GRAPHENE-INCORPORATED METAL ORGANIC FRAMEWORKS AS POTENTIAL ADSORBENTS FOR SOLAR ADSORPTION REFRIGERATION SYSTEMS

BY

Najam ul Qadir

A Dissertation Presented to the

DEANSHIP OF GRADUATE STUDIES

KING FAHD UNIVERSITY OF PETROLEUM & MINERALS

DHAHRAN, SAUDI ARABIA

In Partial Fulfillment of the

Requirements for the Degree of

DOCTOR OF PHILOSOPHY

In

MECHANICAL ENGINEERING

November 2016

KING FAHD UNIVERSITY OF PETROLEUM & MINERALS

DHAHRAN- 31261, SAUDI ARABIA

DEANSHIP OF GRADUATE STUDIES

This dissertation, written by **Najam ul Qadir** under the direction of his dissertation advisor and approved by his dissertation committee, has been presented to and accepted by the Dean of Graduate Studies, in partial fulfillment of the requirements of **DOCTOR OF PHILOSOPHY IN MECHANICAL ENGINEERING.**

Dr. Syed A. M. Said
(Advisor)

Dr. Zuhair M. Gasem
Department Chairman

Dr. Rached B. Mansour
(Co-Advisor)

Dr. Salam A. Zummo
Dean of Graduate Studies

Dr. Habib I. Abualhamayel
(Member)

1/12/16
Date

Dr. Mohamed A. Habib
(Member)

Dr. Khaled Mezghani
(Member)

Dedicated to my beloved Khala

Khala Hameeda

Dedicated to my beloved Rasho Phuppo

Dedicated to my friend Faisal Faraz

ACKNOWLEDGMENTS

I am highly thankful to the continuous support and valuable guidance of my dissertation advisor Prof. S.A.M. Said during the entire course of my PhD study at King Fahd University of Petroleum and Minerals, Dhahran, Saudi Arabia. The constant encouragement and motivation he has been providing for the successful completion of all the research objectives mentioned in my dissertation proposal are highly acknowledged.

I am also thankful to my co-advisor Dr. Rached Ben Mansour for his valuable assistance in almost all the technical problems I have been faced with during my research work. The continuous help and motivation provided by all my committee members namely, Prof. Habib Abulhamayel, Prof. Mohammad Habib, and Dr. Khaled Mezghani are also highly acknowledged.

The laboratory facilities provided by the Center of Research Excellence in Renewable Energy have provided the required platform in the completion of my experimental work in an excellent manner. I am thankful to my Center Director, Dr. Fahd Al-Suleiman, for his continuous support and encouragement during the entire course of my stay in the Fuel Cell Lab for the purpose of completing my experimental research work. I am also grateful to Dr. Amir Al-Ahmed for being a valuable support to the conduction of my experimental work and timely resolution of all the technical problems I have faced in this context.

I am also thankful to Dr. Zain Yamani, Director of the Center of Research Excellence in Nanotechnology, and all the center employees who have provided continuous support for the conduction of Scanning electron microscopy and Powder X-ray diffraction in a timely manner. Similarly, the valuable support provided by Dr. Luai Al-Hadhrami, Director of the Center of Engineering Research, and the respective committee members especially Dr. Anwar-Ul-Hamid, Mr. Hathim Dafalla, and Mr. Abdul Rashid for their ever-lasting technical support in the successful completion of the material characterization as an integral requirement of my dissertation proposal are also highly acknowledged.

TABLE OF CONTENTS

LIST OF TABLES

LIST OF FIGURES

ABSTRACT

Full Name : [NAJAM UL QADIR]

Thesis Title : [GRAPHENE-INCORPORATED METAL ORGANIC FRAMEWORKS AS POTENTIAL ADSORBENTS FOR SOLAR ADSORPTION REFRIGERATION SYSTEMS]

Major Field : [MECHANICAL ENGINEERING]

Date of Degree : November, 2016]

Conventional small-scale adsorption chillers generally employ silica-gel/water or zeolite/water working pairs given the relatively high level of mesoporosity and water affinity in these adsorbent materials. However, the coefficient of performance (*COP*) and specific cooling power (*SCP*) evaluated for these conventional working pairs cannot be still considered practically feasible in the context of a commercial system. Hence, significant improvements concerning the design of the system and/or the choice of the adsorbent/adsorbate pair are required. Metal organic frameworks (MOFs) are one class of micro/nanoporous materials which have been shown to possess water adsorption capacities much higher than those exhibited by their mesoporous counterparts like silica gels and zeolites. However, due to the presence of an organic linker which is present in significantly greater proportion than the metal ion centers, these materials still fail to qualify the heat transfer characteristics required of a commercially feasible adsorbent. This study focuses on the improvement of heat transfer characteristics of two water-stable MOFs, MIL-100(Fe) and MIL-101(Cr), *via* incorporation of either multi-walled carbon nanotubes (MWCNTs) or graphene oxide (GO) using *in-situ* synthesis procedures. The resulting four categories of MOF-based composites with varying weight fractions of MWCNTs or GO have been characterized for microstructure, degree of crystallinity, surface area, thermal stability, water sorption kinetics and hydrothermal cyclic stability. It has been observed that GO/MIL-100(Fe) composite containing 17.75 wt% GO shows the best combination of water vapor uptake, cyclic stability and cost-effectiveness for potential use as adsorbent in commercial-scale adsorption chillers using water as refrigerant.

Keywords: Adsorption refrigeration; metal organic frameworks, specific cooling power

ملخص الرسالة

الاسم الكامل: نجم ال قادر

عنوان الرسالة: الأطر المعدنية العضوية ذات الجرافين المزروع كممتزات ممكنة لأجهزة التبريد الإمتزازي الشمسي

التخصص: هندسة كيميائية

تاريخ الدرجة العلمية: : نوفمبر 2016

تعتمد المبردات التقليدية صغيرة الحجم التي تستخدم تقنية الامتزاز غالبا على الزيولايت او السيليكاجل كزوج تشغيل مع الماء نتيجة لكثرة المسامات متوسطة الحجم الميكروني والإنجذاب العالي لذرات الماء. لكن كفائة الاداء (COP) وقدرة التبريد النوعية (SCP) لهذه المواد صغيرة جدا لدرجة انها لاتصلح للمنافسة التجارية. لهذا السبب يحتاج التبريد بالإبتزاز للكثير من التطوير فيما يتعلق بالتصميم او اختيار زوج ابتزاز مناسب وذلك لإجل إستبدال هذه الانظمة بدلاً عن أنظمة التبريد الكهربائية. في السنين الأخيرة تم تصنيع مواد الأطرالمعدنية العضوية تمسى MOFs ذات مسامات ميكرونية ونانوية وذات إمتصاص عالي للماء تفوق بكثير تلك المتوفرة كالزيولايت و السيليكاجل لكنها بالمقابل ذات خصائص حرارية متواضعة نظرا لتوفر روابط عضوية تربط ذرات المعدن في تركيب MOFs والتي بدورها تجعلها اقل من المطلوب من إجل دخولها في أجهزة التبريد بالامتزاز للغرض التجاري.

هذه الدراسة تركز بشكل كبير على تحسين انتقال الحرارة في مادتين من مواد MOFs وهما MOF-100(Fe) و MOF-101(Cr) عن طريق خلطهما واشراكهما مع الانابيب الكربونية النانوية متعددة الاسطح (MWCNT) او مع اكسيد الجرافين (GO) وذلك خلال مرحلة تصنيع الممتزات. نتيجة لهذا الخلط ينتج عنه اربعة مركبات لممتزات جديدة وكل مركب فيها يختلف باختلاف النسبة الوزنية ل MWCNT او ل GO المضافة الى MOF-100(Fe) و MOF-101(Cr). جميع المركبات الجديدة خضعت لتوصيفات متعددة مثل توصيف البنية التركيبة الميكرونية و التوصيف البلوري وتحديد مساحة المسامات و تحديد الاستقرار الحراي وايضا توصيف حركية الابتزاز والاستقرار الحراري والمائي خلال التدوير. الملفت للنظر من خلال نتائج هذه الدراسة ان المركب GO/MIL-100(Fe) الذي نسبة الجرافين الوزنية فيه 17% هو افضل مازة يمكنه ابتزاز الماء مع تدوير مستقر وسعر مناسب للاستخدام كمزازة في أجهزة التبريد الامتزازية.

كلمات البحث : التبريد بالامتزاز , الأطرالمعدنية العضوية, قدرة التبريد النوعية

CHAPTER 1

INTRODUCTION

1.1. Motivation

The global need for solar-assisted refrigeration and air-conditioning is becoming more pronounced on a daily basis owing to the continuous increases in the unit cost of electricity and the density of population. Solar-assisted cooling effect typically relies on either absorption of a gaseous refrigerant in a liquid absorbent, or adsorption of a vaporized liquid refrigerant in a solid adsorbent; however, solar adsorption refrigeration systems have still not been commercially utilized as much as their absorption counterparts due to the comparatively lower activation energy required for absorption. A great deal of ongoing research is currently underway on exploration of ways to improve the currently observed coefficient of performance (*COP*) of solar adsorption chillers, but a commercially feasible value of *COP* has still not been achieved. Previous studies concerning design and operation of water-based solar adsorption chillers have mostly focused on silica gel, activated carbons and zeolites as adsorbents due to the microporous/mesoporous structure of these materials. However, these adsorbents are still not able to meet the refrigeration demands on a commercial scale due to the limited refrigerant uptake per unit mass of adsorbent. Metal Organic Frameworks (MOFs) are one class of nanoporous materials which are characterized by extremely high specific porosity, and flexibility with which pore geometry can be tailored to desired functionality. Despite significantly higher specific water uptake

compared to traditional adsorbents including silica gel, activated carbons, and zeolites, these materials exhibit relatively lower values of thermal conductivity which limits their widespread use as novel adsorbents for solar adsorption refrigeration systems. However, incorporation of second phase materials like carbon nanotube (CNT), graphene oxide (GO), or activated carbons (ACs) is expected to improve the thermal conductivity of MOFs without interfering with the intrinsic nanoporosity as well as the degree of crystallinity of these materials. This PhD thesis work is based on incorporation of CNTs and GO in two kinds of MOFs, MIL-100(Fe) and MIL-101(Cr) (MIL = Material Institut, Lavoisier), which are already known to retain structural stability on prolonged exposures towards water vapor. The nanocarbon implanted MOFs are characterized for thermal conductivity, crystallinity, and porosity, as well as overall performance as adsorbents in solar adsorption refrigeration systems.

1.2. Research Background

The characteristics of an adsorbent which predominantly influence the working performance of an adsorption refrigeration system include its maximum refrigerant uptake at relatively lower relative pressures, and the kinetics of adsorption/desorption which indirectly depend on the rates of heat and mass transfer. Conventionally used adsorbents like silica gels, zeolites, and activated carbons are stable up to fairly high operating temperatures, but fail to meet the minimum thresholds of refrigerant uptake at lower relative pressures, and adsorption/desorption rates required for a commercially feasible adsorption chiller [1–5]. A recently proposed solution to overcome these challenges is the development of composite adsorbents. Composite adsorbents incorporate second-phase materials which are characterized either by a noticeably higher adsorption capacity than

the base adsorbent, or possess significantly higher thermal conductivity than the matrix material resulting in improved heat transfer and/or mass transfer characteristics of the base adsorbent [6–16].

Metal organic frameworks (MOFs) is a category of organic/inorganic hybrid microporous materials which have been shown to possess water adsorption capacities much higher than those of conventionally used adsorbents mentioned above [33–54]. However, due to the existence of a relatively much greater proportion of organic matter, the resulting lower heat transfer rates in MOF-based adsorbents still do not qualify for the minimum adsorption/desorption rate required for use in a commercial adsorption chiller. The structural details about MOFs can be found later in the text. A number of research groups have recently reported ways to improve the thermal and hydrothermal stability of MOFs *via* addition of carbon materials like GO and CNTs [60–65]. However, only a negligible fraction of these groups have focused on the improvement of thermal conductivity or the heat transfer characteristics of MOFs [65]. Since the emergence of MOF materials as novel adsorbents in commercial adsorption chillers cannot be realized without improving the heat transfer characteristics of these materials, immediate research efforts need to be devoted for these to replace the traditional adsorbents currently being used in low-performance chillers. In the same context, one of the objectives of this PhD dissertation is to improve the thermal conductivity of water-stable MOFs *via* addition of second-phase nanomaterials to an extent that can be considered commercially feasible for a solid adsorbent. However, the volume fraction of the added second phase has to be kept to a limit above which it will start to deteriorate the intrinsic water adsorption capacity, or the adsorption/desorption kinetics of the base MOF adsorbent.

In order to achieve this objective, two best known hydrothermally stable MOFs, MIL-100(Fe) and MIL-101(Cr), have been selected as base adsorbents, whereas the two most thermally conductive as well as commercially cost-effective nanomaterials, multiwalled carbon nanotubes (MWCNTs) and graphene nanoplatelets (GNPs), have been selected as additives to enhance the thermal conductivity of the base adsorbents. The as-synthesized and activated MWCNT or GNP/MOF composites, with varying volume fractions of the added nanomaterials, are then characterized for specific surface area, degree of crystallinity, water adsorption behavior, and hydrothermal cyclic stability, in order to predict the effect of graphene addition on the intrinsic crystal structure, porosity, water adsorption behavior, and adsorption/desorption kinetics of each of the two MOFs selected as the base adsorbents in the study. The type of MWCNT/MOF or GNP/MOF which results in the most optimum theoretically predicted performance of a two-bed solar adsorption chiller, along with the highest hydrothermal cyclic stability of the composite adsorbent, is then proposed as the most appropriate carbon/MOF combination for use as adsorbent in a commercial system. Hence the objective of this dissertation is to propose a water-stable MOF with sufficiently high thermal conductivity which can replace the traditionally used adsorbents for use in a commercial-scale two-bed solar adsorption chiller with an acceptable level of cost-effectiveness as well as cooling efficiency.

1.3. Solar adsorption refrigeration systems

The driving inspiration behind solar-powered cooling technology is the direct correlation between solar irradiation, acting as energy input, and the resultant cooling effect which can be employed for a variety of household and commercial purposes. As already mentioned before, solar-assisted cooling research community is focused to gradually replace the absorption-based systems with adsorption-based ones due to the relatively greater room of engineering available to tailor the properties of a solid adsorbent.

The working principle of a solar adsorption refrigeration system (or solar adsorption chiller) is illustrated in Figure 1.1 [17]. Basically, the adsorption chiller is based upon exchange of refrigerant vapor between the condenser/evaporator and the adsorbent. As the most important property of the refrigerant with regards to adsorption refrigeration is its latent heat of vaporization, water is preferred over other refrigerants like ethanol, methanol, acetone, and chloroform, owing to its highest specific enthalpy of evaporation. There are two basic phases of operation of a solar adsorption chiller – production and regeneration. In the production phase, the refrigerant is evaporated thereby producing the desired cooling effect. The water vapor is then adsorbed by the adsorbent, thereby releasing heat at a medium temperature level. In the regeneration stage, the adsorbent is heated using solar energy thus releasing the adsorbed water in vapor form which is later condensed at a mediocre temperature level. Thermal conductivity of the selected adsorbent, apart from its water adsorption capacity, therefore also plays a significant role in achieving commercially feasible cooling efficiency of the adsorption chiller, as it indirectly affects the number of adsorption-desorption cycles completed per unit operation time.

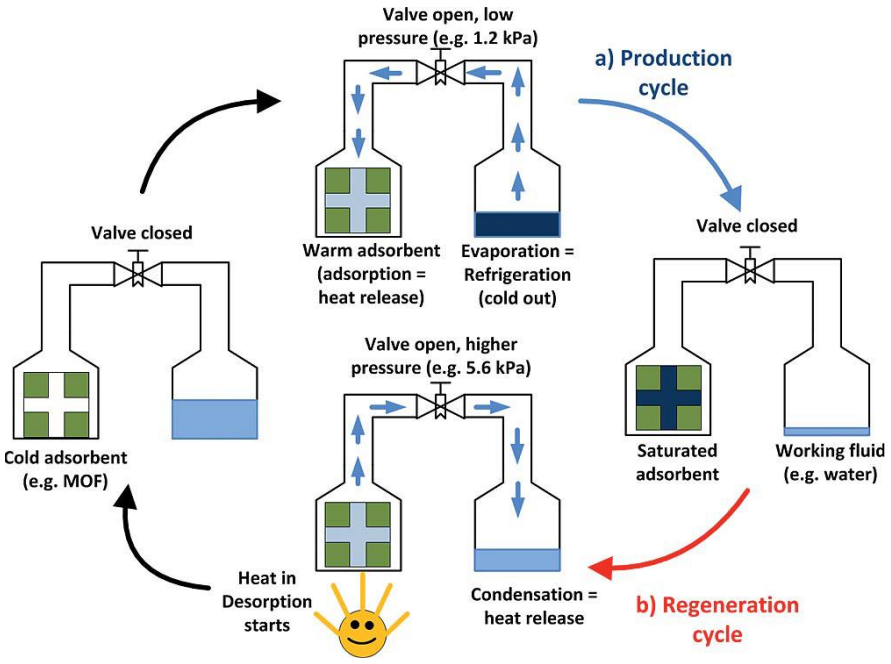

Fig 1.1: Illustration of the basic working principle of a solar adsorption chiller [17].

The foremost requirement of an adsorbent for a chiller application is the maximum achievable exchange of the amount of working fluid within one adsorption–desorption cycle, also known as the "water loading lift". In the van't Hoff diagram illustrated in Figure 1.2, the cycle is defined by the minimum adsorption temperature designated by point B, the highest desorption temperature denoted by point D, and the condenser and the evaporator pressure [17]. The pressure level of approximately 1.2 kPa corresponds to an evaporation temperature of 10°C in the context of operation of a commercial-scale adsorption chiller. The second pressure level of almost 5.6 kPa corresponds to 35°C, which represents the temperature at which heat can be released during a single adsorption/desorption cycle.

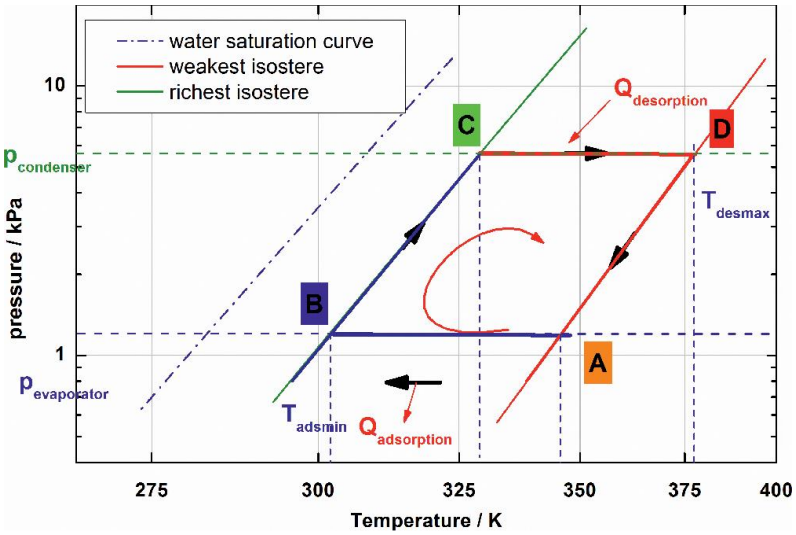

Fig 1.2: Van't Hoff diagram of an ideal adsorption-desorption cycle for a chiller application (the term "isostere" refers to constant water loading lift) [17].

1.4. Selection of adsorbent

Silica gels have been widely studied as potential adsorbents for adsorption chillers using water as refrigerant [21–24], and still represent the most commonly used adsorbent in commercially designed adsorption chillers like the ACS 08 manufactured by Sortech AG [24–25]. However, the main disadvantage of silica gels is low hydrophilicity which ultimately results in a lower water loading lift at lower relative pressures, and consequently a lower value of specific cooling power (*SCP*) for the system. Considering their extremely well-defined porous structure, zeolites have also been extensively evaluated as potential adsorbents for commercial adsorption chillers, faujasites and zeolite A being the most commonly studies classes. However, the relatively greater hydrophilicity of zeolites is the major reason of their restricted use compared to silica gels in commercial adsorption chillers, as temperatures above 200^{o}C are required for achieving a reasonable desorption rate of the refrigerant [27]. Hence, a degree of porosity coupled with structural stability at

operating temperatures, high thermal conductivity to facilitate sufficiently faster adsorption/desorption rate, and retention of pore structure during successive cycles of operation constitute the basic requirements of an adsorbent material for acceptable use in a commercial solar adsorption chiller.

1.5. Metal Organic Frameworks as adsorbents

Conventionally used adsorbent materials like zeolites and silica gels lack the levels of both thermal conductivity as well as adsorption capacities which are required of a commercially viable adsorbent material. Hence, the development of novel microporous materials with high thermal conductivities, water-loading lifts, as well as hydrothermal stabilities, is currently a widely-researched area in the field of solar adsorption refrigeration [26,29]. As a consequence, a newer class of microporous materials referred to as metal organic frameworks (MOFs) also known as porous coordination polymers (PCPs) has emerged [33–54]. MOFs are extended organic-inorganic hybrid networks interwoven *via* complex covalent linkages between metal ion centers or clusters and organic linkers commonly referred to as ligands. A wide variety of strategies meant for synthesizing these versatile frameworks primarily utilize the principles of reticular synthesis [48]. A vast majority of metal cluster geometries in MOFs are, however, based upon transition metals owing to the intrinsic versatility they exhibit in terms of their coordination chemistry. These geometries most commonly include square-planer, tetrahedron, and octahedron among others [49]. The organic ligands, acting as linkers between the organic and the inorganic components, usually consist of cyanides, halides, neutral organic molecules ($4,4' - $bipyradine), and anionic organic molecules (benzene dicarboxylic acid). The organic and inorganic components are known to mutually form *n*-dimensional (*n* = 1,2, and 3) motifs which are

characterized by novel features such as very high specific surface area, large pore volume, and an extreme flexibility of pore geometry in accordance with a large variety of achievable chemical compositions [17,45–50]. As a consequence, not only there exist indefinitely large number of possible network structures, but also an unimaginably large number of possible net topologies as the number of geometrically different vertices and the ways of linkage of these vertices are innumerable. However, it is extremely difficult to deduce synthetic methodologies of MOF structures starting only from simple metal ion centers and organic links, since ions themselves cannot convey sufficient directional information required for this purpose. For example, the underlying structure of carboxylate-based MOFs basically uses the carboxylate functional group to chelate metal (M) ion centers and lock them rigidly into directional M–O–C clusters, where the C atoms in the carboxylate groups act as points of extension constituting well-defined geometrical entities commonly known as secondary building units (SBUs). An innovative design of a rigid framework constructed using such SBUs was presented for the first time in the form of MOF-2 [53] and later in case of MOF-5 [54]. In MOF-5, the $Zn_4O(CO_2)_6$ complexes containing 4 ZnO_4 tetrahedra sharing a common vertex, and 6 carboxylate C atoms that consitute an octahedral SBU, are connected together *via* phenyl linkages. This gives rise to a cubic network where the corner vertices act as the octahedral SBUs, while the edges serve as benzene struts. Since the SBUs and the phenyl linkages are relatively massive and rigid entities, the resultant structure is characterized by an exceptional porosity and extremely high thermal stability. Figure 1.3 shows schematically the crystal structures of MOF-5, zeolite

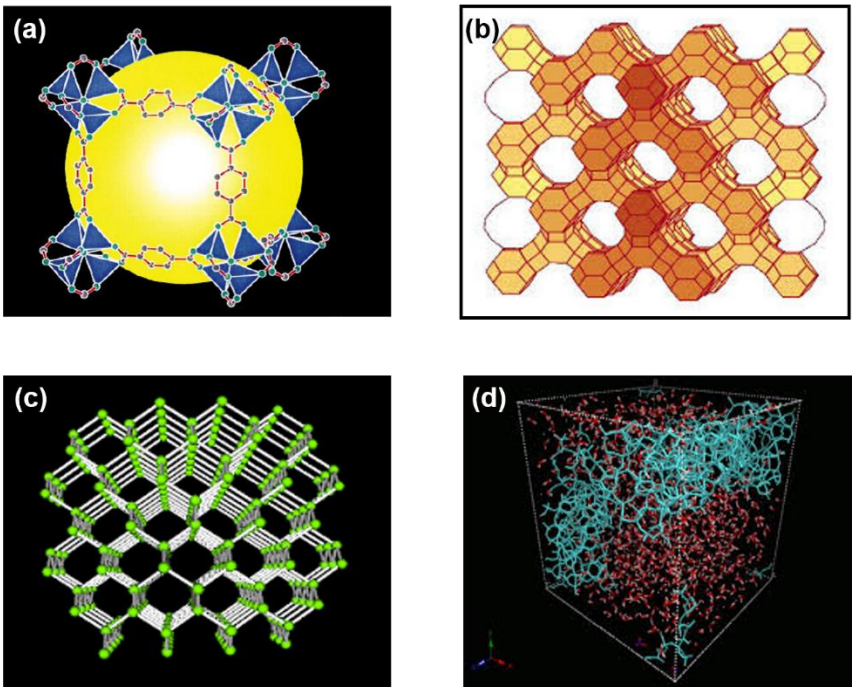

Fig 1.3: Crystal structures of (a) MOF-5 (Eight ZnO_4 tetrahedra, including Zn (blue), O (green), and C (grey) atoms, formulate a unit cell and enclose a yellow spherical pore of diameter 1.85 ^{o}A), (b) faujasite-type zeolite, (c) activated carbon, and (d) silica gel.

(faujasite), silica gel, and activated carbon. It can be easily seen that the MOF-5 unit cell offers a significantly larger pore volume as compared to the other three structures of 1.36 cm^3g^{-1} [55], in contrast to that of activated carbon (0.4–0.6 cm^3g^{-1} [56]), silica gel (0.65 cm^3g^{-1} [57]), and faujasite-type zeolite (0.4 cm^3g^{-1} [58]). Figure 1.4 displays the BET surface areas of some selected MOFs in contrast to those of the conventional porous materials: zeolites, activated carbons and silica gels [59]. As evident, MOFs exhibit significantly higher pore volumes and specific surface areas than the conventional porous materials. As a consequence of the significantly larger pore volume, the water loading lift in a typical adsorption-desorption cycle is observed to be much higher for these materials than traditional adsorbents, as shown in Figure 1.5 [17].

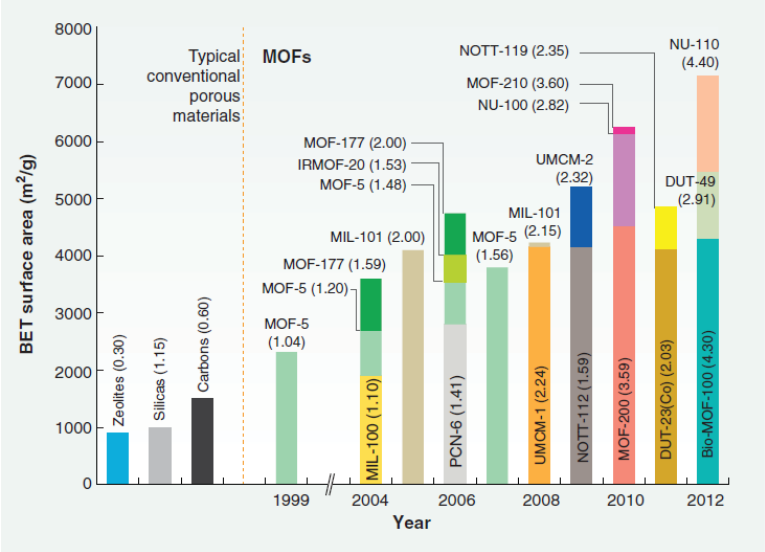

Fig 1.4: BET surface areas of selected MOFs and typical conventional materials estimated from gas adsorption measurements (value in parenthesis is the total pore volume in cm^3g^{-1}) [59].

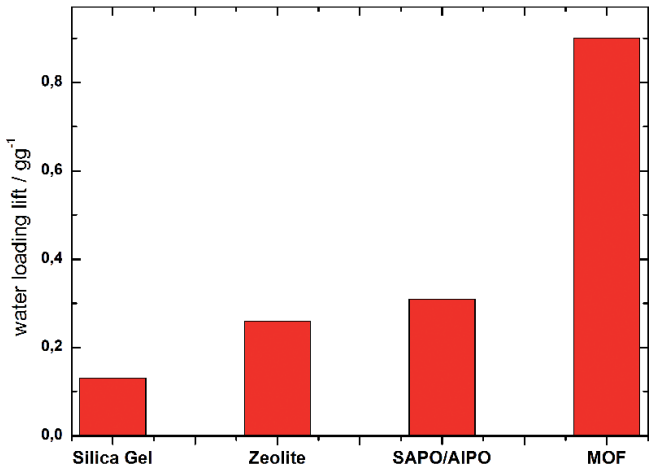

Fig 1.5: Comparison of various adsorbents on the basis of water uptake in a single adsorption/desorption cycle in an adsorption chiller operation [17].

CHAPTER 2

LITERATURE SURVEY

2.1. Basics of adsorption refrigeration

Solar cooling systems incorporate environmentally friendly processes owing to their zero reported rate of ozone-layer depletion, and a negligible effect on global warming compared to conventional technologies including vapor compression [18]. Solar-powered "adsorption" cooling system are reported to be even friendlier to the environment since they are completely independent of any mobile accessories, corrosive media, or noise, and also operate on a low temperature heat source. In such systems, physical or chemical interaction occurs between a pair of substances in order to produce the cooling effect. An adsorption refrigerator (or chiller) is equipped with the unique feature of transforming thermal energy received as input directly into refrigeration effect. In a solar adsorption chiller, the source of this thermal energy is solar radiation. Amongst the pair of substances, the one with the lower boiling point is known as the adsorbate while the other is known as the adsorbent. The adsorbate plays the role of refrigerant during cooling production. Adsorption cooling systems can be distinguished based on the architecture or the number of adsorption/desorption beds, as well as the type of adsorbent/refrigerant working pair used. Silica gel-water, zeolite-water, activated carbon-methanol/ethanol, activated carbon-ammonia, and activated carbon fiber-ammonia have all been used as working pairs in the published literature and a brief summary of the respective research efforts is given in Table 2.1.

Table 2-1: Summary of published literature on adsorption refrigeration systems.

Year	Adsorbent/refrigerant pair	Intended application	Yield	*COP*/*SCP*	Ref.
1982	Zeolite 13X/water	Ice making	7 kg/day	0.04–0.14	[66]
1984	Zeolite 13X/water	Cooling	-	0.086	[67]
1986	Activated carbon/methanol	Ice making	6 kg/day	0.12	[68]
1987	Charcoal/methanol	Ice making	4 kg/day	0.1	[69]
1987	Activated carbon/methanol	Ice making	-	0.1	[70]
1987	Silica gel/water	Cooling	-	0.077	[71]
1993	Activated carbon/ammonia	Ice making	3 kg/day	0.04	[72]
1993	Zeolite 13X/water	Ice making	-	-	[73]
1994	Activated carbon/methanol	Ice making	1 kg/day	0.02	[74]
1996	Activated carbon/ammonia	Ice making	-	0.3	[75]
1998	Silica gel/methanol	Cooling	-	0.3	[76]
1998	Activated carbon/methanol	Ice making	14 kg/day	0.15–0.23	[77]
1999	Activated carbon/methanol	Ice making	4–5 kg/day	0.1–0.12	[78]
2000	Activated carbon/methanol	Ice making	10 kg/day	0.04	[79]
2001	Activated carbon/methanol	Ice making	5–6 kg/day	0.12–0.14	[80]
2001	Activated carbon/methanol	Cooling	-	0.15	[81]
2002	Zeolite 13X/water	Cooling	-	0.4	[82]
2004	Novel silica gel/water	Cooling	-	0.6	[83]
2004	Activated carbon/ammonia	Cooling	-	0.15	[84]
2004	Silica gel/water	Cooling	-	0.16	[85]
2005	Activated carbon/methanol	Cooling	-	0.087	[86]
2005	Silica gel/water	Cooling	-	0.38	[87]
2005	Activated carbon/methanol	Cooling	-	0.055	[88]
2006	Activated carbon/methanol	Grain depot cooling	-	0.105	[89]

Table 2-1 (contd.)

2006	Activated carbon fiber/ethanol	Cooling	-	-	[90]
2006	Silica gel/water	2–stage Cooling	-	1.35	[91]
2006	Charcoal/methanol	Cooling	-	0.15	[92]
2007	Silica gel/water	Cooling	-	0.4–0.6	[93]
2007	Silica gel/water	Low-temperature grain storage	-	0.12	[94]
2007	Activated carbon/methanol	Cooling	-	0.06	[95]
2007	Activated carbon/methanol	Refrigeration	-	0.087	[96]
2007	Silica gel/water	Air-conditioning	-	0.5	[97]
2008	Novel silica gel/water	Cooling	-	0.2	[98]
2008	Silica gel/water	Cooling	-	0.54	[99]
2008	Zeolite/water	Cooling	-	0.14	[100]
2008	Activated carbon/ethanol	Cooling	-	-	[101]
2008	Silica gel/water	Cooling	-	0.3	[102]
2008	Zeolite/water	Cooling	-	0.45	[103]
2008	Activated carbon/methanol	Cooling	-	0.02	[104]
2009	Silica gel/water	Cooling	-	0.3	[105]
2009	Novel silica gel/water	Cooling	-	0.35	[106]
2009	Silica gel/water	Cooling	-	0.47	[107]
2009	Silica gel/water	Cooling	-	0.4	[108]
2010	Silica gel/water	Cooling	-	0.62	[109]
2011	Activated carbon/methanol	Cooling	-	0.211	[110]

For achieving a continuous refrigeration effect, the number of adsorption/desorption beds used in the adsorption chiller must be more than one. A maximum of six beds have been used to date, but two beds have been proven to be sufficient given the performance of the working pair is satisfactory. The schematic layout of a two-bed solar-driven adsorption chiller is shown in Figure 2.1 [19]. It is primarily composed of (*a*) heating water storage tank, (*b*) evacuated tube collectors, (*c*) adsorption/desorption beds, (*d*) cooling towers, (*e*) cooling water storage tank, (*f*) evaporator, (*g*) condenser, (*h*) water pumps, (*i*) valves, (*j*) temperature/pressure sensors, and (*k*) connecting pipes. A real lab-scale setup of a two-bed adsorption chiller based on these components is displayed in Figure 2.2 [19].

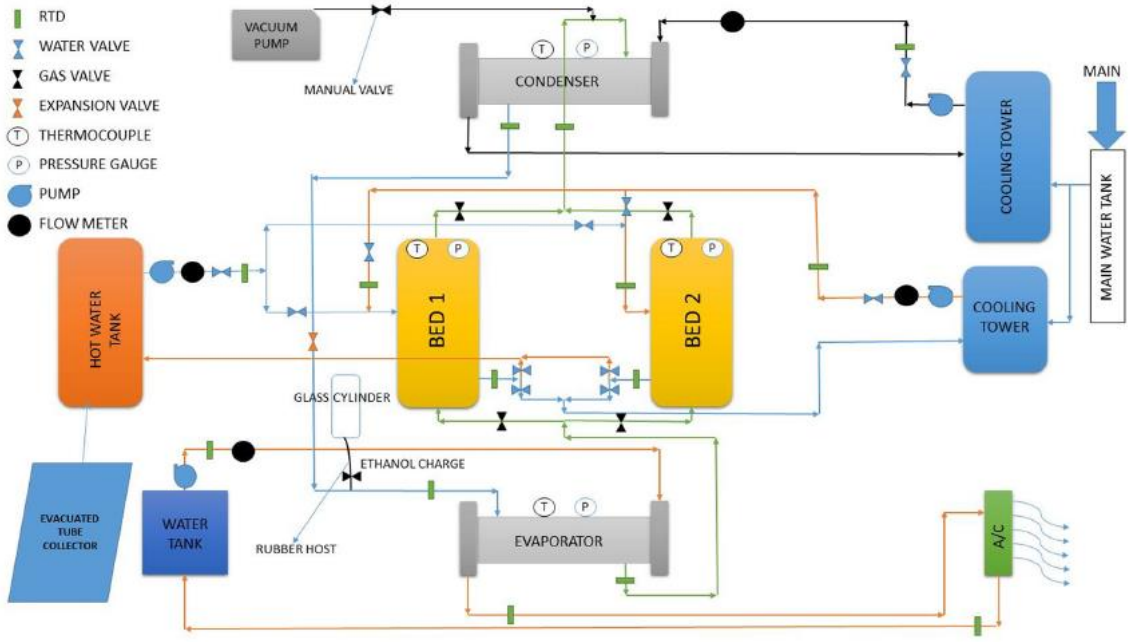

Fig 2.1: Schematic layout of a two-bed solar-driven adsorption chiller [19].

Fig 2.2: A real lab-scale setup of a two-bed solar-driven adsorption chiller [19].

2.2. Conventional adsorbent/refrigerant pairs

The adsorbents used in conventional adsorption chillers can be categorized as physical, chemical, or composite adsorbents in accordance with the adsorption kinetics as well as the nature of guest-host interactions involved during the adsorption process.

2.2.1. Physical adsorbents

The most commonly used physical adsorbents include silica-gels, activated carbons, zeolites, and alumina which are characterized by highly porous structures and specific surface areas of the order of several hundreds. Activated carbon is a form of carbon that has been post-processed for increasing the total pore volume, resulting in a large specific surface area available for vapor adsorption. Methanol and ammonia have been reported as

the most commonly used refrigerants with activated carbon. Activated carbon-methanol has been reported to be one of the most promising working pairs for use in small-scale adsorption chillers owing to its large adsorption capacity coupled with a low heat of adsorption (~1800–2000 $kJkg^{-1}$). Low-temperature heat is a contributing factor to the *COP* of the chiller as the heat of adsorption constitutes the majority of heat consumption during the desorption phase. Another advantage of activated carbon-methanol working pair is the low desorption temperature (~100^{o}C), which is within the appropriate temperature range when solar radiation is used as the heat source. However, activated carbon is known to catalyze methanol into dimethyl ether at working temperatures higher than 120^{o}C.

Activated carbon-ammonia pair is characterized by virtually the same heat of adsorption as the activated carbon-methanol working pair. The main difference lies in the considerably higher working pressure (~1600 kPa at a condensing temperature of 40^{o}C) of the activated carbon-ammonia pair. The high operating pressure demands relatively smaller pipe diameters and hence more compact heat exchangers as compared to those required for the case of activated carbon-methanol pair. However, an added advantage of activated carbon-ammonia pair is the possibility of using heat sources at or above 200^{o}C. The major drawbacks include the inherent toxicity and the pungent ammonia odor.

Silica-gel is a highly porous, granular form of silica which is made synthetically from sodium silicate. For the silica-gel-water working pair, the heat of adsorption is about 2500 $kJkg^{-1}$ while the temperature at which desorption occurs could reach below 50^{o}C. It has been shown that there is approximately 4–6 wt% of water molecules adsorbed in the form of a monolayer on the surface of hydrophilic silica [178]. These water molecules are a compulsory pre-requisite for the adsorption capability of silica-gel, due to which the

temperature at which desorption occurs cannot be raised above 120^{o}C, and is generally lower than 90^{o}C. Such a low desorption temperature renders silica-gel appropriate for use in solar-driven adsorption chillers. The major drawbacks of the silica-gel-water working pair include lower adsorption capacity (~0.2 kgkg^{-1}), lower thermal conductivity of silica-gel (0.2 Wm^{-1}K^{-1}), and its inability to generate evaporating temperatures below absolute zero.

Zeolite is a type of alumina silicate crystal which is composed of either alkali or alkali soil. The heat of adsorption of zeolite-water working pair is relatively higher than that of silica-gel-water (3300–4200 kJkg^{-1}). The desorption temperature of zeolite-water is higher than 200^{o}C due to its more or less stable reported performance at higher temperatures. The drawbacks of zeolite-water working pair are the same as mentioned above for silica-gel-water: low adsorption capacity, lower thermal conductivity, and the inability to produce subzero evaporating temperatures.

2.2.2. Chemical adsorbents

Chemical adsorption is characterized by the presence of a strong chemical bond between the functional groups in the chemical structure of the adsorbent and the refrigerant molecules. The chemical bond mainly performs the functions of coordination, complexation, oxidization, and hydrogenation. The most commonly reported chemical adsorbent for use in solar adsorption chillers is calcium chloride. Calcium chloride has been shown to adsorb ammonia producing $CaCl_2.8NH_3$ and water, which further combine to form $CaCl_2.6H_2O$ as a by-product. Other metal chlorides used as chemical adsorbents include magnesium chloride, strontium chloride, barium chloride, cobalt chloride, and manganese chloride. The main advantage observed for metal chloride-ammonia working

pairs is the higher adsorption capacity compared to that measured for the physical adsorbent-refrigerant pairs. The major drawbacks, however, include: (*a*) relatively higher desorption temperatures, and (*b*) swelling and agglomeration of adsorbent particles during continuous operation which eventually degrades the performance of adsorption chiller.

2.2.3. Composite adsorbents

Composite adsorbents either incorporate a homogeneous combination of two or more adsorbents, or an adsorbent with a filler material like expanded natural graphite (ENG), activated carbon fiber, functionalized carbon nanotubes (CNTs), or exfoliated graphene nanoplatelets (GNPs). The main objectives of synthesizing composite adsorbents include: (*a*) improve heat and mass transfer rate of the base adsorbent, (*b*) enhance the refrigerant adsorption capacity of the base adsorbent, and (*c*) increase the thermal stability of the base adsorbent for it to withstand relatively higher working temperatures.

Composite adsorbents have been fabricated for use in an adsorption heat pump via impregnation of hydrophilic silica into the mesopores and micropores of activated carbons [8]. The water adsorption isotherms of the composite adsorbents were observed to shift to lower relative pressures, and water adsorption capacity was found to be higher than those of raw activated carbons. In a similar fashion, composite adsorbents involving varying volume fractions of ENG in activated carbon have also been developed for use in an adsorption refrigeration system [9]. The thermal conductivity of the composite adsorbent was observed to increase to almost ten times that of activated carbon, while ammonia adsorption was found to increase by 29% at an evaporating temperature of 8^{o}C. Composite adsorbents comprising activated carbon, silica gel and calcium chloride have also been synthesized for use in a solar adsorption cooling system [10]. Water adsorption

measurements on the composite adsorbent resulted in almost 933% higher uptake than raw activated carbon, while the *SCP* and *COP* of the system were measured to be 378 Wkg^{-1} and 0.7 respectively. Composite adsorbents of $CaCl_2$ and sawdust were also fabricated with maximum adsorption capacity of 0.774 gg^{-1}, which resulted in a *SCP* of 869 Wkg^{-1} at a cycle time of 5 min [11]. Similarly, a $Ca(NO_3)_2$ modified silica composite adsorbent was developed for use in a laboratory-scale adsorption chiller using water as refrigerant [12]. An experimentally measured *SCP* of 389 Wkg^{-1} at a cycle time of 10 min was achieved, corresponding to a *COP* of 0.31. A $CaCl_2$ incorporated zeolite 13X composite adsorbent showed a difference in equilibrium water uptake almost 420% higher than that measured for pure zeolite 13X between 25°C and 75°C [13]. This led to an increase in *SCP* of the cooling system by 35% and *COP* by almost 81%. More recently, a novel composite adsorbent comprising a hybrid sawdust/$CaCl_2$ matrix and ENG as the filler material was fabricated for use in an adsorption chiller using ammonia as refrigerant [14]. The sawdust was carbonized and activated prior to composite fabrication in order to enhance the mass transfer characteristics of the adsorbent, while the heat transfer characteristics were improved by the addition of ENG. The composite adsorbent comprising 30wt% ENG was evaluated to show the best performance for potential use in an adsorption chiller, resulting in an *SCP* of 801.7 Wkg^{-1} for an adsorption time of 10 min. Similarly, a $CaCl_2$-filled silica gel composite adsorbent showed an equilibrium water uptake almost 685% that of raw silica gel at a relative humidity of 20% and adsorption time of 2 hours [15]. In comparison, a $CaCl_2$-filled activated carbon fiber cloth (ACFC) composite adsorbent showed a maximum equilibrium water uptake almost 200% higher than that of raw ACFC at a

relative pressure of 0.39, and a predicted *COP* of 0.7 for the adsorption cooling system [16].

2.3. Drawbacks of conventional adsorbent/refrigerant pairs

The major drawbacks of conventionally used adsorbent/refrigerant pairs can be listed as: (*a*) lower thermal conductivity resulting in larger required adsorbent mass, larger required surface area of solar collector, and higher required desorption temperature, (*b*) lower surface area resulting in lesser adsorbed quantity of refrigerant per unit mass, (*c*) non-uniformity of pore-size and shape, (*d*) inability to produce evaporating temperatures below absolute zero, (*e*) necessity of very high vacuum to accelerate rate of refrigerant desorption, and (*f*) lower hydrothermal cyclic stability in case of water as refrigerant. The aforementioned problems associated with conventional adsorbent/refrigerant pairs eventually result in lower measured *COP* and *SCP* values for the adsorption chiller which fail to meet the minimum thresholds required in the context of a commercial adsorption refrigeration system. In other words, the currently available adsorption chillers in the market are only able to meet small-scale refrigeration needs, and thus cannot be considered feasible for use in commerce and industry. Hence, for adsorption cooling technology to successfully replace the electrical cooling technology in the coming decade, significant improvements concerning the design of the system and/or the choice of the adsorbent/adsorbate pair are required. As the most important property of the refrigerant with regards to adsorption refrigeration is its specific evaporation enthalpy, water is preferred over other refrigerants like ethanol, methanol, acetone, and chloroform, owing to its highest specific evaporation enthalpy. In this context, numerous research attempts have been conducted in order to synthesize the most appropriate adsorbent for achieving a

practically feasible performance of a commercial adsorption chiller using water as refrigerant. Although a vast majority of these potential adsorbents are either silica-gel- or zeolite-based, yet none can be considered practically viable for use in a commercial-scale adsorption chiller owing to the lower *COP* as well as *SCP* achievable using these traditional adsorbents.

2.4. Metal Organic Frameworks

Despite the remarkable progress that has been accomplished in development of novel materials for use in adsorption refrigeration, a significant amount of research effort is still required to modify the currently developed micro- and mesoporous materials in order to qualify them for use as adsorbents in commercial-scale adsorption chillers [26,111–112]. Metal organic frameworks (MOFs) constitute one such class of newly-researched materials which possess certain unique features such as extraordinary high specific surface area, extremely large pore volume, and a virtually unlimited degree of chemical, morphological, and physiochemical variability by virtue of their tunable composition. With regards to usage in adsorption chillers using water as refrigerant, the key attributes include the water adsorption behavior and storage capacity, which are strongly dependent on the specific pore volume achievable in the materials. With ongoing research, the specific volume has increased from 1 cm^3g^{-1} reported for MOF-5 up to more than 2 cm^3g^{-1} reported for MIL-101(Cr) [45,121]. In addition to increasingly high pore volumes, extremely high specific surface areas up to more than 6000 m^2g^{-1} have been reported for several MOFs [176]. In addition, a particular category of these materials is capable of exhibiting a reversible transformation in intrinsic pore morphology following adsorption of water molecules, which occasionally may also be accompanied by a reversible shift in the physical

properties. This phenomenon which is referred to as the "breathing effect" has been observed for several MOF structures with distinctive dimensionalities, and practically evidenced to lead to a gradual step-wise adsorption of water molecules [17]. It has been observed to occur at a specific gate pressure during the adsorption phase when the framework gradually transforms from a closed structure to an open one.

Compared to conventional adsorbents like silica gels, activated carbons, and zeolites, MOFs have been practically experienced to exhibit a much higher degree of versatility in terms of composition, topology, as well as pore structure. The inherent flexibility allowable in selecting the metal-cluster/linker combination facilitates construction of frameworks with user-defined pore morphologies and linker functionalities over a wide range. An additional advantage pertains to the mechanism used for synthesis in which the solvent used in the reaction mixture itself acts as the main template for synthesis in contrast to the template-assisted synthesis of most zeolites, which requires an additional high-temperature calcination procedure to remove the guest molecules needed for achieving the desired level of microporosity.

2.4.1. Water adsorption mechanisms in MOFs

According to Cavinet et al. [113], three different mechanisms for adsorption in MOFs can be identified – (*a*) adsorption in the metallic cluster which chemically modifies the first coordination sphere of the metal ion (irreversible), (*b*) layer or cluster adsorption in pores (reversible), and (*c*) capillary condensation in pores (irreversible). Since the majority of MOFs consist of aromatic ligands which are hydrophobic in nature, cluster adsorption is prevalent over layer formation when water is being used as the adsorbate. In MOFs, clusters of water can be formed around three different sites. For MOFs that have

coordinatively unsaturated sites on the metal ions after solvent removal, water molecules can be clustered around those sites. The first water molecule will then be irreversibly adsorbed, modifying the coordination sphere of the concerned ion. Terminal groups on the metal ions of the cluster, when present, are predominantly hydroxide-based species which can also act as nucleation sites for the clustering of water molecules. Finally, hydrophilic functional groups can be attached to the organic ligand, resulting in additional nucleation sites.

2.4.2. Stability of MOFs in aqueous media

One of the key pre-requisites needed for the successful applicability of a given adsorbent material in a chiller or heat pump application is to maximize its structural stability towards repeated exposure to adsorption-desorption of the working fluid with increasing number of cycles. The water sensitivity of MOFs has been a subject of increasing attention amongst the MOF research community dedicated to the development of water-stable frameworks, both at ambient and elevated temperatures [45,114–122]. The main reason suggested for structural degradation in an aqueous medium, is the binding of water molecules to unsaturated metal sites [123], with the exception of MOF-5 which has no coordinatively unsaturated sites but still undergoes structural disintegration on exposure to water vapor [116]. Consequently, many research attempts have successfully resulted in finding ways to develop water stable MOFs using functionalization with hydrophobic functional groups, either by direct synthesis using functionalized linkers [115,124], or by post-synthetic modification of the framework [125]. It has been generally observed that MOFs which are hydrothermally synthesized show higher water stability than those which are synthesized in the absence of an aqueous medium.

Recent studies concerning the development of water-stable MOFs have concluded that MOFs based on Al-carboxylate coordination chemistry are amongst the most hydrothermally stable of these materials reported to date [126–127]. Among the carboxylate-based MOFs, hydrophilic MIL-101 and MIL-100, 8-coordinated Zr-MOF UiO-66, and MOF-74/CPO-27 have all been observed as water-stable, but for certain prescribed levels of environmental humidity [48,128–129]. Similarly, nitrogen-coordinated MOFs have been experienced to more water-stable than carboxylate-based MOFs due to the comparatively higher basicity of nitrogen-based ligands than carboxylic acid [126,130]. For example imidazolate-based ZIF-8 (ZIF = zeolitic imidazolate framework) has been investigated to retain structural stability upon exposure to high levels of humidity [48]; however, loss of framework integrity has been observed upon dispersion in water for 3 months [131]. Moreover, this compound does not adsorb water even to high relative pressures [48]. The water adsorption isotherm of ZIF-8 has also been observed to indicate its strong hydrophobic character, showing only insignificant water adsorption up to p/p_0 = 0.6 (sample pressure/saturation vapor pressure) followed by a marginal increase of approximately 10 cm^3g^{-1} up to p/p_0 = 0.8, and a final abrupt increase to about 150 cm^3g^{-1} attributable to water condensation in the higher pressure region [48]. In general, the hydrothermal stability of MOFs containing imidazolates and other nitrogen-containing ligands has been observed to be higher than that of carboxylate-based MOF materials [126]. It has also been proposed that structural stability of MOFs in aqueous media can be improved *via* chemical attachment of functional moieties, *e.g.* alkyl or fluorinated groups, resulting in increased hydrophobicity of the framework [124–125,132].

2.4.3. Hydrothermal cyclic stability

In certain applications where MOF-based adsorbents are subjected to continuous alternating phases of adsorption and desorption, like adsorption chillers or heat pumps, the selected framework is not only required to be hydrostable, but also capable of retaining its structural integrity on repeated exposure to subsequent adsorption/desorption cycles [45,47,117–119]. Hydrothermal cyclic stability of a MOF-based adsorbent ensures that it not only retains its structural stability during the hydrothermal cycling process, but also maintains the adsorption capacity of the refrigerant for a reasonably large number of adsorption cycles. Hence, the requirement of hydrothermal cyclic stability poses additional constraints on the method being adopted to enhance the hydrostability of the framework, so as to ensure sufficient level of metal-ligand bond strength for achieving satisfactory performance in such applications.

MIL-101(Cr) has been evaluated to adsorb the highest proportion of water molecules in the relative pressure range of $0.4 < p/p_0 < 0.54$ [45], while a porous material is expected to perform in the $0.05 < p/p_0 < 0.4$ range for satisfactory performance in a thermally-controlled adsorption heat pump application. In order to modify the adsorption characteristics of MIL-101(Cr), so as to achieve maximum adsorption capacity in the recommended relative pressure range, Anupam et al. [121] introduced hydrophilic amino- or nitro- functionalities into the framework using time-controlled post-synthetic modification of the parent MOF, for intended use in thermally driven commercial adsorption chillers or heat pumps. Hydrothermal cycle stabilities over 40 ad-/desorption cycles were investigated for four types of samples – MIL-101(Cr)-NH_2, MIL-101(Cr)-*p*NH_2, MIL-101(Cr)-NO_2, and MIL-101(Cr)-*p*NO_2, where *p* denotes partial amination of the respective ligand. In order to

evaluate the hydrothermal cyclic stability, the activated MOF samples were subjected to a repetitive water adsorption-desorption cyclic test between 40 and 140 ^{o}C, under a constant water vapor pressure of 5.2 kPa. The variation in uptake for 40 consecutive cycles for each of the four samples is shown in Figure 2.3 [121]. MIL-101(Cr)-NH_2, MIL-101(Cr)-NO_2, and MIL-101(Cr)-*p*NO_2 were observed to exhibit a drop in the uptake at the beginning of the cyclic test which, however, became more or less constant for MIL-101(Cr)-NH_2 and MIL-101(Cr)-NO_2 starting from the 4th and the 15th cycle, respectively. For MIL-101(Cr)-*p*NO_2, the mass of water was observed to decrease continuously over the designated period of 40 cycles. However, the partially aminated MIL-101(Cr)-*p*NH_2 has been observed to show the highest water loading for 40 consecutive water adsorption-desorption cycles [121]. From the N_2 adsorption isotherms obtained at 77 K, the amino-functionalized samples (MIL-101(Cr)-NH_2 and MIL-101(Cr)-*p*NH_2) were observed to retain their respective BET surface areas, and pore volumes at the end of the cycling experiment [121]. The difference between hydrothermal cyclic stabilities of different MOFs may be explained by the net enthalpy released at the adsorption sites accompanying any phase changes, which has been found to be of the same order of magnitude as the average ligand displacement energy. Since water molecules are continuously engaged in adsorption and desorption to and from the adsorbent during chiller operation, the pores become continually stressed by the alternating pressures generated through cavitation as well as capillary forces, and the probability of the metal-ligand bond to undergo hydrolysis eventually increases with increasing number of cycles. Figure 2.4 shows a comparison of the hydrothermal cyclic stabilities of selected MOFs after 20 and 40 consecutive adsorption-

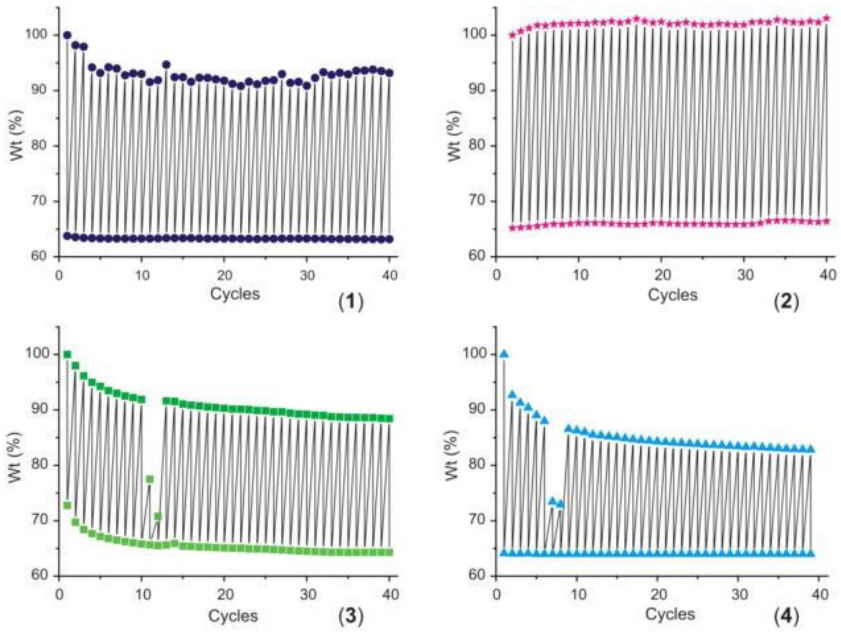

Fig 2.3: Variation of adsorbed amount with number of cycles during cyclic water adsorption/desorption in functionalized MIL-101(Cr) samples for 40 cycles: (1) = MIL-101(Cr)-NH_2, (2) = MIL-101(Cr)-*p*NH_2, (3) = MIL-101(Cr)-NO_2, (4) = MIL-101(Cr)-*p*NO_2 [121].

desorption cycles. It can be observed that MIL-101(Cr) clearly outperforms the other MOFs, followed by MIL-100(Fe). From the published research literature reported to date, the following conclusions can be drawn concerning the structural stability of MOFs in aqueous media:

1. Among the MOFs reported to date, Zn-based MOFs, particularly IRMOF-1, have been observed to be most moisture-sensitive owing to their relatively weak metal-oxygen coordination bonds, which are vulnerable to hydrolysis and lead to the disruption of the open framework structure.

2. Chemical stability of carboxylate-based MOFs in aqueous media improves with increasing inertness of the central metal ion included in the framework.
3. Basicity of Ligand is the most important parameter which affects the structural stability of MOFs in aqueous media, since higher ligand basicity results in greater metal-ligand bond strength.
4. In general, MOF structures based on pyrazole and imidazole linkers exhibit higher water-stability than carboxylate-based MOFs owing to the relatively higher basicity of the former class of ligands.
5. Metal centers with lower coordination numbers are expected to result in shorter bond lengths, and have been suggested to result in relatively greater metal-ligand bond strengths.
6. MOFs containing 6-coordinate (usually octahedral) metal centers are observed be more stable than those containing 4-coordinate (usually tetrahedral) metal centers.
7. Metal centers or clusters with higher oxidation states result in relative higher stability towards reaction with water molecules.
8. Metal-ligand bond strength is a more contributing factor than coordination geometry, or valence, for M^{3+}-containing MOFs than for M^{2+}-containing ones (M = metal center).
9. The Zr_6 cluster has been observed to be one of the most stable secondary building unit for MOF construction, and is largely responsible for exceptional hydrothermal stability of MOFs like PCN-222.
10. *In-situ* functionalization of the organic linker is the most cost-effective and time-efficient strategy for improving the hydrostability and hydrothermal cyclic stability

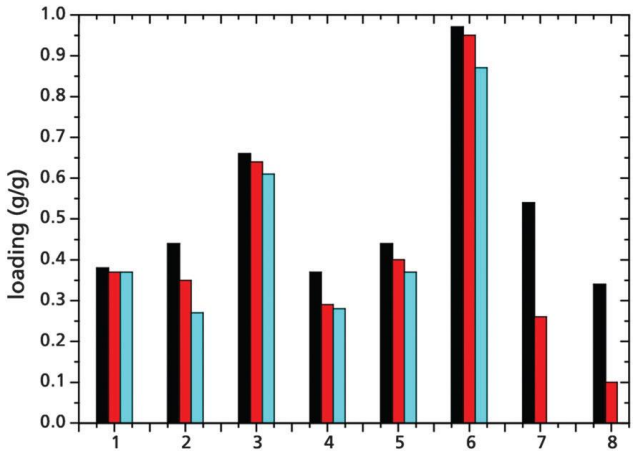

Fig 2.4: Water uptake measurements on (1) Al-fumarate [139], (2) UiO-66 [120], (3) MIL-100(Fe) [47], (4) MIL-100(Al) [47], (5) H_2N-MIL-125 [120], (6) MIL-101(Cr) [45], (7) HKUST-1 [17], (8) Basolite® F300 [17] (black: after activation, red: after 20 adsorption-desorption cycles, blue: after 40 adsorption-desorption cycles).

of MOFs for use in commercial applications like adsorption chillers and heat pumps.

11. Using catenation in conjunction with a pillaring strategy, it is possible to improve the water-stability of MOFs despite the relatively lower basicity of the pillar ligand.

Figure 2.5 summarizes the various factors which control the structural stability of MOFs as well as the different methods which can be adopted to improve the hydrothermal stability of the framework.

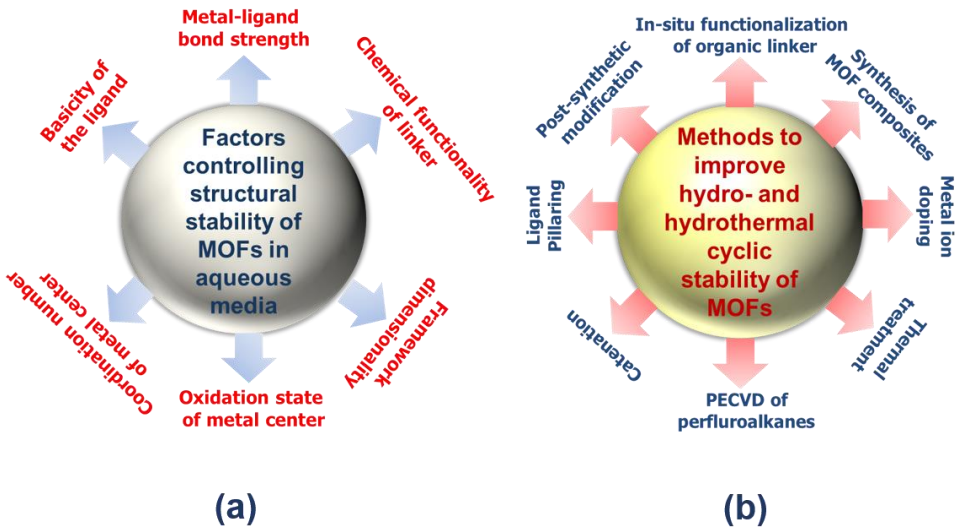

Fig 2.5: (a) Factors controlling the structural stability of MOFs in aqueous media, and **(b)** methods used to improve the hydro- and hydrothermal cyclic stability of MOFs (PECVD = plasma enhanced chemical vapor deposition).

2.4.4. Selection of MOFs as adsorbents

As mentioned above, the three foremost requirements of an adsorbent for use in an adsorption chiller include its maximum water loading lift in a single adsorption-desorption cycle, its hydrothermal cyclic stability, and its thermal conductivity. Amongst the MOFs developed so far, MIL-100(Fe) and MIL-101(Cr) best qualify as potential adsorbents for use in adsorption chillers since they exhibit the best combination of high water adsorption capacities and hydrothermal cyclic stabilities [17,28,45,47–48,133]. More specifically, MIL-101(Cr) has been found to exhibit water adsorption capacity in the range of 1–1.5 gg^{-1}, followed by MIL-100(Fe) of 0.65–0.75 gg^{-1}, and MIL-100(Cr) of 0.6–0.7 gg^{-1} [134]. The highest hydrothermal cyclic stability of all MOFs has been attributed roughly equally to both MIL-100(Fe) and MIL-101(Cr) [47], although MIL-101(Cr) has recently been shown to be marginally better in this context [134]. MIL-100(Fe) is a iron(III) trimesate with the

formula unit C-O-$Fe_3O(H_2O)_2(OH)_{0.19}[C_6H_3(CO_2)_3]_2.mH_2O$ where m~14.5, whereas MIL-101(Cr) is a chromium(III) terephthalate with the formula unit C-O-$Cr_3O(H_2O)_2O[(O_2C)$-C_6H_4-$(CO_2)]_3.mH_2O$ where m~25. The preliminary experiments on hydrothermal stability of MIL-101(Cr) reveal a negligible framework degradation of approximately 3.1% after 40 consecutive adsorption-desorption cycles [17]. However, since Fe is more environmentally benign as compared to Cr, prolonged performance of MIL-100(Fe) as adsorbent in a chiller application might be better suited than MIL-101(Cr), despite being expected of resulting in a slightly lower cooling efficiency. Figure 2.6 shows the framework topologies revealing the pore structures of each of these MOFs. The BET surface areas have been measured to be 3314 m^2g^{-1} for MIL-101(Cr) [135] and 2050 m^2g^{-1} for MIL-100(Fe) [136], with total pore volumes of 1.68 cm^3g^{-1} and 0.9 cm^3g^{-1} respectively. The diameters of the inner cages as well as the openings of the pore windows of MIL-100(Fe) are relatively smaller than those of MIL-101(Cr). Unlike MIL-101(Cr), both MIL-100(Fe) and MIL-100(Cr) exhibit a relatively smaller hysteresis between the desorption and the adsorption phases, which is attributable to the comparatively smaller pores as well as the higher degree of polarity of linker molecules. Furthermore, Akiyama et al. have performed a water-stability test on MIL-100(Fe), experiencing no significant decline in its adsorption capacity even after two thousand cycles [50].

The water adsorption capacity of MOFs is not only assessed by the total pore volume, but also by the hydro-phobicity/philicity of the linker, including the hydrogen bonding affinities of the functional groups, and the degree of susceptibility of the framework to undergo structural transition upon exposure to water molecules [137–139]. Figure 2.7 shows the water adsorption isotherms of a few selected MOFs at 25^oC [134]. As clearly

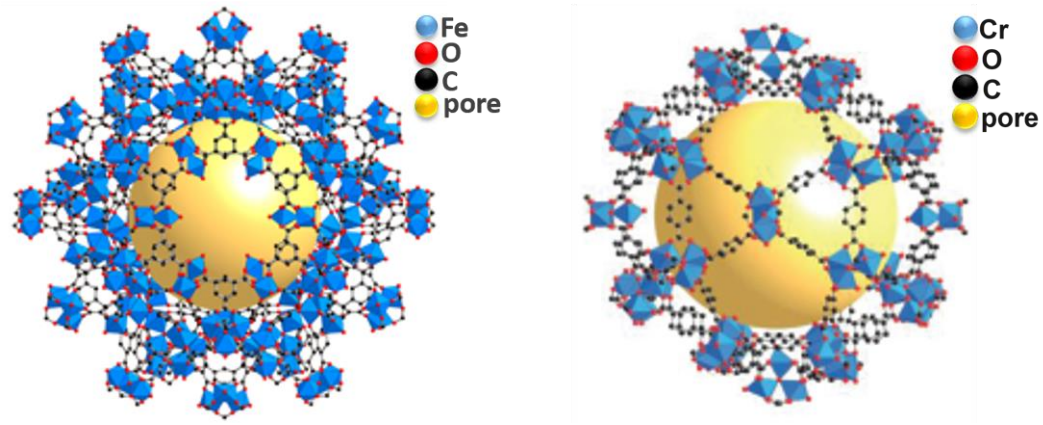

Fig 2.6: Framework topologies revealing the pore structures of **(a)** MIL-100(Fe), and **(b)** MIL-101(Cr) [177].

seen, for $0.1 \leq p/p_0 \leq 0.41$, MIL-100(Fe) shows a higher water uptake than MIL-101(Cr) which exhibits a steep isotherm increase only for $p/p_0 > 0.41$. Keeping this in view, and the fact that Cr is an environmentally toxic heavy metal, the selection of MIL-100(Fe) as adsorbent for a continuous, long- term performance of a solar adsorption chiller might be more suited than MIL-101(Cr) for this application which, however, needs further evaluation.

2.4.5. Deficiencies of MOFs as adsorbents

For applications in periodically working adsorption chillers, the relatively lower hydrothermal stability of MOFs than conventionally used adsorbents is a disadvantage, and is the most critical issue [139]. The decisive factor in the context of hydrothermal stability is the strength of the metal-ligand coordinative bond, which controls the rate of framework decomposition due to the gradual substitution of ligand with water molecules. A vast majority of metal-linker combinations have generally been proven unstable towards

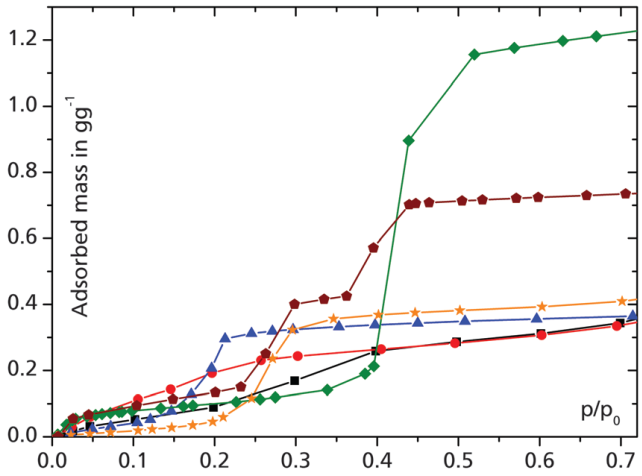

Fig 2.7: Water adsorption isotherms for some selected MOFs at 25°C (squares: UiO-66 [120], circles: H_2N-UiO-66 [120], triangles: H_2N-MIL-125 [120], diamonds: MIL-101(Cr) [45], stars: Al-fumarate [134], pentagons: MIL-100(Fe) [47]).

reaction with water [140]. A much higher proportion of organic matter relative to the inorganic portion is the main reason behind the limited hydrothermal stability of the framework, which typically lies between 150–250°C and seldom surpasses 300°C. This value is considerably lesser than the known value for zeolites. As already mentioned above, a sufficiently high value of thermal conductivity of the adsorbent is crucial in achieving a commercially feasible value of *SCP* for a commercial adsorption chiller. This requirement becomes even more significant in case of a solar adsorption chiller, since solar energy cannot be considered as efficient as direct thermal energy in raising the adsorbent temperature during the desorption phase. Since the thermal conductivity of heat exchanger tubes used in adsorption chillers typically lies between 200 and 400 $Wm^{-1}K^{-1}$ compared to 0.3 $Wm^{-1}K^{-1}$ of a water stable MOF, MIL-100(Fe), the phonons face a tremendous barrier

when heat transfer takes place between the heat transfer fluid flowing inside the tubes and the adsorbent. This will indirectly prolong the water vapor desorption phase, thus increasing the cycle time and hence lowering the value of *SCP*. Hence there exists a need to improve the currently observed values of thermal conductivity of MOF materials before they can be considered as feasible adsorbents for commercial adsorption chillers. This leads to the concept of incorporation of thermally conductive second-phase particles in the MOF structure to an extent that the intrinsic water adsorption capacity, crystal structure, and hydrothermal cyclic stability are not adversely affected.

2.4.6. Improvement of thermal conductivity of MOFs

It is clear from the foregoing discussion that improvement of thermal conductivity of MOF adsorbents is the foremost requirement in achieving an affordable cycle time (or *SCP*) in the context of long-term performance of a commercial adsorption chiller. A number of factors need to be considered while incorporating second-phase materials (fillers) inside MOFs in order to enhance the currently observed thermal conductivity of the framework. These mainly include the axial thermal conductivity of the filler, its aspect ratio (length-to-diameter ratio), interfacial bonding with the surrounding matrix, and the homogeneity of dispersion. Fillers with higher aspect ratios are preferred since thermal percolation threshold can be reached at a relatively lower volume fraction, thus better preserving the intrinsic properties of the MOF matrix. A stronger interfacial bonding facilitates an easier phonon transfer between the filler and the surrounding matrix, leading to lesser interfacial heat dissipation, while a homogeneous dispersion ensures uniformity of thermal conductivity enhancement throughout the MOF structure. Along with these considerations,

the cost of the filler itself also holds significant importance in the context of economic feasibility for a commercial adsorption chiller.

Table 2.2 presents five candidate materials which can be considered as potential fillers for improving thermal conductivity of MOF adsorbents for commercial adsorption chillers. The axial thermal conductivity of each filler, and the associated unit cost are also highlighted in the table. It can be concluded from the data presented in Table 2.2 that graphene GNPs offer the best trade-off between axial thermal conductivity and unit cost, followed by copper nanoparticles (CuNPs), with regards to the long-term performance of a commercial solar adsorption chiller. However, since GNPs are sheet-like nanoparticles, stacking of adjacent nanoparticles in the matrix is expected to take place rather than end-to-end contact, which is a necessary condition for formation of a percolation network at affordable volume fractions. A similar argument holds for CuNPs which are either spherical or ellipsoidal in shape, and also necessitate relatively higher volume fractions to form a percolation network. Since MWCNTs are tubular nanoparticles, end-to-end contact is highly expected to predominate particle stacking, thus facilitating network formation at relatively lower volume fractions. The primary drawback of using CuNPs as fillers is the particle functionalization which is necessary to achieve strong interfacial bonding between the particles and the surrounding MOF matrix, and requires sophisticated chemical procedures in the case of metal nanoparticles [141]. In contrast, graphene can be easily functionalized using simple acid-treatment methods [142], and hence appears more economically feasible than metal nanoparticles in the context of a commercial-scale functionalization setup. In other words, both GNPs and MWCNTs appear as potentially feasible candidate fillers for thermal conductivity enhancement of MOF adsorbents, but

Table 2-2: Candidate second-phase materials as thermally conductive fillers for use in MOF adsorbents with respective values of thermal conductivity and unit cost (MWCNTs: multi-walled carbon nanotubes, SWCNTs: single-walled carbon nanotubes, GNPs: graphene nanoplatelets, CNFs: carbon nanofibers, CuNPs: copper nanoparticles).

Filler	MWCNTs	SWCNTs	GNPs	CNFs	CuNPs
Axial thermal conductivity ($Wm^{-1}K^{-1}$)	2600	1750–5800	3000	1900	370 (400nm)
Cost ($\$Kg^{-1}$)	400–450	35000	200–300	6000	658 (580 nm)

further evaluation is required to conclude which one is more appropriate in the context of use in a commercial solar adsorption chiller.

2.5. Research objective and methodology

The objective of this research is to propose a water-stable MOF with sufficiently high thermal conductivity for use as adsorbent in a two-bed solar adsorption chiller which can be synthesized reproducibly with an industrially scalable as well as cost-effective procedure, and outperforms the traditionally used adsorbents with respect to chiller performance in the context of a commercial system. In order to achieve this objective, the following stepwise methodology has been designed:

1. Select two of the most water-resistant and hydrothermally stable MOFs from recently published literature which can also be synthesized with the highest level

of compatibility on a commercial scale. These have been observed to be MIL-100(Fe) and MIL-101(Cr).

2. In order to improve the thermal conductivity of each of these two MOFs, shortlist two graphite-based filler materials from recent literature which are expected to result in the highest conductivity-to-weight fraction ratio, with an acceptable level of cost-effectiveness on a commercial scale. These have been observed to be graphene nanoplatelets (GNPs) and multiwalled carbon nanotubes (MWCNTs).
3. Acid-treat each of the selected filler materials to create surface-active functional sites which can improve the integration of the filler as well as its cohesive strength with the surrounding MOF matrix.
4. Incorporate gradually increase weight fractions of each of the two fillers in each of the two MOF matrices using an *in-situ* synthesis procedure which maximizes the dispersiblity of filler particles as well as the mutual bond strength between the two entities.
5. Characterize each of the four types of synthesized and activated MOF-based composites for degree of crystallinity, microstructure, thermal stability, functional-group chemistry, water adsorption behavior, and hydrothermal cyclic stability.
6. Select the composite material with appropriate weight fraction of the respective filler material which, while retaining the underlying lattice chemistry of the base MOF, not only results in the most commercially feasible compromise between water adsorption kinetics and hydrothermal cyclic stability, but also the highest level of cooling performance amongst the conventionally used adsorbents in a commercially designed chiller application.

CHAPTER 3

SYNTHESIS AND CHARACTERIZATION METHODS

3.1. Introduction

This chapter presents the fabrication routes adopted in this research work for the synthesis of neat as well as graphene-modified MOF materials, followed by a summary of the various characterization methods utilized for the evaluation of morphology, properties, and performance in view of the intended application.

3.2. Synthesis methods

This section briefly describes the methods adopted for the step-wise synthesis of MOF-based composite adsorbents. The first step in this sequence is the covalent side-wall functionalization of two selected graphene nanostructures, i.e., multiwalled carbon nanotubes (MWCNTs) and graphene nanoplatelets (GNPs), while the second step is the *in-situ* incorporation of MWCNTs or GNPs during the synthesis of the two MOFs selected in this study namely MIL-100(Fe) and MIL-101(Cr).

3.2.1. Covalent sidewall functionalization

The covalent sidewall functionalization of MWCNTs and GNPs can be carried out by a variety of methods [142]. However, since the objective of adding either of these two materials for the current research is to improve the intrinsic thermal conductivity of MIL-

100(Fe) and MIL-101(Cr), appropriate functionalization methods have to be selected in order to preserve the aspect ratio and molecular perfection of both MWCNTs and GNPs to the maximum extent possible. In order to achieve this purpose, nitric acid oxidation has been selected for both these materials [143–144] since carboxylation using a mixture of sulfuric and nitric acids is known to drastically damage the intrinsic structure of graphene [145].

3.2.2. Covalent sidewall functionalization of MWCNTs

3 g MWCNTs were first dispersed in 200 ml concentrated HNO_3 using ultrasonication. The suspension was then transferred to a 250 ml round bottom flask equipped with a condenser and was refluxed at 120^{o}C for 48 hours. After cooling down to room temperature, the suspension was then diluted with around 500 ml deionized water and then filtered through a 2.5 μm polymeric membrane under vacuum. The filtered cake was washed repeatedly with deionized water till the pH of the filtrate reached approximately 5. The filtered cake was dried at 80^{o}C in air for 24 hours and ground for further use.

3.2.3. Covalent sidewall functionalization of GNPs

3 g GNPs were first dispersed in 300 ml concentrated HNO_3 using ultrasonication. The suspension was then transferred to a 500 ml round bottom flask equipped with a condenser and was refluxed at 60^{o}C for 2 hours. After cooling down to room temperature, the suspension was then diluted with 200 ml of deionized water and then washed repeatedly with deionized water *via* centrifugation till the pH of the decanted water after each centrifuge cycle reached almost 5.5 (atleast 6 cycles were needed). The solid thus obtained was dried at 80^{o}C in air for 24 hours and ground for further use. The functionalization of

GNPs results in the formation of graphene oxide [144], which is referred to as "GO" in the rest of the text.

3.2.4. Synthesis of MIL-100(Fe) and MIL-100(Fe) composites

A number of methods have so far been reported for the synthesis of MIL-100(Fe), which either incorporate hydrated Fe-salts (usually nitrate or chloride) as MOF precursors [136,143,146–147], or direct chemical reaction of Fe powder with the organic linker during a hydrothermal synthesis procedure [136,143,148–151]. The use of metal salts has been used exclusively for obtaining fluorine-free MIL-100(Fe), while Fe powder has been used to obtain both fluorinated and fluorine-free structures. However, the advantage of using Fe-salt is its chemical dissociation in water producing Fe^{2+} (or Fe^{3+}) ions which in turn develop chemical bonds with the negatively charged carboxyl ($COOH^{1-}$) groups on the functionalized MWCNT/GNP surfaces. The electrostatic attraction between the oppositely charged species in aqueous suspension is believed to later develop into a covalent bond which serves as the chemical interface between the MWCNTs/GNPs and the MOF matrix. Hence, the evolution of this interfacial bonding during the *in-situ* synthesis of MOF composites is not possible if metallic powder is used as precursor for the MOF matrix.

The method of Seo et al. [136] has been adopted for the synthesis of MIL-100(Fe). Briefly, 4.04 g $Fe(NO_3)_3.9H_2O$, 1.4097 g 1,3,5 benzenetricarboxylic acid (BTC) and 50.2 ml de-ionized water were added to a 125 ml Teflon-liner which was sealed inside a stainless steel autoclave and kept at 160^oC for 14 hours. The autoclave was cooled slowly to room temperature, after which the dark orange solid was recovered using centrifugation at 8000 RPM for 45 minutes. In order to remove the guest molecules, the as-synthesized MIL-100(Fe) was further purified following double-solvent extraction using ethanol and water,

and finally using aqueous NH_4F solution. The dried solid was first immersed in deionized water (1g:60ml) and the resulting suspension was stirred at 70^oC for 5 hours. The suspension was again centrifuged and the procedure was repeated using ethanol (1g:60ml) at 65^oC for 3 hours. This two-step purification was continued till the decanted solvent following centrifugation became completely colorless, after which the solid was immersed in 38mM aqueous NH_4F solution and stirred at 70^oC for 5 hours (1g:150ml). The suspension was centrifuged, after which the solid was washed 5 times with deionized water at 60^oC, and finally dried in air at 75^oC for 2 days and 95^oC for 2 days.

For the synthesis of MWCNT/MIL-100(Fe) composites, 4.04 g $Fe(NO_3)_3.9H_2O$ and a pre-determined amount of functionalized MWCNTs were mixed thoroughly in solid-state until a uniform color of the mixture was achieved. 5 ml of de-ionized water was then added periodically to the mixture and the resulting paste was ultrasonicated till the water was completely vaporized. The dried paste, along with 1.4097 g BTC and 50.2 ml de-ionized water, were then transferred completely to a 125 ml Teflon-lined autoclave which was kept at 160^oC for 14 hours. The post-synthesis purification procedure was exactly the same as the one adopted for unmodified MIL-100(Fe). GO/MIL-100(Fe) composites were synthesized in exactly the same way. However, in case of GO/MIL-100(Fe) composites, the MIL-100(Fe) crystals are observed to be wrapped by the GO sheets as a result of hydrothermal synthesis in order to attain a minimum energy configuration unlike the MWCNT/MIL-100(Fe) composites in which the MWCNTs are observed to be implanted inside the crystals. The *in-situ* synthesis of MIL-100(Fe) composites, starting with a single representative MWCNT and GNP, are summarized schematically in Figures 3.1 and 3.2, respectively.

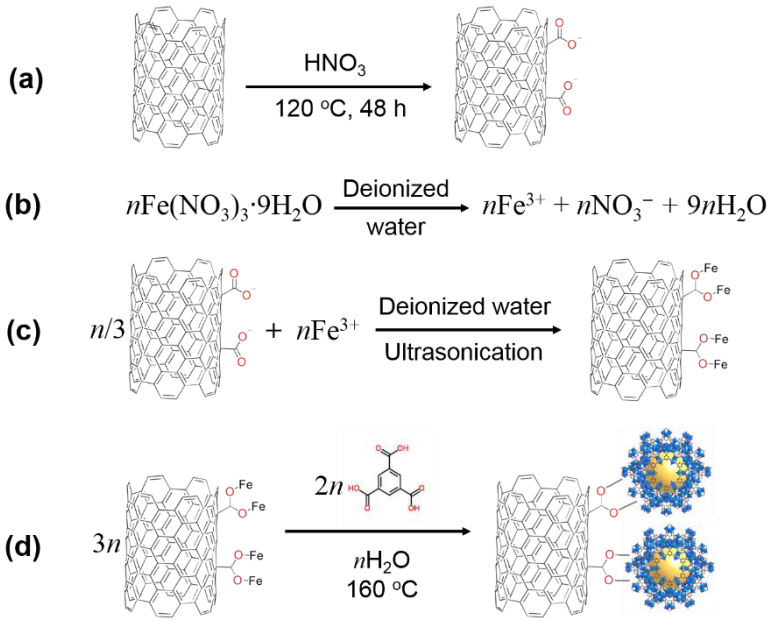

Fig 3.1: *In-situ* synthesis of MWCNT/MIL-100(Fe) composite starting with a single representative MWCNT: **(a)** MWCNT carboxylation, **(b)** Dissociation of hydrated Fe-salt in deionized water, **(c)** Sonication-assisted electrostatic attraction of $COOH^{-1}$ groups on MWCNT and Fe^{3+} ions in aqueous solution, **(d)** Hydrothermal synthesis of MIL-100(Fe) crystals on the surface of MWCNT.

3.2.5. Synthesis of MIL-101(Cr) and MIL-101(Cr) composites

For the synthesis of MIL-101(Cr) and MIL-101(Cr) composites, the method proposed by Férey et al. [39] has been adopted. Briefly, 4 g $Cr(NO_3)_3.9H_2O$, 1.66 g 1,4 benzenedicarboxylic acid (BDC) and 47.4 ml de-ionized water were added to a 125 ml Teflon-liner which was sealed inside a stainless steel autoclave and kept at 220°C for 8 hours. The autoclave was then cooled slowly to room temperature, after which the light green solid was recovered using centrifugation at 8000 RPM for 45 minutes. In order to remove the guest molecules, the as-synthesized MIL-101(Cr) was washed twice with 90

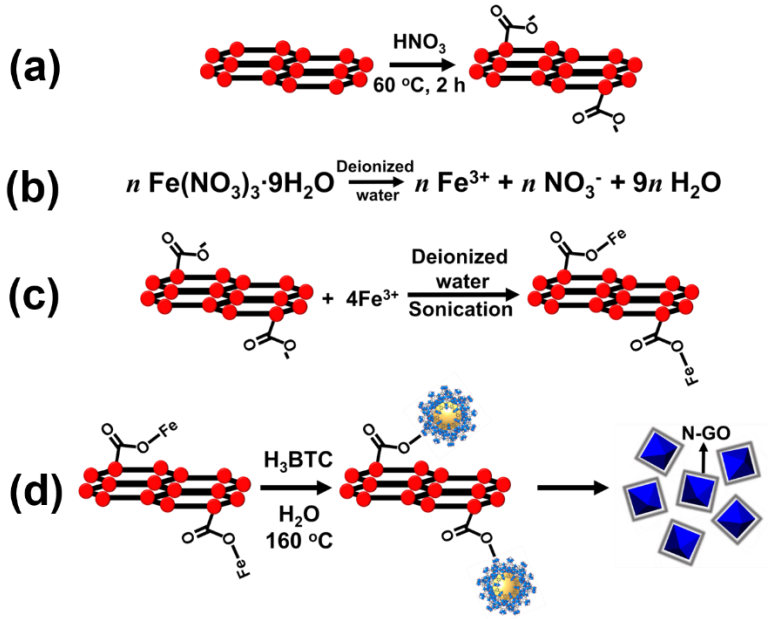

Fig 3.1: *In-situ* synthesis of GO/MIL-100(Fe) composite starting with a single representative GNP: **(a)** GNP carboxylation resulting in GO, **(b)** Dissociation of hydrated Fe-salt in deionized water, **(c)** Sonication-assisted electrostatic attraction of $COOH^{-1}$ groups on GO and Fe^{3+} ions in aqueous solution, **(d)** Hydrothermal synthesis resulting in GO-wrapped MIL-100(Fe) crystals on the surface of GO sheet.

ml deionized water and further purified 5 times using an 80% aqueous solution of ethanol, till the decanted solvent following centrifugation became completely colorless. The green solid was then immersed in 30mM aqueous NH_4F solution and stirred at 60°C for 10 hours (1g:150ml). The suspension was centrifuged, after which the solid was washed 5 times with deionized water at 60°C. The green solid was then washed three times with 70 ml DMF, and 5 times with 75 ml deionized water, and finally dried in air at 75°C for 2 days and 95°C for 2 days.

For the synthesis of MWCNT/MIL-101(Cr) composites, 4 g $Cr(NO_3)_3.9H_2O$ and a pre-determined amount of functionalized MWCNTs were mixed thoroughly in solid-state until a uniform color of the mixture was achieved. 5 ml of de-ionized water was then added periodically to the mixture and the resulting paste was ultrasonicated till the water was completely vaporized. The dried paste, along with 1.66 g BDC and 47.4 ml de-ionized water, were then transferred completely to a 125 ml Teflon-lined autoclave which was kept at 220^{o}C for 8 hours. The post-synthesis purification procedure was exactly the same as the one adopted for unmodified MIL-101(Cr). GO/MIL-101(Cr) composites were synthesized in exactly the same way. The *in-situ* synthesis of MIL-101(Cr) composites, starting with a single representative MWCNT or GNP, can be represented in exactly the same way as shown for the MIL-100(Fe) composites in Figures 3.1 and Figure 3.2, with the only exceptions of replacing $Fe(NO_3)_3.9H_2O$ by $Cr(NO_3)_3.9H_2O$, BTC by BDC, and the synthesis temperature of 160^{o}C by 220^{o}C.

3.3. Characterization methods

The synthesized and activated MOF materials are characterized by a variety of techniques in order to predict the effects of functionalized MWCNT/GNP addition on the intrinsic surface area, crystallinity, morphology, water adsorption-desorption characteristics, thermal conductivity, and hydrothermal cyclic stability of the base MOFs. The following discussion summarizes the different techniques that will be employed for the characterization of activated MOFs and their composites, and the types of useful information which can be obtained using each technique.

3.3.1. Powder X-ray Diffraction (PXRD)

The synthesized and activated MOF materials are characterized using PXRD for evaluating the effects of MWCNT/GNP addition on the intrinsic crystal structure and the degree of crystallinity of both MIL-100(Fe) and MIL-101(Cr), each of which is already published in literature [152–153]. In this study, PXRD patterns have been acquired with a Rigaku Miniflex Multipurpose Diffractometer equipped with a Ni β-filter. Prior to each analysis, the powder samples are packed densely in a 0.6 mm deep groove on a background-proof holder. In order to preserve the constant volume pre-requisite before starting the analysis, programmable divergence slits have been employed for illuminating a fixed length of the samples which is held constant at 8 mm. The powder samples are irradiated with a CuKα radiation with a constant operating power of the diffractometer set at 45 kV and 40 mA. The diffraction data has been collected at constant regular intervals between 3^o and 50^o for MIL-100(Fe), and between 3^o and 30^o for MIL-101(Cr) with the same scan rate of $0.3^o min^{-1}$ for both types of materials.

3.3.2. Brunauer-Emmett-Teller (BET) surface area analysis

In order to investigate the effects of MWCNT/GNP addition on the intrinsic specific surface area of each of MIL-101(Cr) and MIL-100(Fe), BET surface area analysis is employed. Since the characteristic surface areas of both these MOFs are already reported in literature [39,136], this characterization technique is helpful in determining the effect of MWCNT/GNP addition on the intrinsic water adsorption capacity of each of these materials. In this study, BET surface area measurements have been conducted using a Quantachrome Autosorb iQ/ASiQwin apparatus at liquid nitrogen temperature (77 K). The powder sample is degassed at 393 K under vacuum for 17 hours for MIL-100(Fe), and at

423 K for 12 hours for MIL-101(Cr) before commencement of each adsorption experiment. The specific surface areas have been evaluated within a p/p_0 range of 0.06–0.2, while the pore volumes have been evaluated using a single-point method at p/p_0 = 0.9.

3.3.3. Fourier Transform Infrared Spectroscopy (FTIR)

The objective of FTIR is twofold – (*a*) identification of functional groups on the surface of functionalized MWCNTs/GNPs which have already been reported in literature [142,154], and (*b*) identification of the appearance of any new functional groups that might have formed during the *in-situ* chemical synthesis of each of the four types of composites. In the current study, FTIR spectra have been recorded on a thermo scientific Nicolet 6700 Fourier transform infrared spectrometer (Thermo Fisher Scientific), while sample preparation has been performed using KBr pellets containing a total sample amount of 2–3 mg.

3.3.4. Thermogravimetric Analysis (TGA)

Thermogravimetric analysis is carried out to record the weight loss of a sample in with gradual increase in its temperature at a constant rate, or with a gradual increase in time at a constant sample temperature. In this study, the main purpose of conducting TGA is to assess the effect of MWCNT or GNP addition on the thermal stability of MIL-100(Fe) and MIL-101(Cr). For this study, TGA has been carried out with a model SDT Q600 V20.9 Build 20 Thermogravimetric Analyzer (TA instruments, Inc.) between 298 K and 1073 K at 3^{o}C/min under air flow for MIL-100(Fe), and under nitrogen flow for MIL-101(Cr).

3.3.5. Scanning Electron Microscopy (SEM) and Transmission Electron Microscopy (TEM)

The morphologies of both MIL-100(Fe) and MIL-101(Cr), and their respective composites with MCNTs/GNPs, are observed using SEM and TEM. The features that can be explored using each of these two methods is the uniformity of MWCNT/GNP dispersion in the MOF matrix, and whether the MWCNTs are implanted inside the MOF particles, as expected of the designed synthesis method, or simply lie on their surfaces which is not the intended objective of the synthesis procedure. In this study, TEM and SEM have been performed on a JEOL JEM-2100F/HR transmission electron microscope, and TESCAN LYRA3 FEG scanning electron microscope, respectively. TEM samples are prepared by pouring drops of the as-synthesized MOF suspension in acetone or ethanol on carbon-coated 200 mesh Cu-grids, while the TEM images are obtained at an accelerating voltage of 120 kV. SEM samples are prepared by pouring drops of the as-synthesized MOF suspension in ethanol or acetone on Cu tapes followed by solvent drying, and the images are obtained at an accelerating voltage of 5 kV and a working distance of 5–6 mm using a standard secondary electron (SE) detector.

3.3.6. X-ray Photoelectron Spectroscopy (XPS)

XPS is primarily a surface analysis technique which measures the energy of electrons emitted from the core atomic levels. The XPS instrument is programmed to measure the binding energy of the photoelectrons emitted from the core levels of the various constitutive elements which are characterized by distinctive oxidation states and chemical affiliations. Since formation of a covalent bond between a metallic and a non-metallic species increases the oxidation number of the former and decreases the oxidation number of the latter, this shift in the oxidation state measured by the XPS instrument is extremely

helpful in identifying the organic-inorganic bonds which form during an *in-situ* solvent-assisted chemical synthesis of an organic-inorganic hybrid composite. In this work, the main purpose of XPS is to characterize the nature of interfacial bonding between the metal ion centers within the framework and the MWCNTs which are incorporated *in-situ* during the hydrothermal synthesis of the MWCNT/MOF composites. In this study, XPS measurements have been performed on a Thermo Scientific ESCALAB 250Xi X-ray photoelectron spectrometer.

3.3.7. Water sorption isotherms and hydrothermal cyclic stability

The characteristic water adsorption-desorption isotherms of both MIL-100(Fe) and MIL-101(Cr) are well established and reported in a number of publications [17,45,47–48,134,155]. The degrees of shift in the shape and the hysteresis of the water adsorption-desorption isotherms will be indicative of the effects of MWCNT/GNP addition on the water adsorption-desorption behavior of each of these two compounds. Hydrothermal cyclic stability of a MOF-based adsorbent ensures that it not only retains its structural stability during the hydrothermal cycling process, but also maintains the water adsorption capacity during the operation of the adsorption chiller. In order to evaluate the hydrothermal cyclic stability, the MOF materials will be subjected to continuous adsorption/desorption cycles between 40 and 140 °C, under a water vapor pressure of 5.2 kPa. The shift in the water adsorption capacity is then recorded with the increasing number of continuous cycles. For recommended use in a commercial adsorption chiller, the adsorbent is expected to show more or less constant water loading lift for a large number of continuous cycles (typically more than 50,000). The instrumentation and typical outcomes of a hydrothermal cyclic stability test can be found in [47,120,155–156].

Both water adsorption-desorption isotherms and hydrothermal cyclic stability in this study have been measured using DVS vacuum (Surface Measurement Systems, Inc., London, U.K.). The samples were degassed under vacuum at 120 °C for 15 h prior to commencing the appropriate experiments. For the cycling tests, samples were subjected to 21 successive ad-/desorption cycles between 40 °C and 140 °C at 5 h per cycle and a constant vapour pressure of 5.6 kPa. The time-temperature profile used for the test is as follows: heating from 40 °C to 140 °C at 5 °C min^{-1}, followed by a constant-heating step at 140 °C for 150 min to facilitate complete desorption, cooling back to 40 °C at 5 °C min^{-1} to commence water adsorption, and finally an isothermal stay at 40 °C for 200 min to allow for complete adsorption.

CHAPTER 4

EXPERIMENTAL RESULTS AND DISCUSSION

4.1. Pristine and functionalized MWCNTs

Figure 4.1 shows the FTIR spectra of pristine (as-received) and functionalized MWCNTs. The peak observed at 3450 cm^{-1} corresponds to the O–H stretch of the carboxyl groups (C–OH and O=C–OH), while the peak evidenced around 2365 cm^{-1} is assignable to the O–H stretch of the –COOH groups with covalent hydrogen bonding [157]. The peak at 1565 cm^{-1} is attributed to the stretching vibration of the carboxylate anion. The peaks at around 2880 and 2935 cm^{-1} are assigned to the C–H stretch modes of O=C–H in the carboxyl functionality. The peak evidenced around 1640 cm^{-1} can be attributed to the stretching of the MWCNT backbone [158]. Figure 4.2 shows the SEM micrographs of both pristine and functionalized MWCNTs. As clearly evident, the acid-treatment process used for functionalization has resulted in disentanglement of nanotube bundles which is expected to lead to an improved dispersion of MWCNTs during the synthesis of the MWCNT/MIL-100(Fe) composite.

4.2. MWCNT/MIL-100(Fe) composite

Figure 4.3 shows the SEM micrographs of as-synthesized MIL-100(Fe) and MWCNT/MIL-100(Fe) composites. The octahedral-shaped crystals characteristic of the MIL-100(Fe) lattice are evident in Figure 4.3(a). However, a significant degree of variation can be seen in the size of the crystals which is observed to lie between 50 nm and 500 nm in terms of diameter. The incorporation of MWCNTs preserves the shape of the crystals as

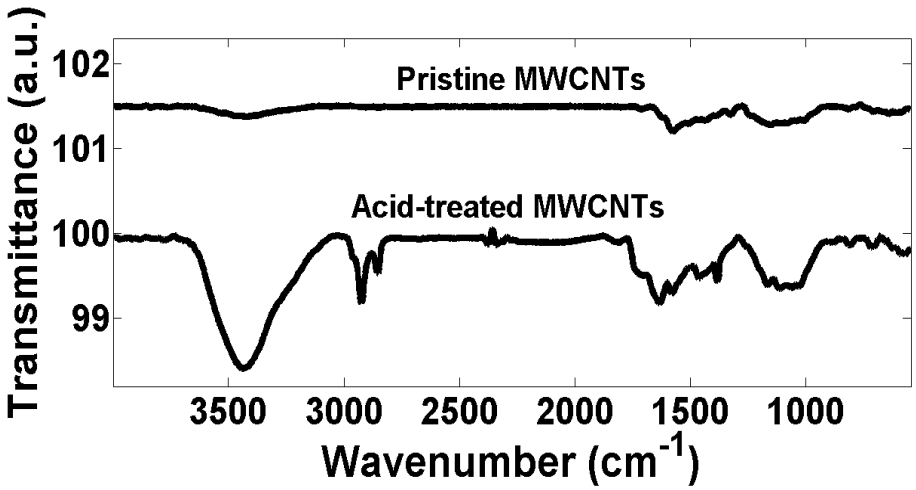

Fig 4.1: FTIR spectra of pristine and acid-treated (functionalized) MWCNTs.

shown in Figure 4.3(b). The MWCNTs can also be seen implanted in the surrounding MIL-100(Fe) matrix, which is a consequence of the molecular-level interaction of negatively charged carboxyl groups on MWCNTs and Fe^{3+} ions in aqueous solution during the *in-situ* synthesis of the composite (Figure 3.1(b–d)). As opposed to simple physical mixing of MWCNTs with already synthesized MIL-100(Fe), the implantation of carbon nanotubes is a necessary pre-requisite required to improve the heat transfer rate within the MIL-100(Fe) matrix.

Figure 4.4 shows the TEM micrographs of as-synthesized MIL-100(Fe) and the MWCNT/MIL-100(Fe) composites. Since the electron beam used in TEM transmits through the thickness of the sample, the cross-section of one of the octahedral crystals of MIL-100(Fe) shown in Figure 4.3(a) can be clearly seen in Figure 4.4(a). Moreover, TEM can also be used to reveal the micropores within the MIL-100(Fe) framework represented by the bright-colored spots uniformly distributed across the entire cross-section of the

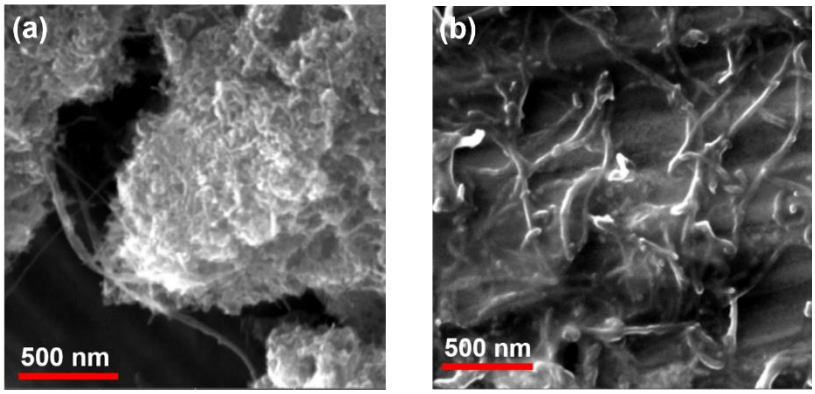

Fig 4.2: SEM micrographs of **(a)** pristine MWCNTs, and **(b)** acid-treated MWCNTs.

crystals. The mean dimension of these spots was found to be equal to 2.6 nm, which is in excellent agreement with the size of the mesoporous cages characteristic of the MIL-100(Fe) structure [159]. Figure 4.4(b) re-confirms the implantation of MWCNTs in the MOF matrix which can be clearly seen as tubular structures implanted across the crystals of MIL-100(Fe) in accordance with the protocol proposed for the synthesis of MWCNT/MIL-100(Fe) composites (Figure 3.1).

Figure 4.5 shows the nitrogen physiosorption isotherms of MIL-100(Fe) as well as MWCNT/MIL-100(Fe) composite with 3 different weight fractions of MWCNTs. It can be clearly seen that increasing the content of carbon nanotubes in the MIL-100(Fe) matrix does not alter the adsorption kinetics since all the plots clearly reveal a type IV isotherm shape. Moreover, the incorporation of MWCNTs does not introduce any hysteresis between the adsorption and the desorption phases as characteristic of the pure MIL-100(Fe) structure. Hence, the implantation of nanotubes within the MIL-100(Fe) crystals does not result in deformation of the framework by virtue of the guest-host interactions occurring

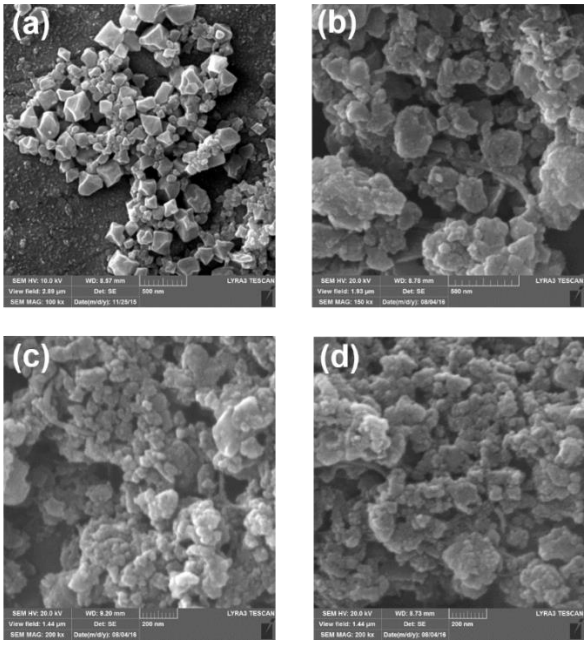

Fig 4.3: SEM micrographs of MWCNT/MIL-100(Fe) composites – **(a)** 0 wt% MWCNTs, **(b)** 2.16 wt% MWCNTs, **(c)** 5.9 wt% MWCNTs, and **(d)** 10.72 wt% MWCNTs.

during adsorption-desorption of gas molecules. However, simple physical mixing of MWCNTs with already synthesized and activated MIL-100(Fe) is expected to result in a certain degree of hysteresis during uptake of guest molecules since nanotubes are not implanted within the framework in this case. The specific surface area for MIL-100(Fe) was calculated using the best fit of the nitrogen sorption isotherm to the BET equation and was found to be equal to 1360 m^2g^{-1} which is in agreement with the already published result for MIL-100(Fe) synthesized using the same method [136]. For the MWCNT/MIL-100(Fe) composite, the specific surface areas for different weight fractions of MWCNTs were calculated as follows: 1193 m^2g^{-1} (3.74 wt%), 1047 m^2g^{-1} (8.13 wt%), 1029 m^2g^{-1} (8.99

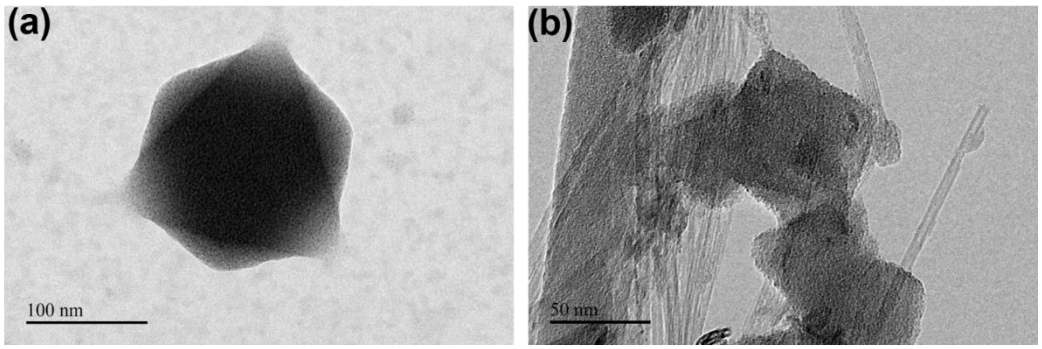

Fig 4.4: TEM micrographs of **(a)** MIL-100(Fe), and **(b)** MWCNT/MIL-100(Fe) composite.

wt%), 1071 m^2g^{-1} (13.99 wt%), and 630 m^2g^{-1} (17.70 wt%) (Table 4.1). The synthesized MWCNT/MIL-100(Fe) composites are referred to as MIL-100-C*n* with *n* from 1 to 5 corresponding to the respective amounts of MWCNTs added initially to MIL-100(Fe) precursors (60 mg, 180 mg, 120 mg, 300 mg, and 240 mg respectively).

Figure 4.6 shows the PXRD profiles of MWCNT/MIL-100(Fe) composite with various weight fractions of MWCNTs. It can be seen that the PXRD profile of MIL-100(Fe) is in very good agreement with the one reported in literature for similar method used for the synthesis [160], as well as the simulated pattern shown in Figure 4.6. The incorporation of MWCNTs does not result in any noticeable peak shift or decrease in the crystallinity of the framework, as all the characteristic peaks representative of the MIL-100(Fe) structure can also be observed in the patterns shown for each category of MWCNT/MIL-100(Fe) composite. However, a slight reduction in the peak intensities can be seen in the PXRD pattern of MIL-100-C-5 as a consequence of the excessive chemical coordination of the functional groups on the surface of MWCNTs with the oppositely charged metal ion

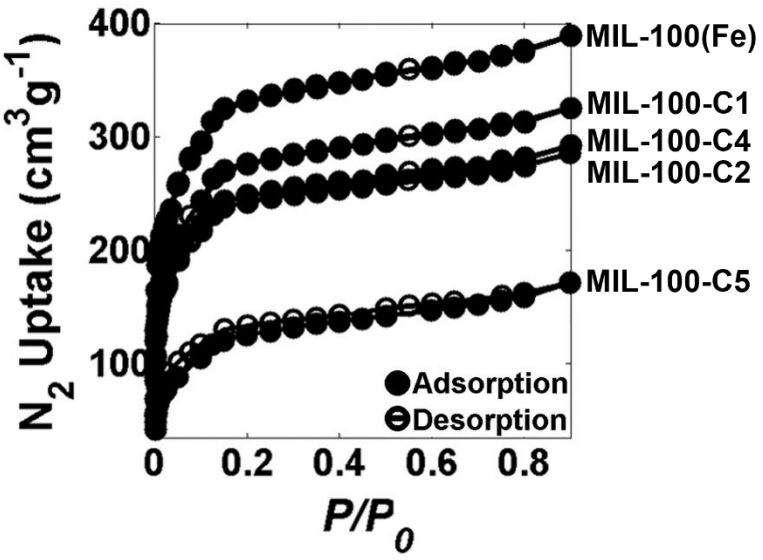

Fig 4.5: Nitrogen physiosorption isotherms for MIL-100(Fe) and MWCNT/MIL-100(Fe) composites.

centers in the MIL-100(Fe) framework. Hence, it can be concluded that the incorporation of MWCNTs up to 18 wt% using an *in-situ* synthesis method preserves the characteristic crystal lattice of the MIL-100(Fe) framework, despite the presence of a chemical interface between the nanotubes and the surrounding MOF matrix. It can be observed from Figure 4.6 that for $2\theta = 24.5–50^{o}$, 5 additional peaks are observed in the PXRD profiles of MIL-100(Fe) and MWCNT/MIL-100(Fe) composites which are absent in the profile of the simulated pattern. As clearly depicted in Figure 4.7, these 5 peaks correspond to the presence of α-Fe_2O_3 in the samples which forms during synthesis due to variations in the pH of the reaction mixture. For completely avoiding the formation of α-Fe_2O_3, the pH should remain acidic throughout the synthesis [136].

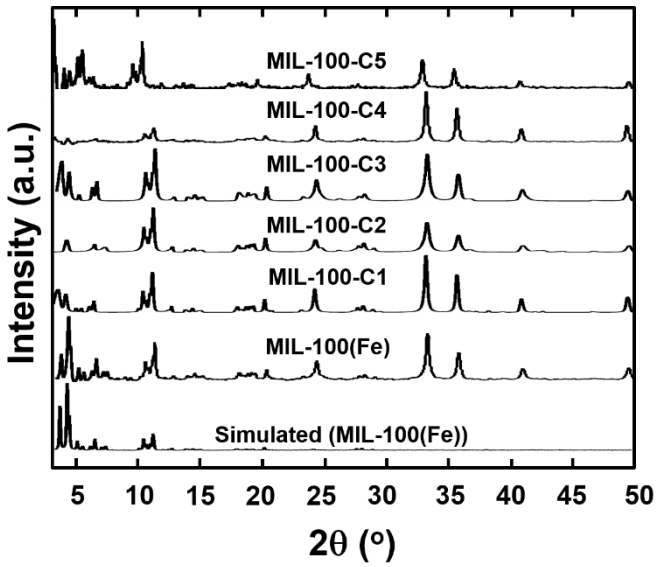

Fig 4.6: PXRD patterns for MIL-100(Fe) and MWCNT/MIL-100(Fe) composites.

Figure 4.8 shows the TGA results of acid-treated MWCNTs, MIL-100(Fe) and MWCNT/MIL-100(Fe) composites. For MIL-100(Fe), the TGA curve exhibits three major weight losses spread between 30 and 700^{o}C. However, for the composite materials, an additional weight loss is observed owing to the presence of MWCNTs in the framework. An initial weight loss between 30 and 60^{o}C corresponds to the removal of water molecules trapped inside the pores within the MIL-100(Fe) framework. The second weight loss spread between 60^{o}C and 297^{o}C represents the evaporation of water molecules coordinated to the Fe-trimers. The abrupt weight loss of 32.23% observed between 297^{o}C and 353^{o}C in the TGA profile of MIL-100(Fe) is assigned primarily to linker decomposition within the framework [136]. However, the linker decomposition start and end temperatures were observed to vary with the changing content of MWCNTs in MWCNT/MIL-100(Fe) composites. In general, it was noticed that the temperature at which the linker

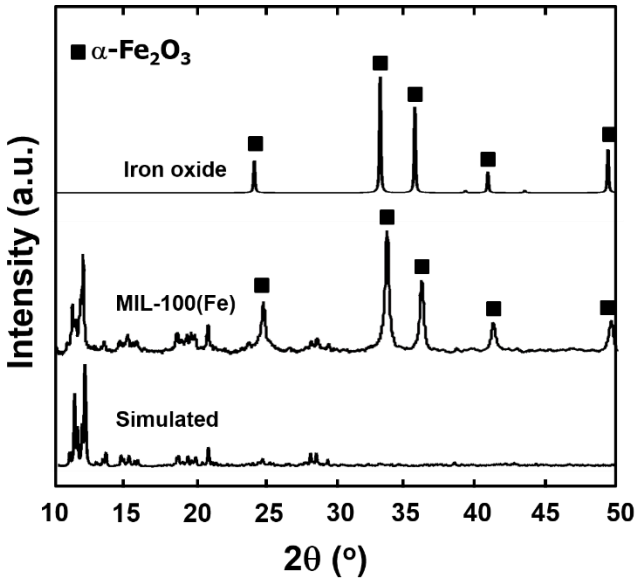

Fig 4.7: Qualitative confirmation of existence of α-Fe_2O_3 in MIL-100(Fe) and MWCNT/MIL-100(Fe) composites.

decomposition ends (or the MWCNT oxidation begins) shifts to lower values with increasing content of MWCNTs in the composites. Above the linker decomposition end temperature up to the final analysis temperature of 700^{o}C, the weight loss occurring in all the composite samples is assigned primarily to the oxidation of MWCNTs with a negligibly small contribution corresponding to the decomposition of the remaining linker. The residual weights observed for each sample at 700^{o}C is 55.3% (MIL-100(Fe)), 59.3% (MIL-100-C1), 49% (MIL-100-C2), 43.9% (MIL-100-C3), 45.7% (MIL-100-C4), and 48.7% (MIL-100-C5). From the TGA data, the amount of MWCNTs inside each composite can be evaluated. Since the amount of residual MWCNTs at the end of TGA was observed to be 0.75%, the content of MWCNTs in each composite can be estimated as:

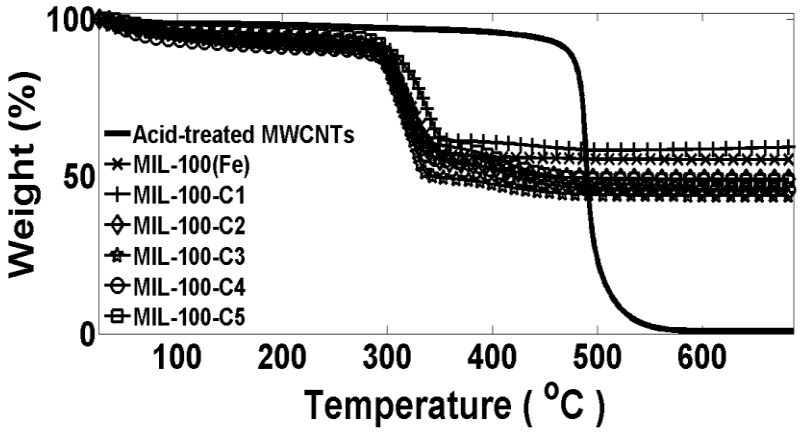

Fig 4.8: TGA curves for acid-treated MWCNTs, MIL-100(Fe), and MWCNT/MIL-100(Fe) composites.

$$\textbf{MWCNTs (wt\%)} = \left\{\left[\textbf{W.L.}_{T_{L-O_2}\rightarrow 700^{o}C}^{comp} - \textbf{W.L.}_{353^{o}C\rightarrow 700^{o}C}^{MIL-100(Fe)}\right] + \mathbf{0.75}\right\} \times \frac{\mathbf{100}}{\mathbf{M_w}} \qquad (4.1)$$

where $\mathbf{T_{L-O_2}}$ is the temperature at which linker decomposition ends or MWCNT oxidation begins during TGA, $\textbf{W.L.}_{T_{L-O_2}\rightarrow 700^{o}C}^{comp} = \mathbf{W}_{T_{MWCNTs-O_2}}^{comp} - \mathbf{W}_{700^{o}C}^{comp}$ stands for the weight loss between $\mathbf{T_{L-O_2}}$ and 700°C expressed as a percentage of the initial weight, and the superscript "comp" denotes MWCNT/MIL-100(Fe) composite. The weight loss for MIL-100(Fe) between 353 and 700°C was measured to be equal to 1.8148 wt%, i.e. $\textbf{W.L.}_{353^{o}C\rightarrow 700^{o}C}^{MIL-100(Fe)}$ = 1.8148%. In Equation (4.1), the term $\mathbf{M_w}$ stands for the weight percentage of anhydrous MIL-100(Fe) in each sample which excludes the content of iron-oxide (α-Fe_2O_3) impurity. Since the chemical formula of anhydrous MIL-100(Fe) is $Fe_3O(OH)[C_6H_3(CO_2)_3]_2$ with a molar mass of 614.78 $gmol^{-1}$ [148], the weight percentage of Fe atoms in anhydrous MIL-100(Fe) is given as $\frac{3\times 55.845\ gmol^{-1}}{614.78\ gmol^{-1}}\times 100 = 27.25\%$, where the remaining 72.75% accounts for the organic linker. Since the weight loss between

297°C and 700°C in the TGA profile of MIL-100(Fe) is assigned to linker decomposition of approximately 34.06%, the corresponding weight percentage of Fe atoms in proportion to this linker content is expressed as $\frac{27.25}{72.75}\times 34.06 = 12.76\%$. Hence, the corresponding content of α-Fe_2O_3 formed by the oxidation of this percentage of Fe atoms is expressed as $\frac{12.76\left[2\left(55.845\right)+3\left(16\right)\right]}{2\left(55.845\right)} = 18.24\%$. Since the post-TGA α-Fe_2O_3 residue in the TGA profile of MIL-100(Fe) accounts for almost 55.3%, the actual weight percentage of anhydrous MIL-100(Fe) can thus be found as: $\mathbf{M}_{\mathbf{w}} = 100 - \left(55.3 - 18.24\right) = 62.91\%$. In a similar fashion, the value of $\mathbf{M}_{\mathbf{w}}$ can be calculated for the MWCNT/MIL-100(Fe) composites with various weight fractions of MWCNTs. Table 4.1 lists the detailed calculation of MWCNT content in each composite using Equation (4.1).

Figure 4.9 shows the FTIR spectra for MIL-100(Fe) as well as MWCNT/MIL-100(Fe) composite with various weight fractions of MWCNTs. The vibrational bands evidenced around 1460, 1379, 765, and 717 cm^{-1} are characteristic of the MIL-100(Fe) framework [160], while a weak signal observed within 1710–1720 cm^{-1} corresponds to the residual trimesic acid residing within the pores of inside the framework. Finally, the peak at 3445 cm^{-1} visible in the spectra of carbon nanotube- implanted materials is attributable to the O–H stretch of the carboxyl groups (C–OH and O=C–OH) present on the acid treated MWCNTs as shown earlier in Figure 2. More interestingly, a faint shoulder is observed around 510 cm^{-1} in the spectra of MIL-100-C3 to MIL-100-C5, which is totally absent in the spectrum of MIL-100(Fe). This peak corresponds to the Fe– C–O stretching vibration which is a consequence of the chemical coordination formed between the negatively

Table 4-1: Calculation of MWCNT contents in MWCNT/MIL-100(Fe) composites using Equation (4.1).

Sample ID	$T_{L\text{-}O_2}$ (°C)	$W^{comp}_{T_{L\text{-}O_2}}$ (%)	$W^{comp}_{700^oC}$ (%)	$W.L.^{comp}_{T_{L\text{-}O_2}\rightarrow 700^oC}$ (%)	M_w (%)	MWCNTs (wt%)
MIL-100-C1	350	62.5031	59.2829	3.2202	57.71	3.7406
MIL-100-C2	345	55.9593	48.9947	6.9647	72.6	8.1337
MIL-100-C3	334	52.0863	43.9110	8.1753	79.05	8.9996
MIL-100-C4	333	57.4979	45.7181	11.7799	76.62	13.9885
MIL-100-C5	328	62.7789	48.6838	14.0951	73.63	17.7008

charged carboxyl groups on acid-treated MWCNTs, and the positively charged Fe^{+3} ions during *in-situ* synthesis of the composite as shown in Figure 4.10 [161–162]. Hence, the method of synthesis proposed in this study can be engineered to tailor the characteristics of the chemical interface formed between the nanotubes and the surrounding MOF matrix in accordance with the intended application. Moreover, the incorporation of MWCNTs up to 18 wt% in MIL-100(Fe) using the proposed approach does not result in formation of any undesirable functionalities thus preserving the original chemical integrity of the framework.

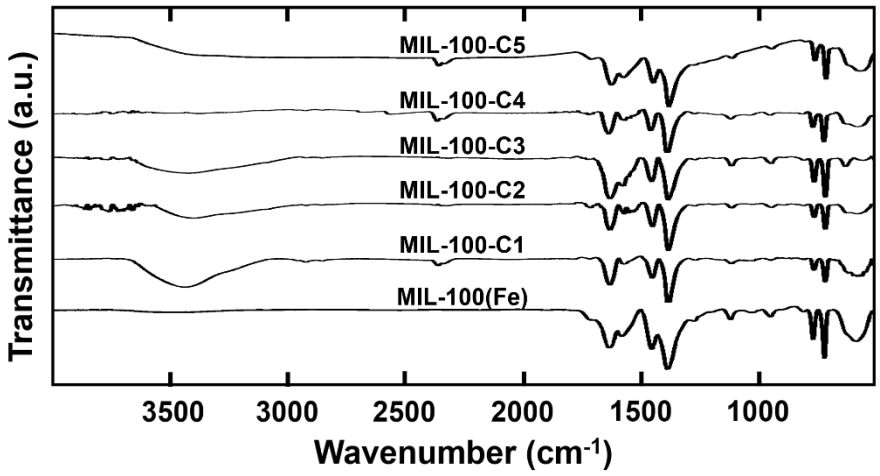

Fig 4.9: FTIR spectra for MIL-100(Fe) and MWCNT/MIL-100(Fe) composites.

In order to further probe the chemistry of the interface between the MWCNTs and the MIL-100(Fe) crystallites, XPS measurements have also been conducted on MIL-100(Fe) and MIL-100-C3. The full surveys of the surface composition for MIL-100(Fe) and MIL-100-C3 show photo electron lines at a binding energy of about 283.15, 530.31 and 710.53 eV, which are attributed to C 1s, O 1s and Fe 2p, respectively, as shown in Figure 4.11 [163]. For MIL-100(Fe), the C 1s peak can be deconvoluted into 3 peaks centered at 282.95, 286.88 and 284.61 eV, representing phenyl, carboxyl, and surface C atoms, respectively, as shown in Figure 4.12 [163]. In case of MIL-100-C3, the peaks corresponding to carboxyl groups and surface C atoms are positioned at more or less the same binding energies as in MIL-100(Fe) as shown in Figure 4.12; however, the peak representing the phenyl group in MIL-100(Fe) is further deconvoluted into two peaks centered at 283.20 and 282.57 eV, which is attributable to the attachment of functional moieties at two distinct positions on benzene ring caused by the shift in the mechanism of formation of MIL-100(Fe) crystals

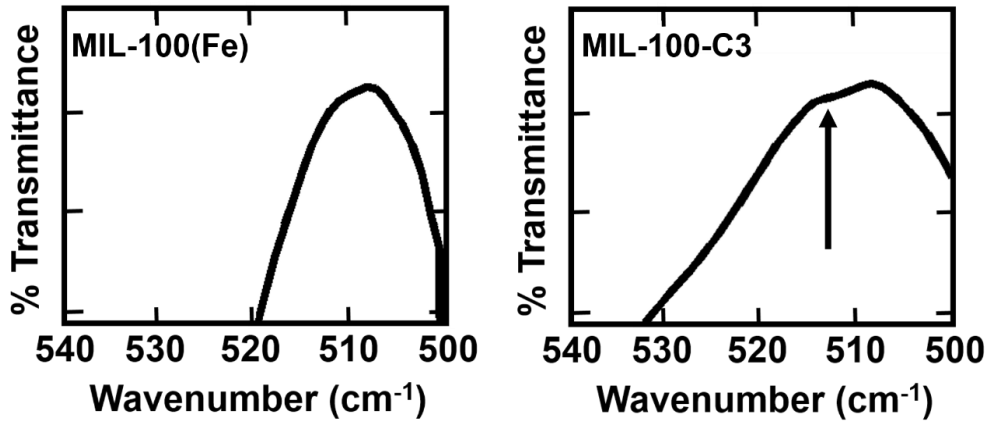

Fig 4.10: Qualitative identification of C–O–Fe bonding in MWCNT/MIL-100(Fe) composites.

occurring due to the introduction of MWCNTs [163–164]. The O 1s peak of MIL-100(Fe) can be deconvoluted into 3 peaks centered at 530.37, 532.29 and 530.20 eV, which correspond to C=O, C–O–Fe and O–Fe bonds, respectively, and are positioned at 530.69, 528.61 and 530.36 eV, respectively, in case of MIL-100-C3 (Figure 4.13). Hence, the peak attributable to C–O–Fe bonds in MIL-100(Fe) framework shifts to a lower binding energy in MIL-100-C3 as the O atoms require additional valence electrons in order to form covalent bonds with Fe atoms, resulting in the interfacial C–O–Fe bonds between the

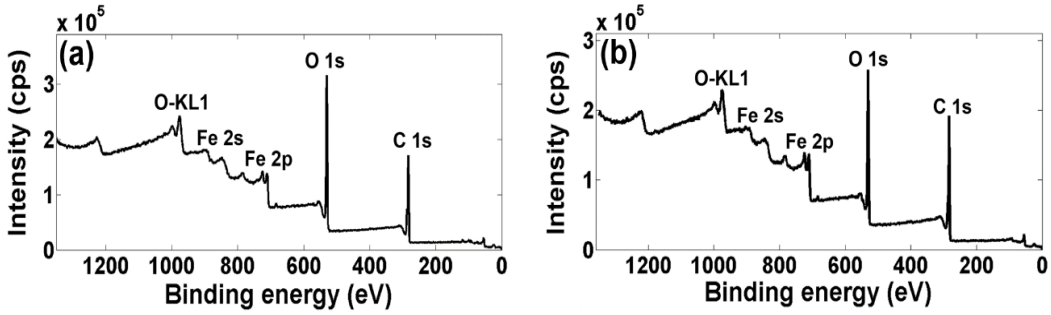

Fig 4.11: Full surveys for XPS spectra of **(a)** MIL-100(Fe) and **(b)** MIL-100-C3.

MWCNTs and the MIL-100(Fe) crystals (Figure 3.1(d)). The Fe 2p peak for MIL-100(Fe) can be deconvoluted into 4 peaks centered at 709.83, 712.12, 724.01 and 715.72 eV, corresponding to the peaks of Fe $2p_{3/2}$, Fe $2p_{1/2}$, and the two satellite peaks of Fe $2p_{1/2}$ and Fe $2p_{3/2}$, respectively, as shown in Figure 4.14 [163]. For MIL-100-C3, the same peaks are observed at 709.65, 711.86, 723.44 and 716.35 eV, respectively. Hence, the satellite peak of Fe $2p_{3/2}$ for MIL-100(Fe) shifts to a higher binding energy in case of MIL-100-C3, since removal of additional valence electrons from Fe atoms to form bonds with $COOH^-$ groups on the surface of acid-treated MWCNTs is expected to increase the binding energy of the core electrons, and correspondingly shift the satellite peak of Fe $2p_{3/2}$ to a higher binding energy [164].

The water adsorption-desorption isotherms at 298 K for MIL-100(Fe) and three types of MWCNT/MIL-100(Fe) composites, MIL-100-C1, MIL-100-C2, and MIL-100-C4, are shown in Figure 4.15. A maximum water vapour uptake of 42.45 wt% is observed for MIL-100(Fe), which drops to 24.72% after the framework is subjected to 21 consecutive water adsorption/desorption cycles as shown in Figure 4.15(a). It can be observed that there is a

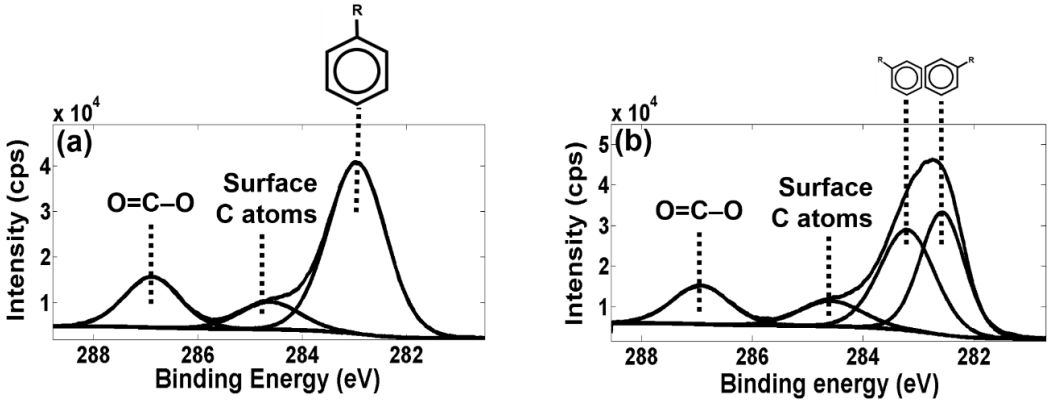

Fig 4.12: Deconvoluted C1s XPS spectra of **(a)** MIL-100(Fe) and **(b)** MIL-100-C3.

steep rise in adsorbed amount for $0.25 < P/P_0 < 0.45$, which is in excellent agreement with already published results [47–48]. At $P/P_0 < 0.25$, mono- as well as multi-layer adsorption of water molecules mainly takes place at the hydrophilic metal ion clusters within the framework. The steep rise observed between $0.25 < P/P_0 < 0.45$ is attributed to capillary condensation which first involves the filling of 25Å mesopores, followed by the filling of 29Å mesopores. For MWCNT/MIL-100(Fe) composites, the maximum uptakes are observed to be 38.77 wt% (MIL-100-C1), 42.96 wt% (MIL-100-C2), and 40.86 wt% (MIL-100-C4). Hence, MIL-100-C2 results in a 1.2% higher maximum water vapor uptake than MIL-100(Fe) at 298 K despite the intrinsic hydrophobic nature of MWCNTs. This is attributable to a relatively higher nucleation rate of MIL-100(Fe) on the surface of MWCNTs resulting in a relatively larger number of crystals, and consequently greater number of sites available for water adsorption. However, on exceeding a critical weight fraction, the intrinsic hydrophobicity of MWCNTs supersedes the effect of the higher nucleation rate of MIL-100(Fe) crystals thus again causing a reduction in the maximum water vapor uptake. The other factor that might lead to lower water vapor uptake at higher

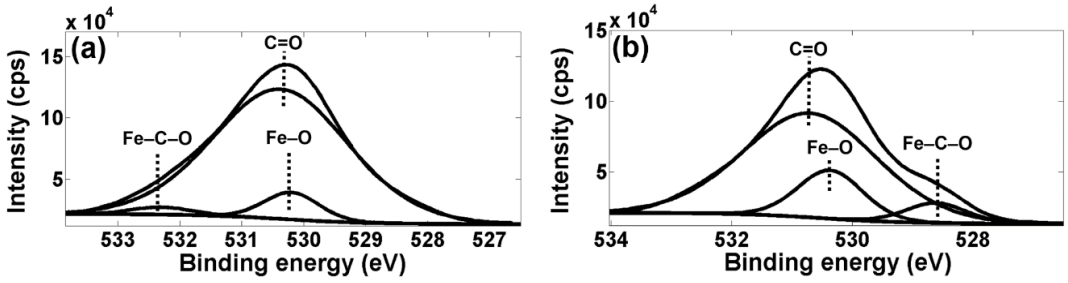

Fig 4.13: Deconvoluted O1s XPS spectra of **(a)** MIL-100(Fe) and **(b)** MIL-100-C3.

MWCNT contents is agglomeration as discussed above. Since the mean tube-to-tube distance varies inversely with the weight percentage of MWCNTs in the composites, a sufficiently higher loading might cause the tube-to-tube distance to reduce to an extent at which the Van der Waals attraction between the neighboring tubes might overcome the mutual repulsion caused by the negatively charged carboxyl groups, thus eventually leading towards agglomeration. As a consequence, the density of the tube-free regions within the structure would greatly exceed the density of the regions with agglomerated CNTs, thus lowering the net nucleation rate of MIL-100(Fe) crystals within the composite, and a subsequent reduction in the maximum water vapor uptake.

The water adsorption/desorption isotherms at 313 K for MIL-100(Fe), MIL-100-C1, MIL-100-C2 and MIL-100-C4, are shown in Figure 4.16. A maximum water vapor uptake of 36.2 wt% is observed for MIL-100(Fe), while it has been measured to be 34.6, 42.3 and 39.7 wt.% for MIL-100-C1, MIL-100-C2, and MIL-100-C4, respectively. Hence, a noticeable difference in uptake can be seen for both MIL-100(Fe) and MIL-100-C1, which becomes quite nominal for MIL-100-C2 and MIL-100-C4. It is observed that, for MIL-100(Fe), the desorption branch now lies completely below the adsorption branch for all

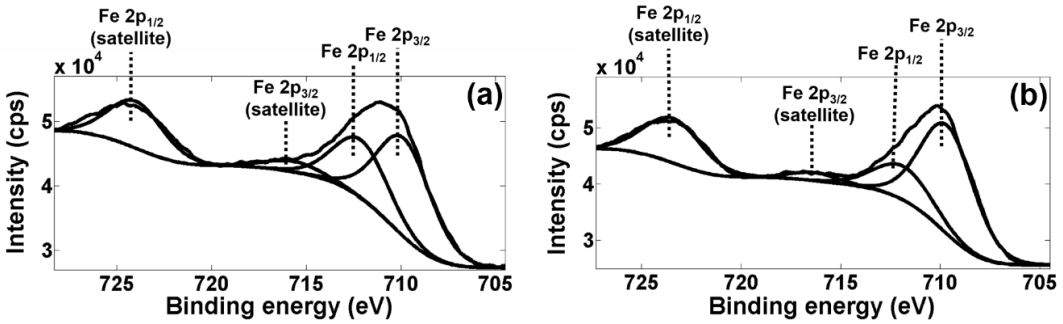

Fig 4.14: Deconvoluted Fe2p XPS spectra of **(a)** MIL-100(Fe) and **(b)** MIL-100-C3.

values of P/P_0, and the amount of hysteresis increases substantially when the temperature is raised from 298 to 313 K. For the three composites, the desorption curve can be seen to intersect the adsorption curve at critical value of P/P_0, after which it stays below the adsorption curve for the remaining values of P/P_0. This is attributable to the increased hydrophobicity of the framework due to the incorporation of MWCNTs which accelerates the desorption of water molecules when a critical value of P/P_0 is reached. From the water sorption data measured at 298 and 313 K, the heat of adsorption can be estimated. The differential isosteric heat of adsorption $Q_{st,ads,diff}$ can be expressed as [47]:

$$Q_{st,ads,diff} = -R \ln\left(\frac{p_2}{p_1}\right)\left(\frac{T_1 T_2}{T_2 - T_1}\right) \tag{4.2}$$

where p_1 and p_2 are the relative pressures corresponding to instantaneous water uptake for the isotherms measured at temperatures T_1 and T_2 respectively, and R denotes the molar gas constant.

Figure 4.17 shows the variation of $Q_{st,ads,diff}$ with instantaneous water uptake for MIL-100(Fe) and MWCNT/MIL-100(Fe) composites. It can be seen that $Q_{st,ads,diff}$ decreases with increasing uptake except for MIL-100-C1 in which it case it is observed to increase. From the individual values of $Q_{st,ads,diff}$ measured against each value of instantaneous uptake, the average isosteric enthalpy of adsorption can be expressed as [120]:

$$Q_{st,ads} = \frac{1}{q_{high} - q_{low}} \int_{q_{low}}^{q_{high}} Q_{st,ads,diff}(q)\, dq \tag{4.3}$$

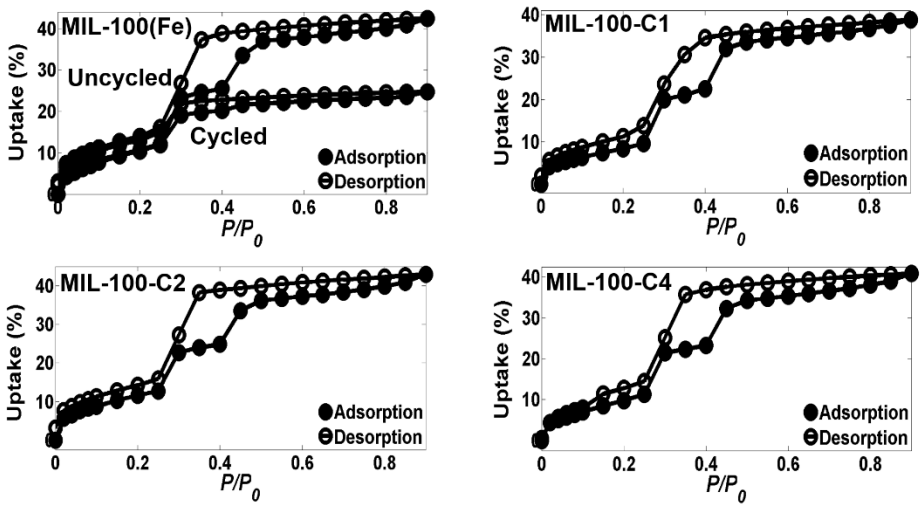

Fig 4.15: Water adsorption-desorption isotherms at 298 K for MIL-100(Fe) and MWCNT/MIL-100(Fe) composites.

where q_{low} and q_{high} denote the lower and upper limits of instantaneous water uptake respectively. The values of $Q_{st,ads}$ for each material are measured to be 51.19 kJmol^{-1} for MIL-100(Fe), 49.32 for MIL-100-C1, 55.32 for MIL-100-C2 and 40.88 for MIL-100-C4. Since heat of adsorption is a measure of the affinity of an adsorbent towards adsorbate molecules, a direct correlation can be seen to exist between $Q_{st,ads}$ and the maximum uptake except for the case of MIL-100-C2 since it alone shows the anomalous behavior of increase in $Q_{st,ads,diff}$ with increasing instantaneous uptake as shown in Figure 4.17.

The cyclic water adsorption/desorption test results based on 21 consecutive cycles for MIL-100(Fe) and three types of MWCNT/MIL-100(Fe) composites, MIL-100-C1, MIL-100-C2, and MIL-100-C4, are shown in Figure 4.18. It can be seen that there is a continual

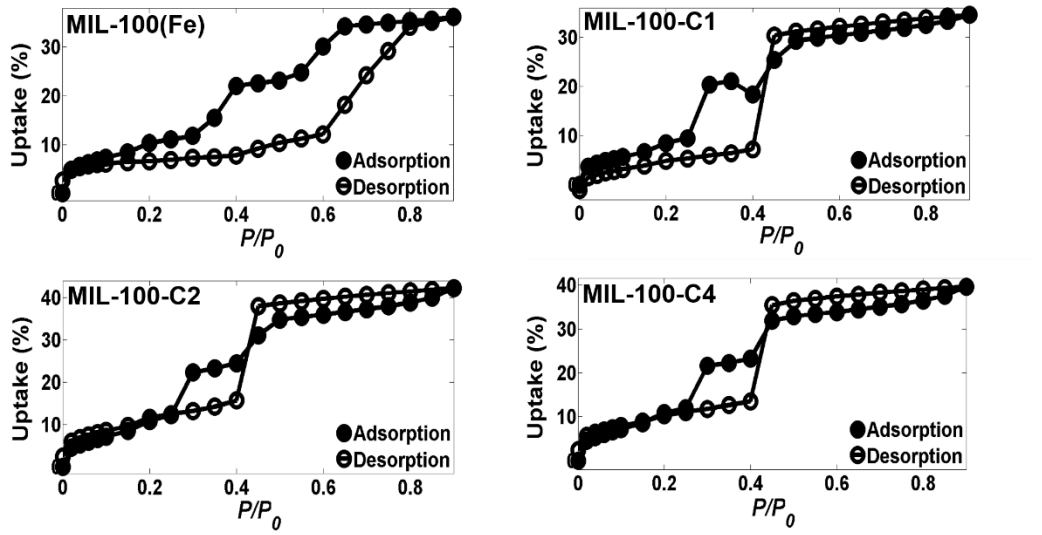

Fig 4.16: Water adsorption-desorption isotherms at 313 K for MIL-100(Fe) and MWCNT/MIL-100(Fe) composites.

decrease in the water uptake with the increasing number of cycles for each sample. For MIL-100(Fe), it was observed that there is a difference of 54.31% between the maximum water vapor uptake measured for the first and the last cycles; for MIL-100-C1, this difference was evaluated to be equal to 37.73%; for MIL-100-C2 it was calculated to be equal to 62.54%, while for MIL-100-C4 it was evaluated to be equal to 48.43%. Hence, a comparison of Figures 4.15 and 4.18 indicates that the composite exhibiting the highest maximum water vapor uptake at 298 K also results in the largest difference between the maximum uptake measured for the first and the last cycles during cyclic adsorption-desorption (MIL-100-C2), while the one exhibiting the lowest maximum water vapor uptake results in the smallest difference between the maximum uptake measured for the first and the last cycles (MIL-100-C1). Hence, for practical use as an adsorbent in an adsorption chiller application, the composite MC4 can be preferred over the other three

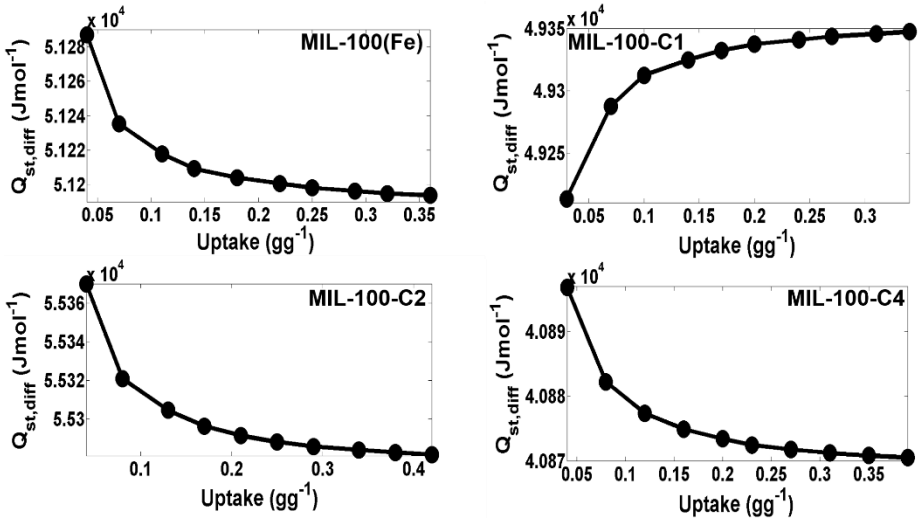

Fig 4.17: Variation of differential isosteric heat of adsorption with instantaneous water uptakes for MIL-100(Fe) and MWCNT/MIL-100(Fe) composites.

characterized materials as it exhibits only 3.8% lower maximum water uptake than MIL-100(Fe) but shows 11.5% lesser difference between the maximum water vapor uptake measured for the first and the last cycles during cyclic adsorption-desorption. Figures 4.19 and 4.20 show the SEM micrographs and the PXRD patterns of the uncycled and the cycled materials, respectively. The arrows in the SEM micrographs shown in Figure 4.19 indicate the locations of MWCNTs. It is evident that the cycled samples retain the crystallinity of their uncycled counterparts upon exposure to 21 consecutive water adsorption-desorption cycles.

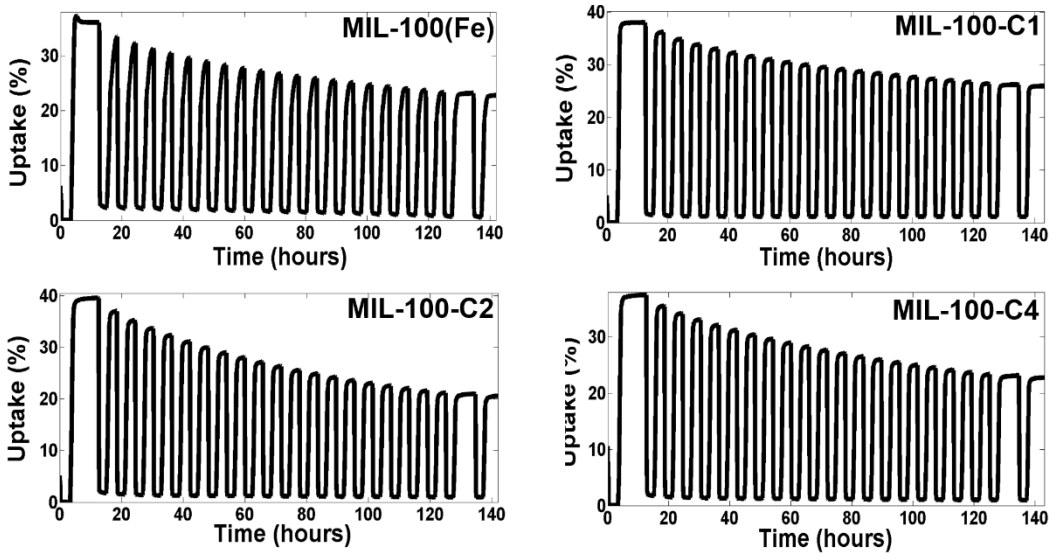

Fig 4.18: Cyclic water adsorption-desorption profiles for **(a)** MIL-100(Fe), **(b)** MIL-100-C1, **(c)** MIL-100-C2, and **(d)** MIL-100-C4.

4.3. MWCNT/MIL-101(Cr) composite

Figure 4.21 shows the SEM micrographs of as-synthesized MIL-101(Cr) and MWCNT/MIL-101(Cr) composites. The octahedral-shaped crystals characteristic of the MIL-101(Cr) lattice are evident in Figure 4.21(a). The incorporation of MWCNTs preserves the shape of the crystals as shown in Figure 4.21(b). The MWCNTs can also be seen implanted in the surrounding MIL-101(Cr) matrix, which is a consequence of the molecular-level interaction of negatively charged carboxyl groups on MWCNTs and Cr^{3+} ions in aqueous solution during the *in-situ* synthesis of the composite (Figure 3.1(b)). Moreover, the MWCNTs can be clearly seen to be decorated with the MIL-101(Cr) crystals along the portion protruding out of the surrounding matrix in Figure 4.21(b), which is in agreement with the hypothetical concept displayed in Figure 3.1(d).

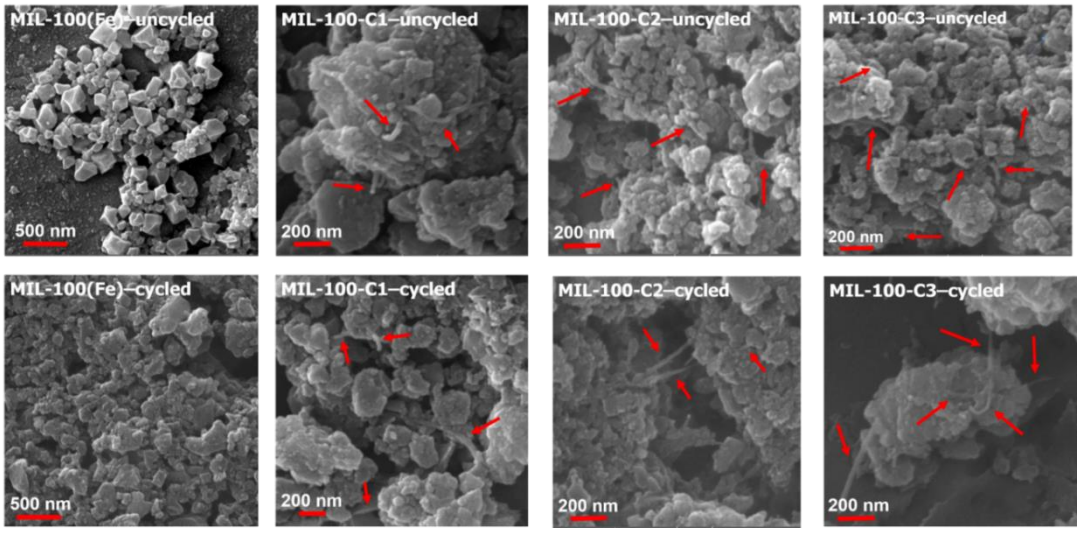

Fig 4.19: SEM micrographs of MIL-100(Fe) and MWCNT/MIL-100(Fe) composites before and after cyclic water adsorption-desorption.

Figure 4.22 shows the TEM micrographs of as-synthesized MIL-101(Cr) and the MWCNT/MIL-101(Cr) composites. Since the electron beam used in TEM transmits through the thickness of the sample, the cross-section of one of the octahedral crystals of MIL-101(Cr) shown in Figure 4.21(a) can be clearly seen in Figure 4.22(a). Moreover, TEM can also be used to reveal the micropores within the MIL-101(Cr) framework represented by the bright-colored spots uniformly distributed across the entire cross-section of the crystal. The mean dimension of these spots was found to be equal to 3.1 nm, which is in excellent agreement with the average pore diameter of the smaller and larger cages of the MIL-101(Cr) framework [165]. The inset shown in Figure 4.22(a) is the selected area diffraction pattern which clearly reveals bright spots arranged in the form concentric rings indicating the periodicity of the lattice structure of as-synthesized MIL-101(Cr) crystals. Figure 4.22(b) re-confirms the implantation of MWCNTs in the MOF matrix which can be

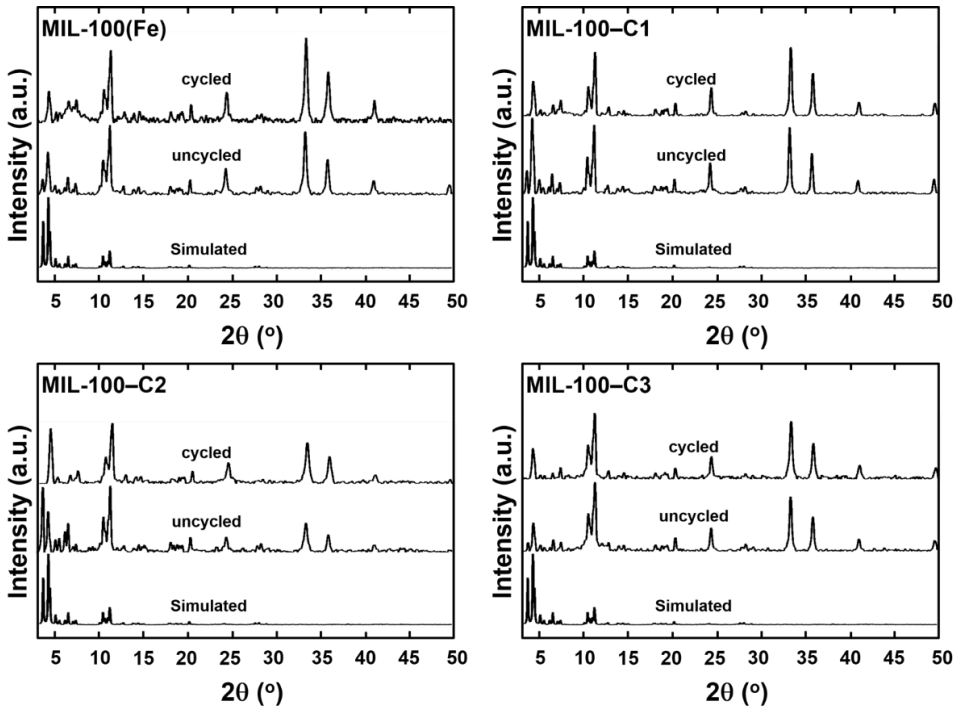

Fig 4.20: PXRD profiles of MIL-100(Fe) and MWCNT/MIL-100(Fe) composites before and after cyclic water adsorption-desorption.

clearly seen as transparent tubular structures spread across the octahedral-shaped crystallites of MIL-101(Cr).

Figure 4.23 shows the nitrogen physiosorption isotherms of MIL-101(Cr) as well as MWCNT/MIL-101(Cr) composite with 5 different weight fractions of MWCNTs. It can be clearly seen that increasing the content of carbon nanotubes in the MIL-101(Cr) matrix does not alter the adsorption kinetics since all the plots clearly reveal a type IV isotherm shape. Moreover, the incorporation of MWCNTs does not introduce any hysteresis between the adsorption and the desorption phases as characteristic of the pure MIL-101(Cr) structure. Hence, the implantation of nanotubes within the MIL-101(Cr) crystals does not

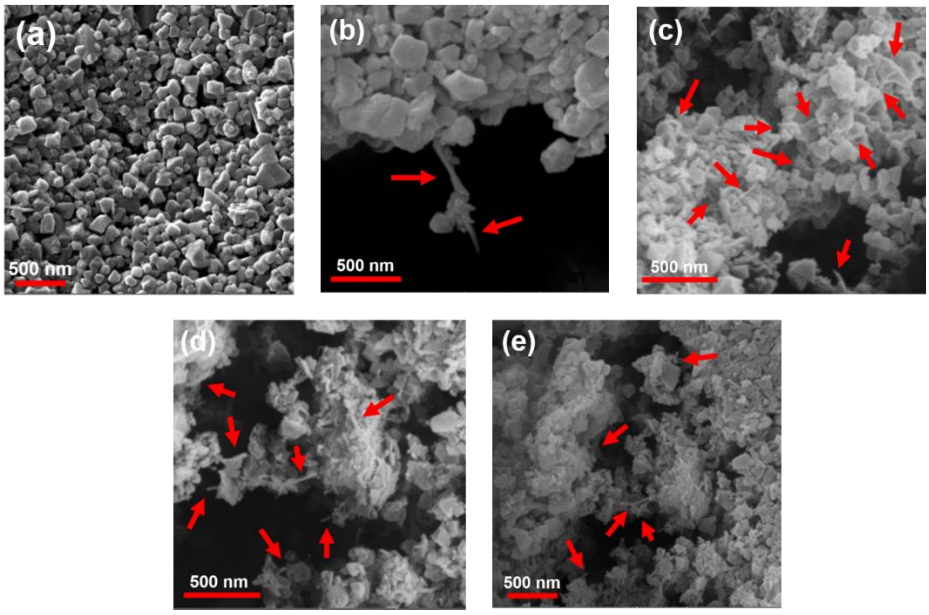

Fig 4.21: SEM micrographs of MWCNT/MIL-101(Cr) composites with various weight fractions of MWCNTs – **(a)** 0 wt% **(b)** 1.7 wt%, **(c)** 5.1 wt%, **(d)** 6.9 wt% and (e) 8.6 wt%.

result in deformation of the framework by virtue of the guest-host interactions occurring during adsorption-desorption of gas molecules. The specific surface area for MIL-101(Cr) was calculated using the best fit of the nitrogen sorption isotherm to the BET equation and was found to be equal to 3650 m^2g^{-1} which is in agreement with the already published result for MIL-101(Cr) synthesized using the same method [17]. However, at a relative pressure P/P_0 = 0.9 where MIL-101(Cr) exhibits a surface area of 2660 m^2g^{-1}, the specific surface areas for MWCNT/MIL-101(Cr) composites with different weight fractions of MWCNTs were calculated as: 3321 m^2g^{-1} (1.7 wt%), 4197 m^2g^{-1} (3.5 wt%), 3508 m^2g^{-1} (5.1 wt%), 2490 m^2g^{-1} (6.9 wt%), and 2420 m^2g^{-1} (8.6 wt%). The synthesized MWCNT/MIL-101(Cr) composites are referred to as MIL-101-C*n* with *n* from 1 to 5 corresponding to the amounts

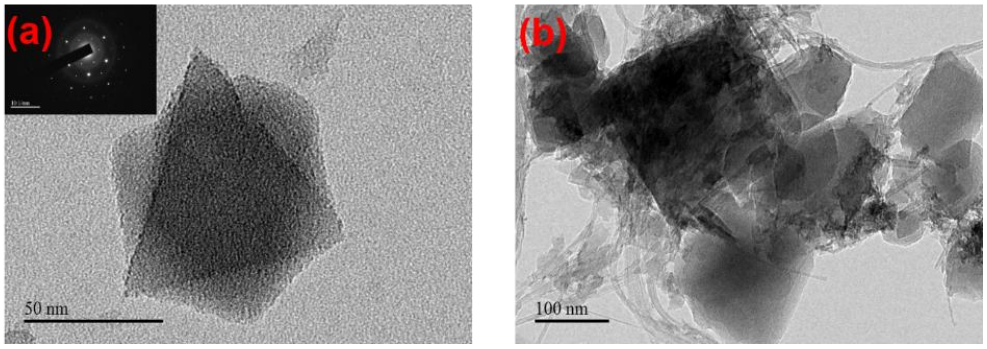

Fig 4.22: TEM micrographs of **(a)** MIL-101(Cr), and **(b)** MIL-101-C5.

of initially added MWCNTs (60 mg, 120 mg, 180 mg, 240 mg, and 360 mg, respectively).

Figure 4.24 shows the PXRD profiles of MWCNT/MIL-101(Cr) composite with various weight fractions of MWCNTs. It can be seen that the PXRD pattern of MIL-101(Cr) is in good agreement with the one reported in literature for similar method used for synthesis [61]. The incorporation of MWCNTs does not result in any noticeable peak shift or decrease in the crystallinity of the framework, as all the characteristic peaks representative of the MIL-101(Cr) structure can also be observed in the patterns shown for each category of MWCNT/MIL-101(Cr) composite. Hence, it can be concluded that the incorporation of MWCNTs up to 9 wt% using an *in-situ* synthesis method preserves the characteristic lattice structure of the MIL-101(Cr) framework. Figure 4.25 shows the TGA curves for MIL-101(Cr) and MWCNT/MIL-101(Cr) composites measured in both nitrogen and oxygen atmospheres. It can be seen that, for the curves measured in N_2 atmosphere, all the samples are stable within the range of 300–350^{o}C. The TGA curves exhibit three major weight losses spread between 30 and 600^{o}C. An initial weight loss between 30 and 100^{o}C is assigned to the removal of guest molecules trapped inside the large cages within the

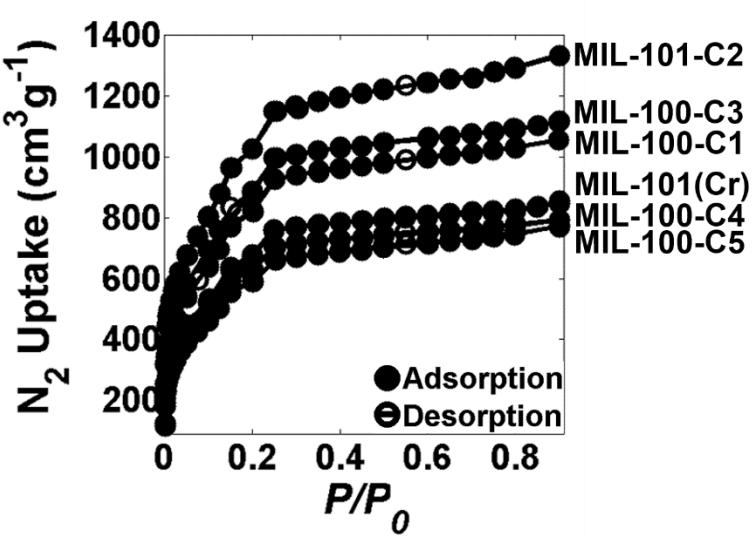

Fig 4.23: Nitrogen physiosorption isotherms of MIL-101(Cr) and MWCNT/MIL-101(Cr) composites.

framework (d = 34 Å) [38,133]. The second weight loss spread between 100 and 350^{o}C represents the removal of water molecules from the middle-sized framework cages (d = 29 Å) [166]. The final weight loss above 350^{o}C corresponds to the thermal decomposition of the benzenedicarboxylic acid linker. It can be further observed from Figure 4.25(a) that MIL-101-C1, MIL-101-C2, and MIL-101-C3 show relatively higher hydrophobicity than MIL-101(Cr) as signified by the comparatively lower weight losses observed between 30 and 100^{o}C, while both MIL-101-C4 and MIL-101-C5 depict lower hydrophobicity than MIL-101(Cr) owing to possible agglomeration of MWCNTs within the framework. Finally, it can be seen that MIL-101-C1 and MIL-101-C2 both show higher thermal stability than MIL-101, while MIL-101-C3 to MIL-101-C5 all show comparatively lower thermal stability. In contrast, the TGA conducted in the O_2 atmosphere reveals that all the composite samples show lower hydrophobicity than MIL-101(Cr) for the entire

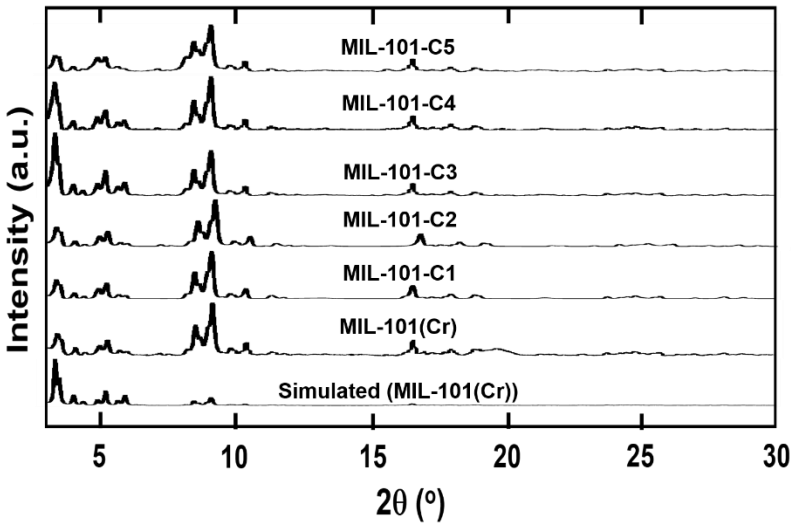

Fig 4.24: PXRD patterns for MIL-101(Cr) and MWCNT/MIL-101(Cr) composites.

temperature range between 30 and 100ºC, but also lower thermal stability than MIL-101(Cr) for the entire temperature range between 30 and 600ºC. For TGA conducted in N_2 atmosphere, the residual weights have been observed as 35.5, 37.9, 38.4, 31.9, 27.7 and 36% for MIL-101(Cr) and MIL-101-C1-C5 respectively, while for TGA conducted in O_2 atmosphere, the residual weights have been noticed to be 37.2, 31.3, 19.9, 21.8 and 30.1% for MIL-101(Cr) and MIL-101-C2-C5 respectively. Figure 4.26 shows the FTIR spectra for MIL-101(Cr) as well as MWCNT/MIL-101(Cr) composites. For MIL-101(Cr), the vibrational band observed around 1630 cm^{-1} is assigned to the surface-adsorbed water molecules [135]. The bands evidenced around 1405 cm^{-1} are attributed to the symmetric O–C–O vibrations, indicating the existence of carboxylate groups within the framework. The bands observed between 590 and 1610 cm^{-1} are assigned to phenyl groups which primarily incorporate the C=C stretching at 1510 cm^{-1}, and the C–H deformation at 1159, 1018, 885 and 751 cm^{-1}, along with a weak signal observed at 3070 cm^{-1}. The narrow and

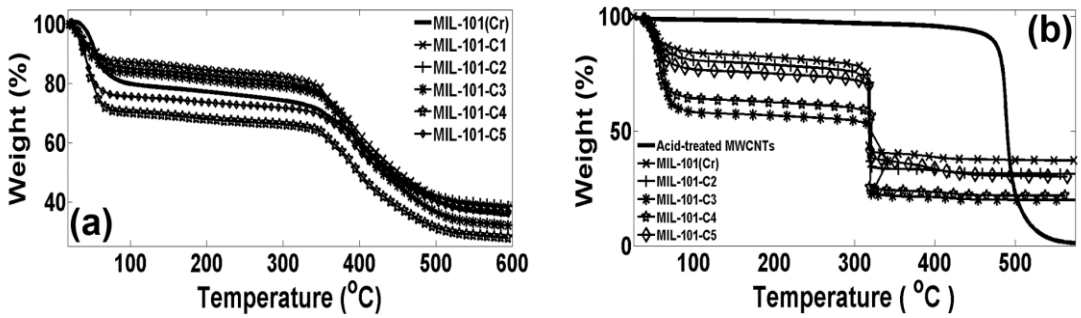

Fig 4.25: TGA curves for MIL-101(Cr) and MWCNT/MIL-101(Cr) composites in **(a)** nitrogen and **(b)** oxygen atmospheres.

weak bands observed around 749 and 1017 cm^{-1} are attributed to δ (C–H) and γ (C–H) vibrations of the aromatic rings, respectively. The weak bands present within the region of 400–700 cm^{-1} are attributed to the in-plane and the out-of-plane bending vibrations of –COO– groups [167]. A signal of medium strength around 577 cm^{-1} corresponds to Cr–O vibrations characteristic of the SBUs of the MIL-101(Cr) framework, while the peak observed in the region of 1560 – 1650 cm^{-1} is attributable to the vibration of C=O group. Finally, the broad peak observed between 2900–3700 cm^{-1} can be attributed to the water of crystallization and/or the O–H vibration of the carbonyl group. In case of MWCNT/MIL-101(Cr) composites, the peak observed at 3446 cm^{-1} is attributed to the O–H stretch within the carboxyl groups (C–OH and O=C–OH) present on the acid treated MWCNTs as shown in Figure 4.1. The weakening of the broad peak between 2900–3700 cm^{-1} observed in the spectra of MIL-101-C2 to MIL-101-C5 indicates the increased hydrophobicity of the framework with increase in the weight fraction of MWCNTs. The absence of any extraneous peaks other than those characteristic of the MIL-101(Cr) framework in the

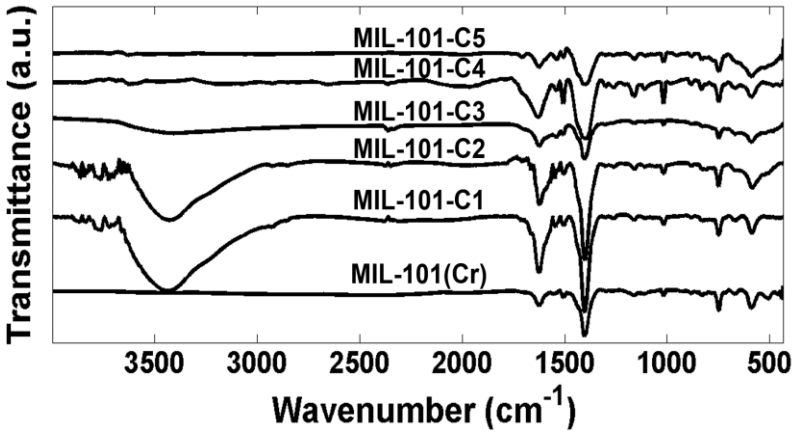

Fig 4.26: FTIR spectra for MIL-101(Cr) and MWCNT/MIL-101(Cr) composites.

FTIR spectra of the composites indicates that the incorporation of MWCNTs using the *in-situ* synthesis method does not introduce any additional functional groups which are not associated with the intrinsic chemistry of the MIL-101(Cr) framework.

The water adsorption/desorption isotherms at 298 K for MIL-101(Cr) and three types of MWCNT/MIL-101(Cr) composites, MIL-101-C3, MIL-101-C4, and MIL-101-C5, are shown in Figure 4.27. A maximum water vapor uptake of 96 wt% is observed for MIL-101(Cr), while for MWCNT/MIL-101(Cr) composites, the maximum uptakes are observed to be 127.4 wt% (MIL-101-C3), 172.3 wt% (MIL-101-C4) and 99.38 wt% (MIL-101-C5). Hence, MIL-101-C4 results in the highest water vapor uptake reported so far for a water-stable MOF. This is attributable to a much higher nucleation rate of MIL-101(Cr) on the surface of MWCNTs at a weight percentage of 6.9 wt%, resulting in a substantially larger number of crystals and significantly greater number of sites available for water adsorption [171]. However, an abrupt decline in uptake is observed when the content of MWCNTs is

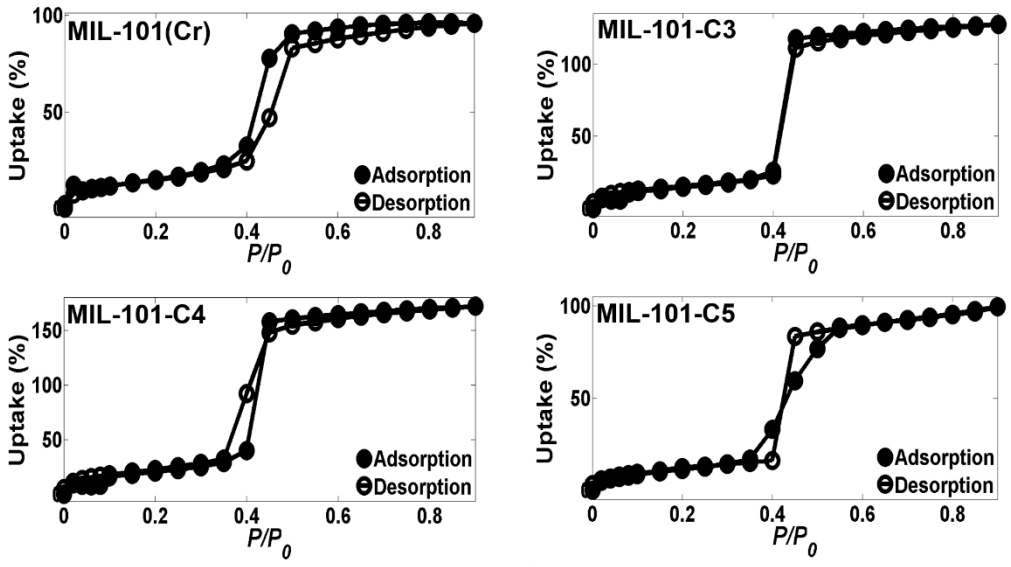

Fig 4.27: Water adsorption-desorption isotherms at 298 K for MIL-101(Cr) and MWCNT/MIL-101(Cr) composites.

increased from 6.9 to 8.6 wt% due to the possible agglomeration of MWCNTs inside MIL-101(Cr). Figure 4.28 shows the cyclic adsorption/desorption tests for 20 consecutive cycles conducted on MIL-101(Cr), MIL-101-C2, MIL-101-C3 and MIL-101-C4. It has been observed that there is a difference in uptake of approximately 17% between the first and the last cycles for MIL-101(Cr), while this difference amounts to approximately 39.6, 33.8, and 31% in case of MIL-101-C2, MIL-101-C3 and MIL-101-C4, respectively. Hence, all the MWCNT/MIL-101(Cr) composites show atleast 50% lower hydrothermal cyclic stability than MIL-101(Cr). Given the environmental toxicity associated with the use of Cr metal, the MWCNT/MIL-101(Cr) composite cannot be thus considered suitable with regards to potential usage as an adsorbent material for commercial chiller applications.

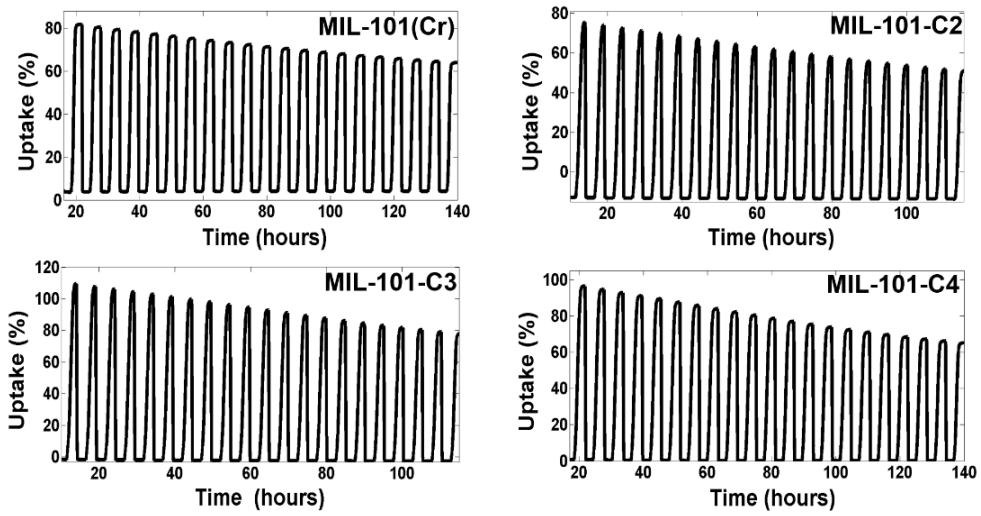

Fig 4.28: Cyclic adsorption/desorption profiles for MIL-101(Cr) and MWCNT/MIL-101(Cr) composites.

4.4. Pristine and functionalized GNPs (GO)

Figure 4.29 shows the FTIR spectra of pristine and functionalized GNPs or GO. The broad peak observed at 3430 cm^{-1} is attributable to the O–H stretching mode in carboxyl groups as well as in adsorbed water molecules. The C=O stretching in the carboxyl groups can be evidenced around 1728 cm^{-1}. The signals noticed around 627 and 1232 cm^{-1} designate the C=C and O–H bending modes in aromatic groups, and the C–O stretching mode in epoxy groups, respectively [168]. The bands evidenced around 880 and 850 cm^{-1} also confirm the asymmetric stretching and deformation modes of epoxy groups, respectively [169]. Finally, the peak observed around 1061 cm^{-1} indicates the C–O stretching modes characteristic of the alkoxy functional groups [168]. The relatively much higher intensity of the peak at 3430 cm^{-1} observable in the spectrum of GO as compared to pristine GNPs confirms the carboxylation of GNPs as a result of the functionalization process. Figure 4.30

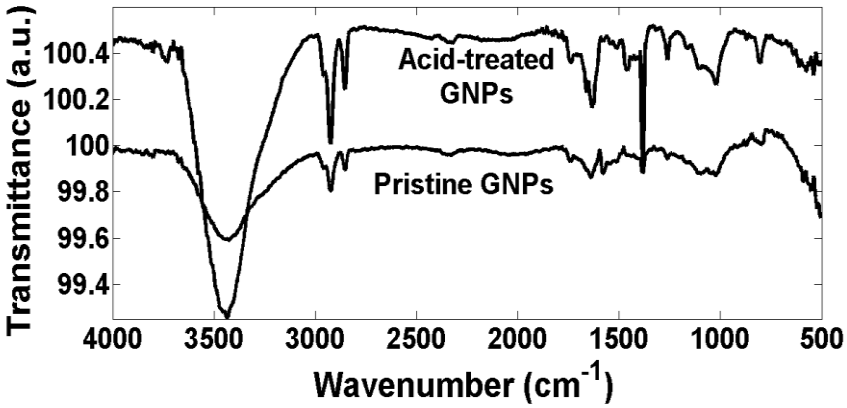

Fig 4.29: FTIR spectra of pristine GNPs and functionalized GNPs (GO).

shows the SEM micrographs of GNPs before and after the acid-treatment. It can be clearly seen that the GO sheets are more exfoliated than the pristine material. Figure 4.31 shows the PXRD patterns of both pristine and acid-treated GNPs. It can be seen that the intensity of the peak at $2\theta = 26.06^{o}$ representing the (001) planes of graphitic carbon increases substantially after the acid treatment, which is attributable to the higher interaction volume available to the incident X-rays as compared to pristine GNPs due to the exfoliation of the GO sheets. It can be further observed that the same peak is shifted slightly towards the right in the case of functionalized GNPs relative to pristine GNPs owing to the chemical attachment of functional groups as a result of the acid treatment. Finally, the peak at $2\theta = 44.46^{o}$ almost disappears in the PXRD pattern of GO due to the defect sites created on the basal planes as a result of the acid-treatment.

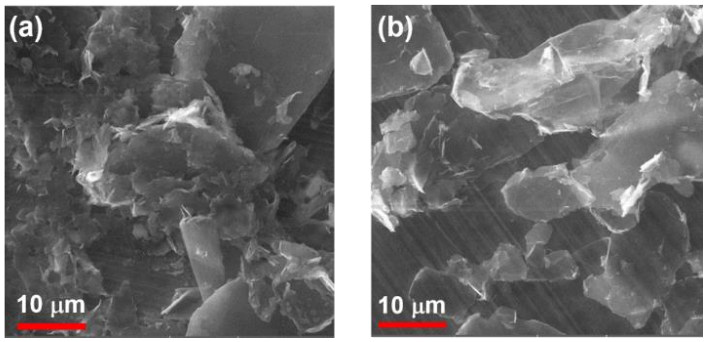

Fig 4.30: SEM micrographs of **(a)** pristine and **(b)** acid-treated GNPs (GO).

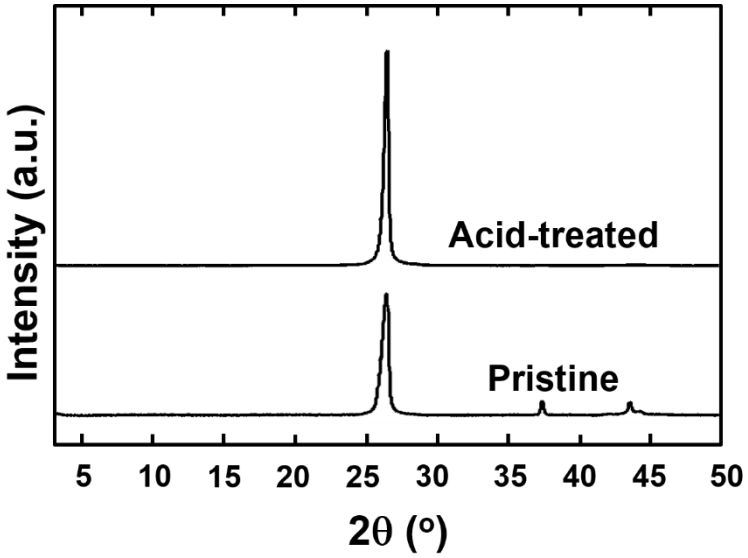

Fig 4.31: PXRD patterns of pristine and acid-treated GNPs (GO).

4.5. GO/MIL-100(Fe) composite

Figure 4.32 shows the SEM micrographs of as-synthesized MIL-100(Fe) and GO/MIL100(Fe) composites. The octahedral-shaped crystals characteristic of the MIL-100(Fe) lattice are clearly shown, while the wrapping of these crystals by the GO sheets

can be seen in the SEM images of GO/MIL100(Fe) composites, especially in case of MIL-100-G3 as schematically shown earlier in Figure 3.2(d). The protruding end of the GO sheet on the right corner of the crystal, in the inset shown in the SEM image of MIL-100-G5, confirms the nucleation and growth of the MIL-100(Fe) crystals at the functional sites on the surface of GO sheets as a consequence of the molecular-level interaction of negatively charged carboxyl groups and Fe^{3+} ions in aqueous solution during the *in-situ* synthesis of the composite [170]. It can be further noticed that the average size of the crystallites gradually decreases with increasing content of GO inside MIL-100(Fe) due to the relatively greater number of sites available for crystal nucleation and consequently a comparatively lower amount of volume available for crystal growth. As opposed to simple physical mixing of GO powder with already prepared MIL-100(Fe) powder which does not facilitate phonon transfer between the guest and host materials, the existence of a chemical linkage between the GO sheets and the MIL-100(Fe) crystals is a necessary pre-requisite to achieve an improved heat transfer rate within the MIL-100(Fe) matrix.

Figure 4.33 shows the TEM micrographs of as-synthesized MIL-100(Fe) and the GO/MIL-100(Fe) composites. The TEM micrographs of MIL-100-G3 and MIL-100-G5 show a number of MIL-100(Fe) crystals reflected across adjacent N-GO platelets (black arrows), which is a sign that these crystals are wrapped by these platelets in three dimensions (Figure 3.2(d)). The micrograph of MIL-100-G1 clearly shows a dark-colored corner of a single platelet reflected on the rear side of an isolated MIL-100(Fe) crystal which is also a confirmation of partial wrapping. The average crystallite size can also be seen to reduce gradually upon increasing GO loadings in MIL-100(Fe) as observed earlier in the SEM study. Hence, both SEM and TEM studies validate the synthesis protocol used for

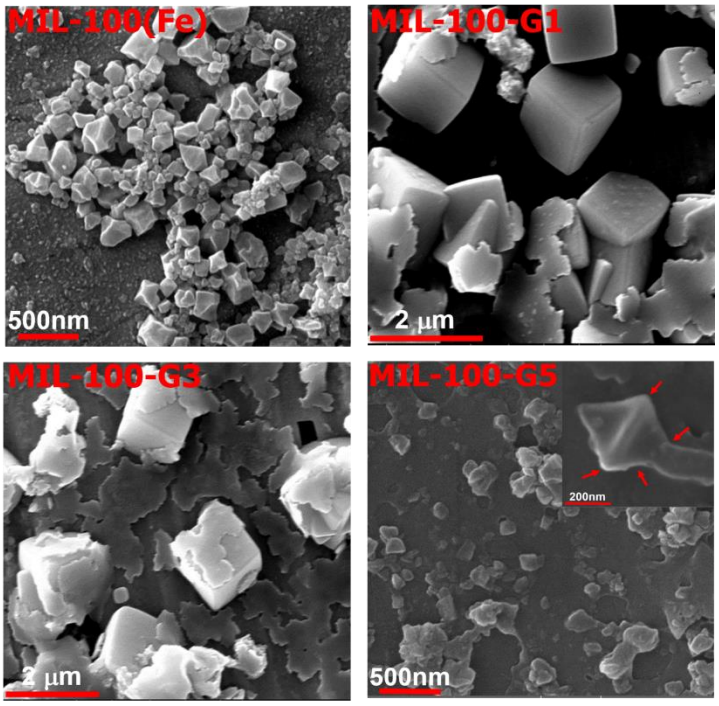

Fig 4.32: SEM micrographs of MIL-100(Fe) and GO/MIL-100(Fe) composites.

GO/MIL-100(Fe) composite involving molecular-level interaction of Fe^{+3} ions with the oppositely-charged functional groups attached on the surface of GO sheets in a common solvent.

Figure 4.34 shows the nitrogen physiosorption isotherms of MIL-100(Fe) as well as GO/MIL-100(Fe) composites. It can be clearly seen that increasing the content of GO in MIL-100(Fe) neither alters the adsorption kinetics since all the plots clearly reveal a type IV isotherm shape, nor introduces any further hysteresis between the adsorption and desorption phases relative to the intrinsic MIL-100(Fe) framework. The specific surface area for MIL-100(Fe) was calculated using the best fit of the nitrogen sorption isotherm to the BET equation and was found to be equal to 1360 m^2g^{-1} which is in agreement with the

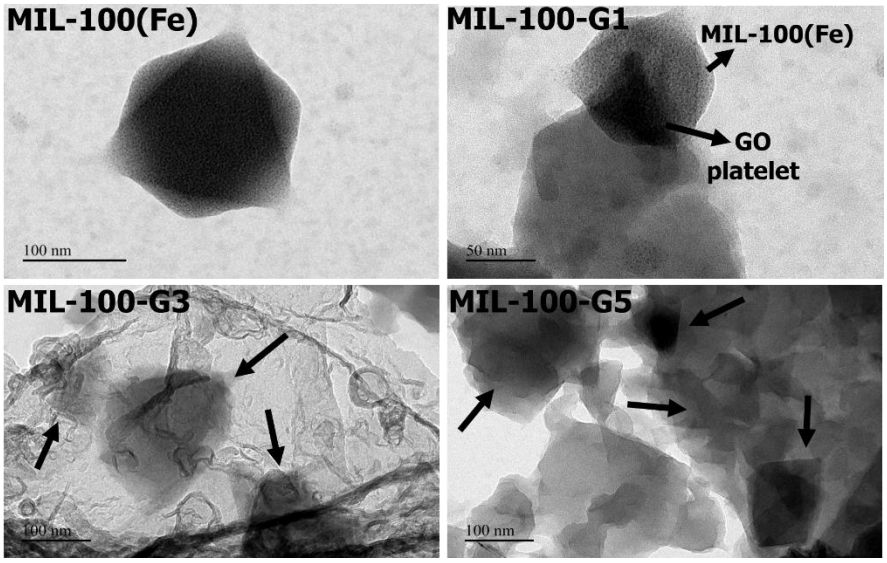

Fig 4.33: TEM micrographs of MIL-100(Fe) and GO/MIL-100(Fe) composites.

already published result for MIL-100(Fe) synthesized using the same method [136]. For the GO/MIL-100(Fe) composite, the specific surface areas in the ascending order of GO addition to MIL-100(Fe) precursors were calculated as follows: 1104 m^2g^{-1} (10.14 wt%), 819 m^2g^{-1} (13.87 wt%), 889 m^2g^{-1} (19.99 wt%), 843 m^2g^{-1} (22.43 wt%), and 1393 m^2g^{-1} (17.75 wt%) (Table 4.2). Hence, the composite with 17.75 wt% GO results in a higher BET surface area than MIL-100(Fe). The synthesized GO/MIL-100(Fe) composites are referred to as MIL-100-G*n* with *n* from 1 to 5 corresponding to the respective amounts of GO added initially to MIL-100(Fe) precursors (70 mg, 130 mg, 180 mg, 200 mg, and 300 mg respectively).

Figure 4.35 shows the PXRD profiles of activated MIL-100(Fe) as well as GO/MIL-100(Fe) composites. The incorporation of GO does not result in any noticeable peak shift or decrease in the crystallinity of the framework, as all the characteristic peaks

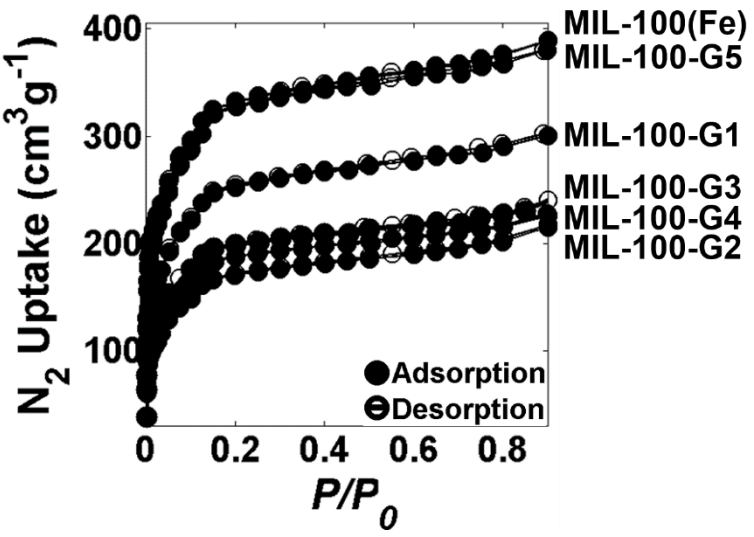

Fig 4.34: Nitrogen physiosorption isotherms of MIL-100(Fe) and GO/MIL-100(Fe) composites.

representative of the MIL-100(Fe) structure can also be observed in each of the PXRD patterns shown for GO/MIL-100(Fe) composites. However, a slight reduction in the peak intensities for $2\theta = 3–30^{o}$ can be seen in the PXRD patterns of MIL-100-G-2 to MIL-100-G-5 as a consequence of the excessive chemical coordination of the functional groups on the surface of GO with the oppositely charged metal ion centers in the MIL-100(Fe) framework. Hence, it can be concluded that the incorporation of GO up to 22 wt% using an *in-situ* synthesis method preserves the characteristic lattice structure of the MIL-100(Fe) framework, despite the presence of a chemical interface between the GO sheets and the surrounding MOF matrix. A comparison of the PXRD pattern of MIL-100-G5 in Figure 4.35 with the PXRD pattern of α-Fe_2O_3 shown in Figure 4.7 shows that the amount of α-Fe_2O_3 detected in this material is much less as compared to the other MWCNT or GO/MIL-

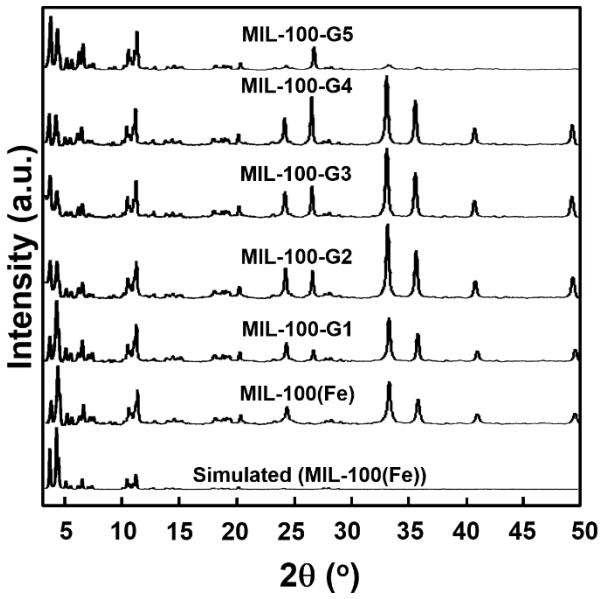

Fig 4.35: PXRD patterns for MIL-100(Fe) and GO/MIL-100(Fe) composites.

100(Fe) composites. Figure 4.36 shows the TGA results of GO, MIL-100(Fe) and GO/MIL-100(Fe) composites. For MIL-100(Fe), the TGA curve exhibits three major weight losses spread between 30 and 700^{o}C. However, for the composite materials, an additional weight loss is observed owing to the presence of GO in the framework. An initial weight loss between 30 and 60^{o}C corresponds to the removal of water molecules trapped inside the pores within the MIL-100(Fe) framework. The second weight loss spread between 60^{o}C and 297^{o}C represents the evaporation of water molecules coordinated to the Fe trimers. The abrupt weight loss of 32.23% observed between 297^{o}C and 353^{o}C in the TGA profile of MIL-100(Fe) is attributed primarily to linker decomposition within the framework [136]. Above the linker decomposition end temperature up to the final analysis temperature of 700^{o}C, the weight loss occurring in all the composite samples is assigned primarily to the oxidation of graphene inside GO with a negligibly small contribution

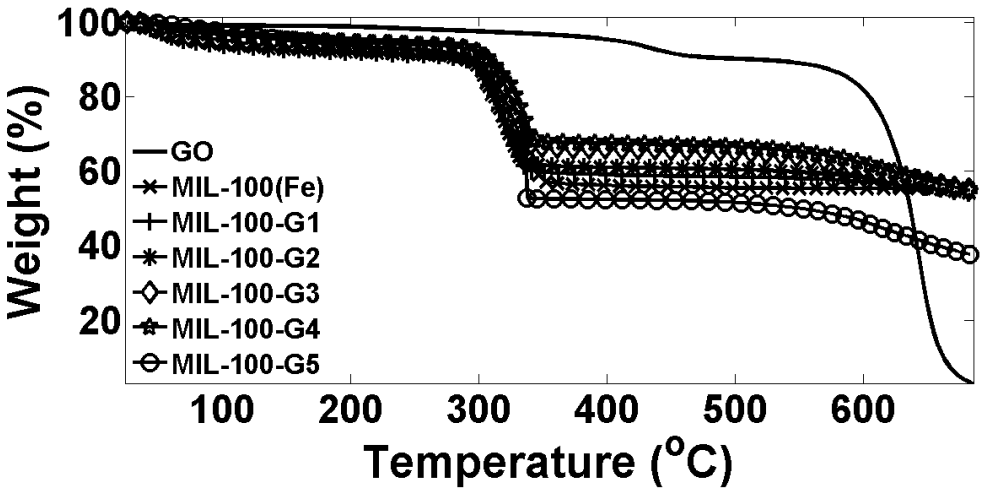

Fig 4.36: TGA curves for GO, MIL-100(Fe), and GO/MIL-100(Fe) composites.

corresponding to the decomposition of the remaining linker. From the TGA data, the amount of GO inside each composite can be evaluated. Since the amount of residual GO at the end of TGA was observed to be 2.73 wt%, the content of GO in each composite can be estimated as:

$$\textbf{GO (wt\%)} = \left\{\left[\textbf{W.L.}_{T_{GO-O_2}\rightarrow 700^{o}C}^{comp} - \textbf{W.L.}_{353^{o}C\rightarrow 700^{o}C}^{MIL-100(Fe)}\right] + 2.73\right\} + \frac{100}{M_w} \qquad (4.4)$$

where T_{GO-O_2} is the temperature at which linker decomposition ends or GO oxidation begins during TGA, $\textbf{W.L.}_{T_{GO-O_2}\rightarrow 700^{o}C}^{comp} = W_{T_{GO-O_2}}^{comp} - W_{700^{o}C}^{comp}$ stands for the weight loss between T_{GO-O_2} and 700°C expressed as a percentage of the initial weight, and the superscript "comp" denotes GO/MIL-100(Fe) composite. The weight loss for MIL-100(Fe) between 353 and 700°C was measured to be equal to 1.8148 wt%, i.e. $\textbf{W.L.}_{353^{o}C\rightarrow 700^{o}C}^{MIL-100(Fe)}$ = 1.8148%. In Equation (4.4), the term M_w stands for the weight percentage of anhydrous

MIL-100(Fe) in each sample excluding the content of iron-oxide (α-Fe_2O_3) impurity which is calculated exactly the same way as previously for the case of MWCNT/MIL-100(Fe) composites. The residual weights from TGA were observed to be 55.3, 54.6, 54, 55, 54.7 and 37.4% for MIL-100(Fe) and MIL-100-G1–5, respectively. Table 4.2 lists the detailed calculation of GO content in each composite using TGA data.

Figure 4.37 shows the FTIR spectra for MIL-100(Fe) and GO/MIL-100(Fe) composites. The vibrational bands evidenced around 1460, 1379, 765, and 717 cm^{-1} are characteristic of the MIL-100(Fe) framework [160], while a weak signal observed at 1710–1720 cm^{-1} corresponds to the residual trimesic acid residing within the pores of the structure. Finally, the peak at 3445 cm^{-1} visible in the spectra of GO-incorporated materials is assignable to the O–H stretch coming from the carboxyl groups (C–OH and O=C–OH) attached to the walls of the GO sheets as shown earlier in Figure 4.29. Figure 4.38 shows a qualitative evidence of the existence of C–O–Fe bonding between the negatively charged functional groups on GO and the positively charged Fe metal ion clusters in MIL-100(Fe) framework. The black arrow highlighting an extra peak positioned around 510 cm^{-1} in the spectrum of MIL-100-G5 indicates the C–O–Fe stretching vibration which has not been observed in the spectrum of MIL-100(Fe) [162]. This clearly indicates the existence of C–O–Fe linkage formed by virtue of the chemical interaction between the negatively charged functional groups on GO and the positively charged Fe metal ion clusters in MIL-100(Fe) framework during the synthesis of the GO/MIL-100(Fe) composites. Hence, the method of synthesis proposed in this study can be engineered to tailor the characteristics of the chemical interface formed between the GO sheets and the surrounding MOF matrix in accordance with the intended application. Moreover, it can be seen from Figure 4.37 that the

Table 4-2: Calculation of GO contents in GO/MIL-100(Fe) composites using TGA data.

Sample ID	$T_{GO\text{-}O_2}$ (ºC)	$W^{comp}_{T_{GO\text{-}O_2}}$ (%)	$W^{comp}_{700^oC}$ (%)	$W.L._{T_{GO\text{-}O_2}\rightarrow 700^oC}^{comp}$ (%)	M_W (%)	GO (wt%)
MIL-100-G1	341	60.2562	54.6326	5.6236	64.50	10.1382
MIL-100-G2	339	62.1291	54.0719	8.0572	64.69	13.8707
MIL-100-G3	343	67.0191	55.0041	12.0150	64.70	19.9857
MIL-100-G4	344	68.4627	54.6678	13.7949	65.58	22.4327
MIL-100-G5	349	52.5967	37.3552	15.2415	91.01	17.7528

incorporation of GO up to 22 wt% in MIL-100(Fe) using the proposed approach does not result in formation of any undesirable functionalities thus preserving the original chemical integrity of the framework.

The water adsorption/desorption isotherms at 298 K for MIL-100(Fe), GO and three types of GO/MIL-100(Fe) composites, MIL-100-G1, MIL-100-G3, and MIL-100-G5, are shown in Figure 4.39. A maximum water vapor uptake of 42.45 wt% is observed for MIL-100(Fe), while a water vapor uptake of 2.65 wt% has been measured for GO. For GO/MIL-100(Fe) composites, the maximum uptakes are observed to be 40.62 wt% (MIL-100-G1), 33.92 wt% (MIL-100-G3), and 53.05 wt% (MIL-100-G5). Hence, MIL-100-G5 results in almost 22% higher water vapor uptake than MIL-100(Fe) at 298 K despite the intrinsic hydrophobic nature of GO. This is attributable to a relatively higher nucleation rate of MIL-

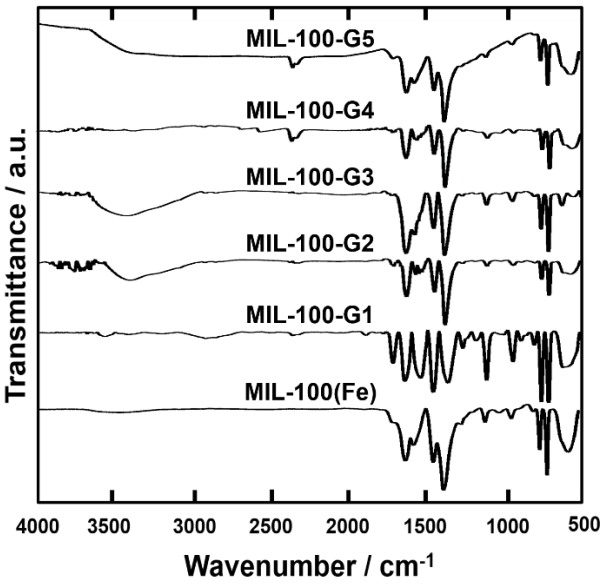

Fig 4.37: FTIR spectra for MIL-100(Fe) and GO/MIL-100(Fe) composites.

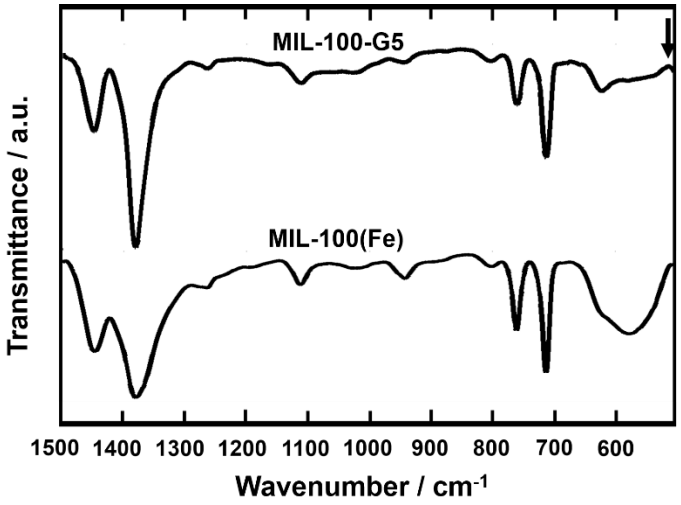

Fig 4.38: Magnified FTIR spectra of MIL-100(Fe) and MIL-100-G5 (inverted black arrow indicates C–O–Fe stretching which is absent in case of MIL-100(Fe)).

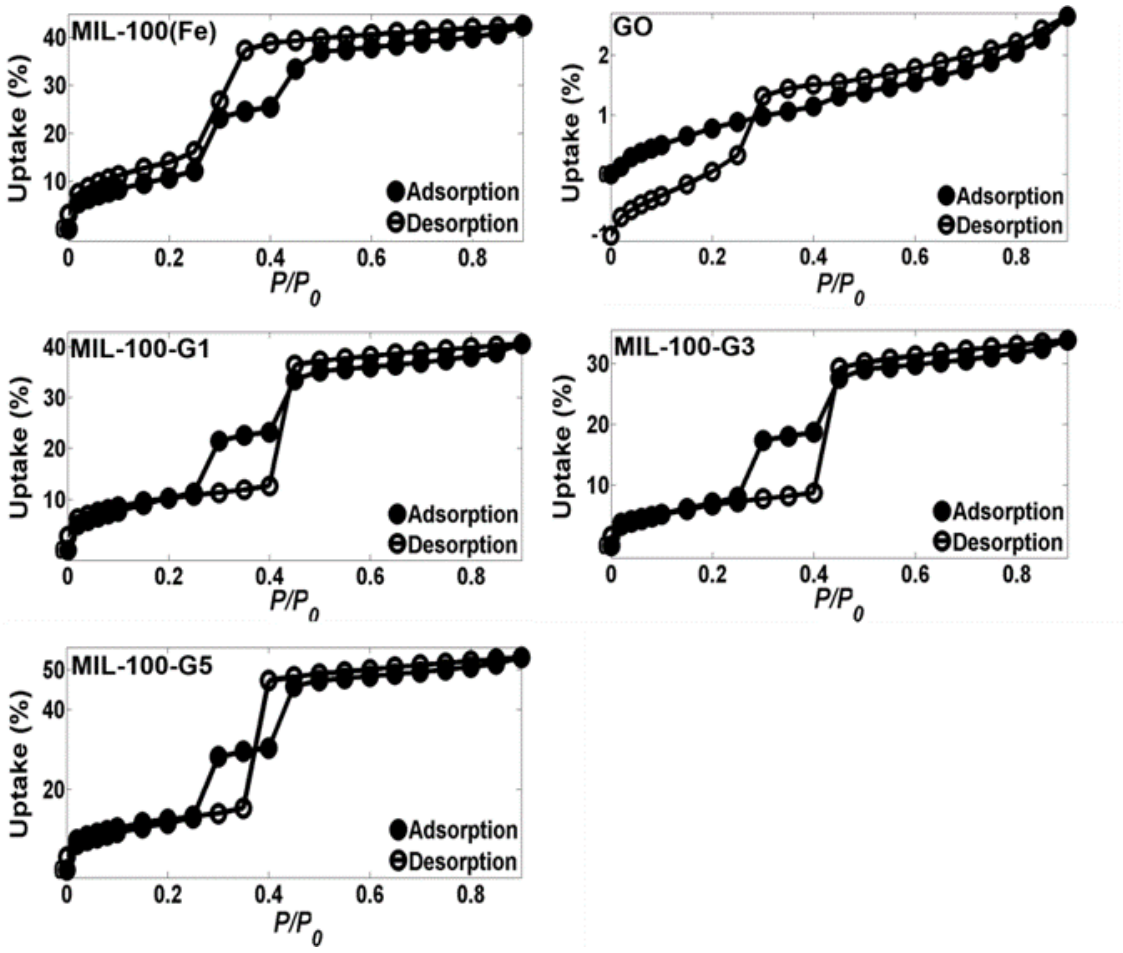

Fig 4.39: Water adsorption-desorption isotherms at 298 K for MIL-100(Fe), GO and GO/MIL-100(Fe) composites.

100(Fe) on the surface of GO at a critical weight fraction, resulting in relatively larger number of crystals, and consequently greater number of sites available for water adsorption [171]. Unlike MIL-100(Fe), the desorption curves for the three GO/MIL-100(Fe) composites have been observed to intersect the adsorption curves when a critical value of P/P_0 is reached. This is attributable to the presence of GO since the same observation also holds true for the water sorption isotherm measured for GO as shown in as shown in Figure

4.39. The cyclic water adsorption/desorption test results based on 21 consecutive cycles for MIL-100(Fe) and three types of GO/MIL-100(Fe) composites, MIL-100-G1, MIL-100-G3, and MIL-100-G5, are shown in Figure 4.40. The difference in water vapor uptake measured between the first and last cycles for each of the four materials is measured to be 48.2% for both MIL-100(Fe) and MIL-100-G3, while 27.6% and 29% for MIL-100-G1 and MIL-100-G5, respectively. Hence, it can be concluded that the GO/MIL-100(Fe) composite containing 17.75 wt% GO synthesized using the proposed approach is the most suited material for use as adsorbent in commercial-scale adsorption chillers since it has been observed to result in the best combination of water vapor uptake and architectural robustness during cyclic adsorption-desorption.

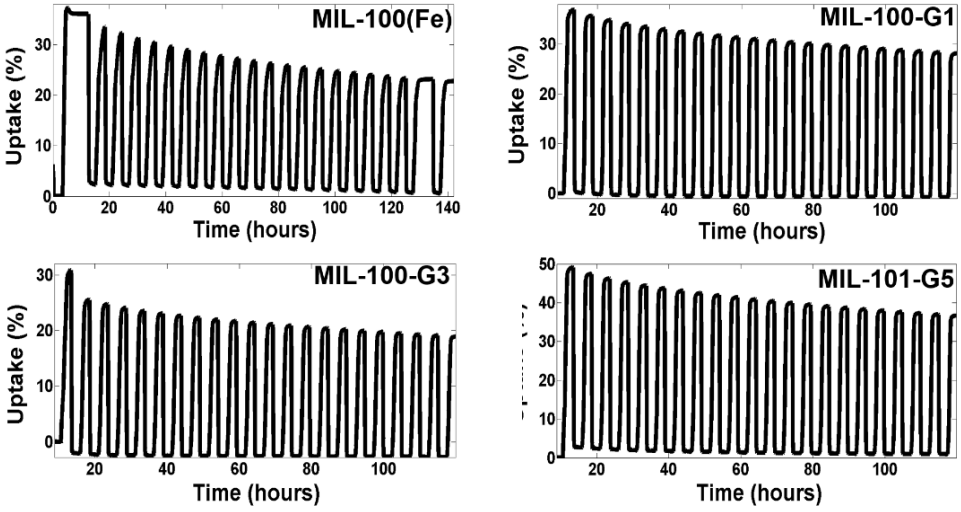

Fig 4.40: Cyclic water adsorption-desorption test results for MIL-100(Fe) and GO/MIL-100(Fe) composites.

4.6. GO/MIL-101(Cr) composite

Figure 4.41 shows the SEM micrographs of as-synthesized MIL-101(Cr) and GO/MIL-101(Cr) composite. The octahedral-shaped crystals characteristic of the MIL-101(Cr)

lattice are evident in Figure 4.41(a). The incorporation of GO preserves the shape of the crystals as shown in Figure 4.41(b). The MOF crystals can also be seen wrapped by the surrounding GO sheets (indicated by white arrows) which is a consequence of the molecular-level interaction of negatively charged carboxyl groups on GO and Cr^{3+} ions in aqueous solution during the *in-situ* synthesis of the composite. Hence, the SEM micrograph shown in Figure 4.41(b) validates the protocol proposed in this work for the synthesis of GO/MIL-101(Cr) composite. Figure 4.42 shows the TEM micrographs of as- synthesized MIL-101(Cr) and GO/MIL-101(Cr) composite. Figure 4.42(b) confirms the wrapping of the GO sheets around the MIL-101(Cr) crystals (white arrows) which reassures the presence of chemical linkages between the sheets and the crystals at the functional sites created during the acid-treatment of GNPs prior to the synthesis of the GO/MIL-101(Cr) composite.

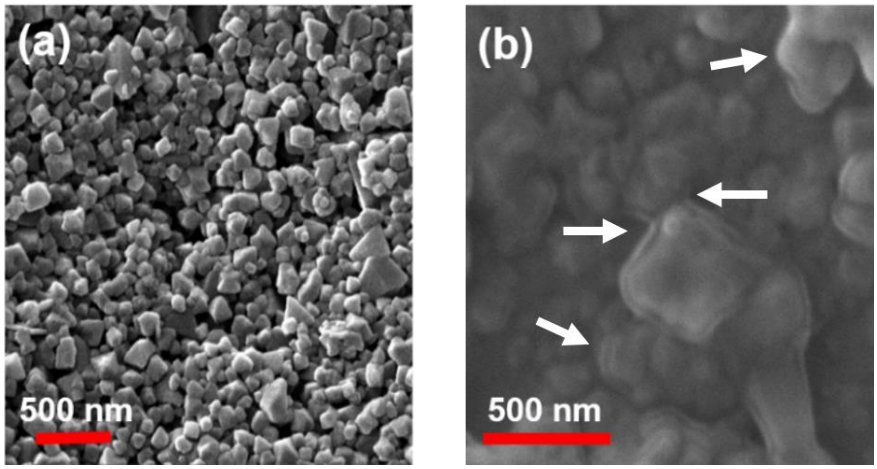

Fig 4.41: SEM micrographs of **(a)** MIL-101(Cr), and **(b)** GO/MIL-101(Cr) composite.

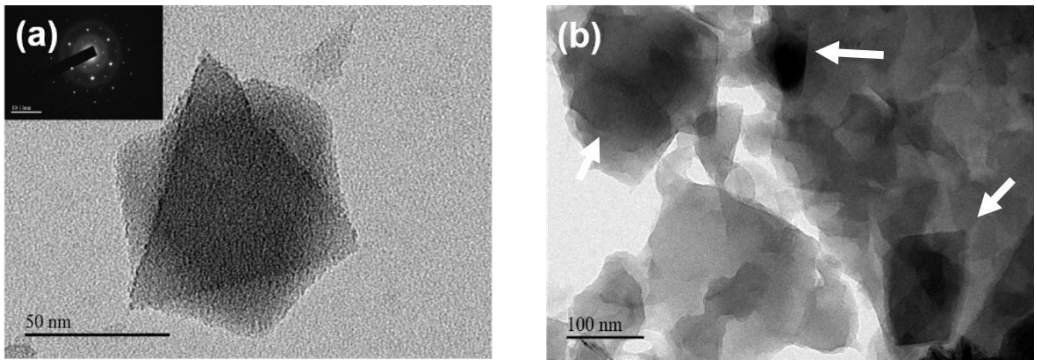

Fig 4.42: TEM micrographs of **(a)** MIL-101(Cr), and **(b)** GO/MIL-101(Cr) composite.

Figure 4.43 shows the nitrogen physiosorption isotherms of MIL-101(Cr) as well as GO/MIL-101(Cr) composite with 4 different weight fractions of GO. It can be clearly seen that increasing the content of GO in MIL-101(Cr) matrix does not alter the adsorption kinetics since all the plots clearly reveal a type IV isotherm shape. Moreover, the incorporation of GO does not introduce any hysteresis between the adsorption and the desorption phases as characteristic of the pure MIL-101(Cr) structure. At $P/P_0 = 0.95$, the specific surface area for MIL-101(Cr) evaluated using the best fit of the nitrogen sorption isotherm to the BET equation was found to be equal to 3650 m^2g^{-1}, while for the GO/MIL-101(Cr) composites, the specific surface areas for different weight fractions of GO at the same relative pressure were calculated as: 3020 m^2g^{-1} (2.7 wt%),1990 m^2g^{-1} (5.03 wt%), 2520 m^2g^{-1} (6.97 wt%), and 2210 m^2g^{-1} (11.6 wt%). The synthesized GO/MIL-101(Cr) composites are referred to as MIL-101-G*n* with *n* from 1 to 4 corresponding to the respective amounts of added GO (70 mg, 130 mg, 180 mg, and 300 mg, respectively).

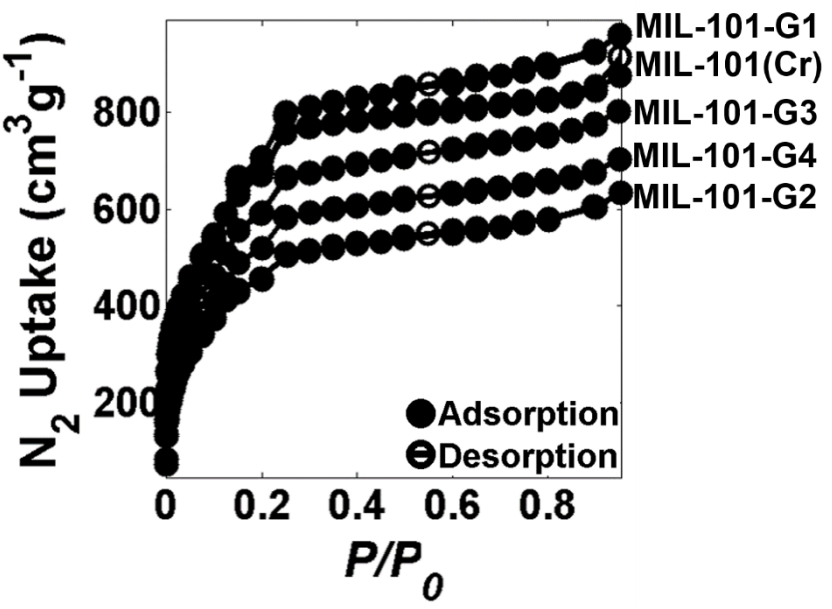

Fig 4.43: Nitrogen physiosorption isotherms of MIL-101(Cr) and GO/MIL-101(Cr) composites.

Figure 4.44 shows the PXRD profiles of GO/MIL-101(Cr) composites with various weight fractions of GO. It can be seen that the PXRD pattern of MIL-101(Cr) is in good agreement with the one reported in literature for similar method used for synthesis [61]. The incorporation of GO does not result in any noticeable peak shift or decrease in the crystallinity of the framework, as all the characteristic peaks representative of the MIL-101(Cr) structure can also be observed in the patterns shown for each category of GO/MIL-101(Cr) composite. However, an additional peak between 2θ equal to 26 and 27^{o} can be observed in the PXRD patterns of MIL-101-G3 and MIL- 101-G5, which is attributable to the (002) planes of graphitic carbon present in the GO sheets (Figure 4.30). Hence, it can be concluded that the incorporation of GO up to 12 wt% using an *in-situ* synthesis method preserves the characteristic lattice structure of the MIL-101(Cr) framework.

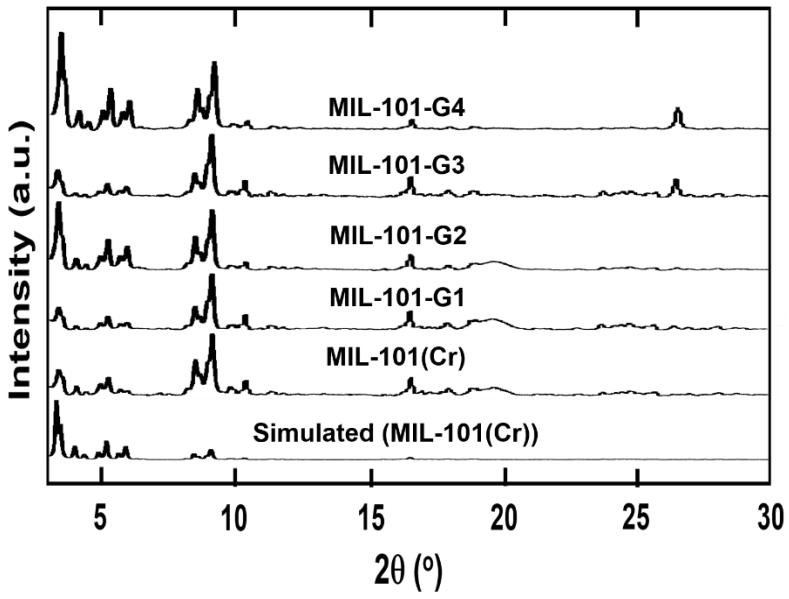

Fig 4.44: PXRD patterns for MIL-101(Cr) and GO/MIL-101(Cr) composites.

Figure 4.45 shows the TGA curves for MIL-101(Cr) and GO/MIL-101(Cr) composites. It can be seen that all the samples are stable within the range of 300–350°C. The TGA curves exhibit three major weight losses spread between 30 and 600°C. An initial weight loss between 30 and 100°C is attributed to the removal of guest water/gas molecules trapped inside the large cages within the framework (d = 34 Å) [38,133]. The second weight loss spread between 100 and 350°C represents the removal of water molecules from the middle-sized cages (d = 29 Å) [166]. The final weight loss above 350°C corresponds to the thermal decomposition of the benzenedicarboxylic acid linker. It can be clearly observed that MIL-101-G3 depicts the highest thermal stability amongst all the samples over the entire temperature range, which is most probably due to the most homogeneous dispersion of GO sheets within the MIL-101(Cr) framework. Figure 4.46 shows the FTIR spectra for MIL-101(Cr) as well as GO/MIL-101(Cr) composites. For MIL-101(Cr), the vibrational band

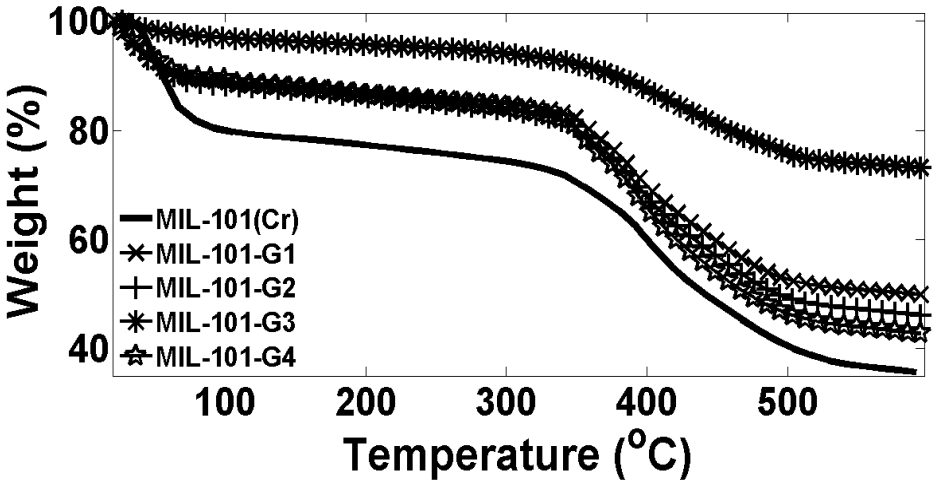

Fig 4.45: TGA curves for MIL-101(Cr) and GO/MIL-101(Cr) composites.

evidenced around 1626 cm^{-1} is attributed to the presence of adsorbed water molecules [135]. The band at 1405 cm^{-1} corresponds to the symmetric O–C–O bond vibrations, indicating the existence of carboxylate groups within the framework. The other bands observed between 590 and 1610 cm^{-1} are attributable to benzene, including the C=C stretching mode at1510, and the C–H deformation vibration at 1162, 1018, 886 and 751 cm^{-1}. A weak signal of C–H deformation can also be observed at 3070 cm^{-1}. The weak and narrow bands observed at 749 and 1017 cm^{-1} are assigned to δ (C–H) and γ (C–H) vibrations of the aromatic rings respectively. The weak bands present within the region of 400–700 cm^{-1} are attributed to the in-plane and out-of-plane bending vibrations of –COO– groups [167]. A signal of medium strength around 577 cm^{-1} corresponds to Cr–O vibrations, which is an indication of the successful synthesis of MIL-101(Cr). The peak observed in the region of 1560 – 1650 cm^{-1} is assigned to the vibration of C=O group. Finally, the broad peak spread between 2900–3700 cm^{-1} can be attributed either to the water

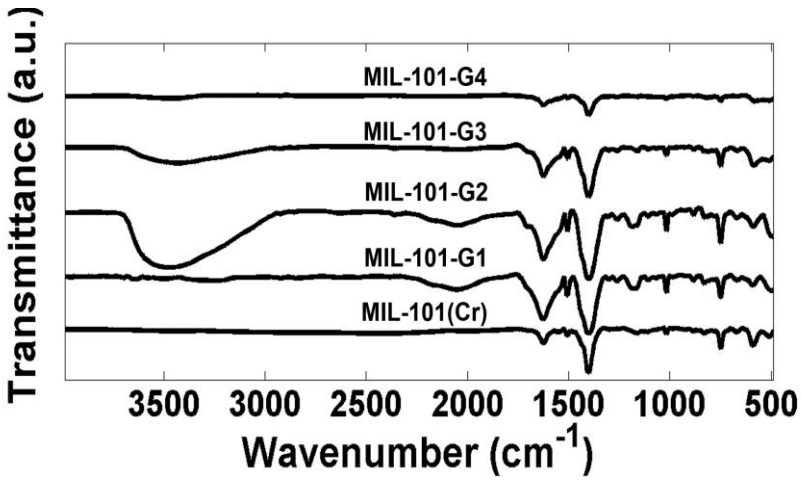

Fig 4.46: FTIR spectra for MIL-101(Cr) and GO/MIL-101(Cr) composites.

of crystallization, or to the O–H vibration of the carbonyl group. In case of GO/MIL-101 composites, the peak at 3450 cm^{-1} is assignable to the O–H stretching within the carboxyl groups (C–OH and O=C–OH) attached to the GO sheets as shown in Figure 4.29. The weakening of the broad peak observed between 2900–3700 cm^{-1} in the spectra of MIL-101-G2 to MIL-101-G4 indicates the increased hydrophobicity of the framework with the increasing content of GO. The absence of any extraneous peaks other than those characteristic of the MIL-101(Cr) framework in the FT-IR spectra of the composites indicates that the incorporation of GO up to 12 wt% using the *in-situ* synthesis method does not introduce any additional functional groups which are not associated with the intrinsic chemistry of the framework.

Figure 4.47 shows the water adsorption-desorption isotherms measured at 298 K for MIL-101(Cr) and three types of GO/MIL-101(Cr) composites, MIL-101-G1, MIL-101-G3 and MIL-101-G4. The retained uptake at the end of desorption is measured to be 1.97 wt% for MIL-101(Cr), 3.44 wt% for MIL-101-G1, 2.69 wt% for MIL-101-G3, and 0.77 wt% for

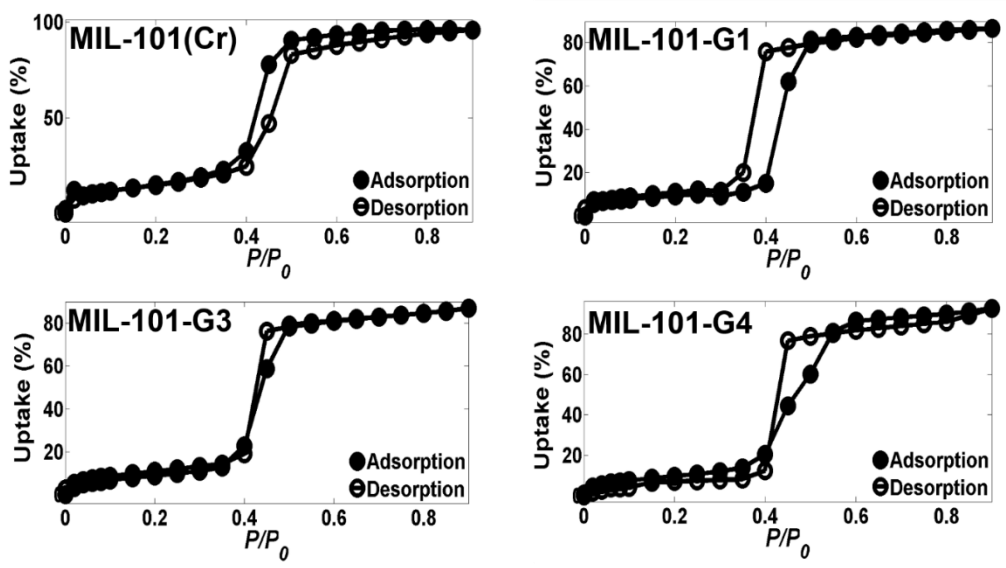

Fig 4.47: Water adsorption-desorption isotherms at 298 K for MIL-101(Cr) and GO/MIL-101(Cr) composites.

MIL-101-G4. Hence, for the three composites, the retained uptake at the end of desorption phase decreases with the increasing GO loading due to a continuous increase in the hydrophobicity of MIL-101(Cr) framework. A maximum uptake of 96 wt% has been observed for MIL-101(Cr) which drops to 86.5 wt% for MIL-101-G1, 87 wt% for MIL-101-G3, and 93 wt% for MIL-101-G4. Hence, all the three types of GO/MIL-101(Cr) composites show lower maximum uptake than MIL-101(Cr). Figure 4.48 shows the plots of hydrothermal cyclic stability for 10 consecutive cycles for MIL-101(Cr) and each of the three GO/MIL-101(Cr) composites. A difference of almost 15.4 wt% has been observed in the uptakes between the first and the eleventh cycle for MIL-101(Cr), while the corresponding values have been noticed to be 22.3 wt% for MIL-101-G1, 12.5 wt% for MIL-101-G3, and 85.5 wt% for MIL-101-G4. Hence, the GO/MIL-101(Cr) composite

showing the highest uptake shows extremely poor architectural robustness during cyclic adsorption-desorption. Given the well-known environmental toxicity affiliated with the use of Cr-containing compounds, it is therefore not recommended to use the GO/MIL-101(Cr) composite as an adsorbent in commercial-scale adsorption chillers using water as refrigerant.

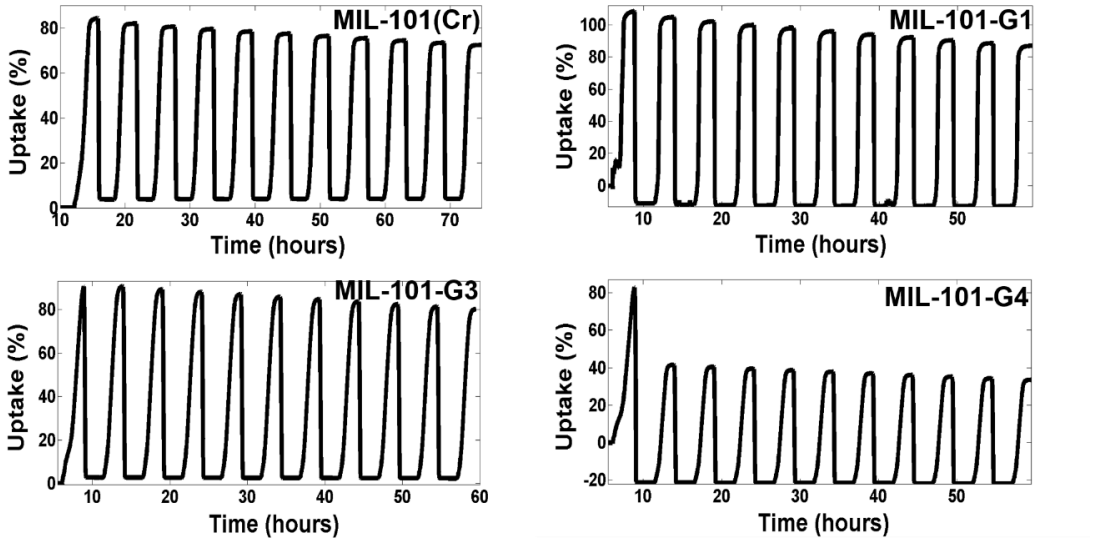

Fig 4.48: Cyclic adsorption-desorption curves for MIL-101(Cr) and GO/MIL-101(Cr) composites between 40 and 140^{o}C at 5.6 kPa.

CHAPTER 5

MODELING AND SIMULATION

5.1. Introduction

In this chapter, a numerically validated modeling approach has been adopted to evaluate the coefficient of performance (*COP*) and specific cooling power (*SCP*) for a solar-powered two-bed adsorption chiller using the MWCNT/MIL-100(Fe) composite as adsorbent and water as refrigerant. The water adsorption kinetics have been modeled using the linear driving force (LDF) correlation [172], while the Dubinin-Ashtakov model has been used to approximate the adsorption equilibrium [173]. The numerical modeling scheme assumes a zero-hysteresis water adsorption kinetics, i.e., the isosteric heats of adsorption and desorption are assumed to be of exactly the same magnitude. For solar energy input, a flat-plate solar collector has been employed which has been glazed using three different configurations – (*a*) single-glazed (S-G) cover, (*b*) double-glazed (D-G) cover, and (*c*) single-glazed cover with transparent insulation material (TIM) [175]. Numerical simulations have been conducted for each of these glaze configurations in combination with each of four different adsorbent materials – MIL-100(Fe) and MWCNT/MIL-100(Fe) composites with three different weight fractions of MWCNTs – 3.74 wt% (MIL-100-C1), 8.13 wt% (MIL-100-C2) and 13.99 wt% (MIL-100-C4). The resulting temporal variations of *COP* and *SCP* have been compared, and the most appropriate combination for use in a small-scale adsorption chiller has been proposed.

5.2. System description

A schematic of the two-bed solar adsorption chiller considered for the numerical simulation is shown in Figure 5.1. It primarily consists of four components, namely two beds (adsorber or desorber based on operational mode), evaporator and condenser. The two beds are generally equal-sized and are packed with the granulated adsorbent. A pair of control valves, V_2 and V_4, is installed between the evaporator and the adsorption/desorption beds, and another pair, V_1 and V_3, between the condenser and the beds to monitor the flow of the refrigerant. The adsorption chiller functions to generate the cooling effect *via* 4 sequential operational modes. In the first mode, V_1 and V_4 are kept closed while V_1 and V_3 are kept open. The refrigerant vaporizes at the current evaporator temperature and pressure, and is directed towards the adsorption bed where cold water circulation absorbs the heat generated during the adsorption process. At the same time, the hot water circulation around the desorption bed desorbs the already adsorbed refrigerant with the desorbed vapors directed towards the condenser *via* V_3. The refrigerant vapor are condensed again *via* cold water circulation within the condenser, while the liquid refrigerant then flows back to the evaporator which ends the first mode. In the second mode, V_1–V_4 are kept closed and the adsorption and desorption beds are pre-heated and pre-cooled *via* hot water and cold water circulation respectively, till the pressures inside the adsorption and desorption beds become roughly equal to the condenser and evaporator pressure respectively. The third mode is the reciprocal of the first one since the adsorption bed in the first one now functions as the desorption bed, and *vice versa*. As a consequence, the fourth mode is also the reciprocal of the second one, following which the first mode is re-visited. Hence, the presence of two beds functioning in parallel facilitates a continuous cooling effect as opposed to a one-bed

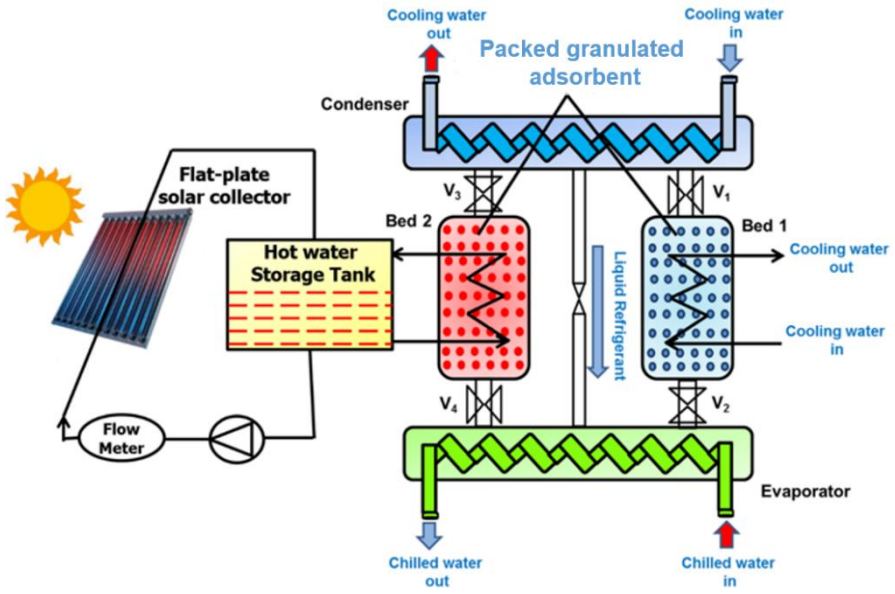

Fig 5.1: A schematic design of the two-bed solar adsorption chiller used in the study.

adsorption chiller in which a single bed can either adsorb or desorb at a time, and the cooling effect can only be generated during the desorption phase.

5.3. Adsorption equilibrium and adsorption kinetics

For each of the four types of adsorbents selected for numerical simulation, the Dubinin-Ashtakov model has been used to approximate the adsorption equilibrium given as [173]:

$$\Delta x^* = x_0 \exp\left\{-D\left[T_{ads}\ln\frac{P_{s,w}(T_r)}{P_{s,ads}(T_{ads})}\right]^n\right\} \tag{5.1}$$

where x_0, D and n are fitting parameters, while T_r has been taken to be equal to T_{evap} in the adsorption phase, and T_{con} in the desorption phase. The temperature-dependence of

saturation vapor pressure of water can be expressed as [174]:

$$P_{s,w}(T) = \exp\left(23.2308 - \frac{3841}{T-45}\right) \tag{5.2}$$

The temperature-dependence of the saturation vapor pressure for the four types of adsorbent/adsorbate pairs in its generic form can be expressed as:

$$P_{s,ads}(T) = 140 \cdot 75 \exp\left(A - \frac{B}{T-C}\right) \tag{5.3}$$

where the values of the constants *A*, *B* and *C* have been evaluated experimentally after fitting the model-predicted isotherms to experimentally measured ones for each adsorbent, and are listed in Table 5.1 along with the fitting parameters used in Equation (5.1) evaluated at 298 K [173]. Figure 5.2 presents the experimental and fitted water adsorption isotherms measured at 298 K for each of the four selected adsorbents. The water adsorption kinetics have been modeled using the linear driving force (LDF) correlation expressed as [172]:

$$\Delta x_t = \Delta x^* - \exp\left[-k_s a_v . t + \ln\left(\Delta x^* - \Delta x_t\right)\right] \tag{5.4}$$

where Δx_t represents the water vapor uptake at time *t*, and

$$k_s a_v = \frac{D_{s0}}{R_p^2} \exp\left(-\frac{E_a}{RT}\right) \tag{5.5}$$

Table 5.1 – Evaluation of empirical constants in Eq. (5.1) and Eq. (5.3) for four candidate adsorbent materials evaluated at 298 K.

Parameter	MIL-100(Fe)	MIL-100-C1	MIL-100-C2	MIL-100-C4
D	1.8×10^{-5}	1.7×10^{-5}	1.7×10^{-5}	1.7×10^{-5}
x_0	0.4281	0.3913	0.4336	0.4127
n	1.775	1.81	1.78	1.8
A	18.25	18.25	18.144	18.168
B	3830.7	3830.8	3841	3840.95
C	46.969	46.95	44.8	44.889

5.4. Energy and mass balance

5.4.1. Solar collector energy balance

The intensity of solar radiation incident on the flat-plate solar collector has been assumed to vary from sunrise to sunset in a sinusoidal manner in accordance with the relation [175]:

$$I(t) = I_{\max} \sin\left[\frac{\pi(t - t_{sr})}{t_{ss} - t_{sr}}\right],\ t_{sr} \le t \le t_{ss} \tag{5.6}$$

where $I_{\max}$ is the maximum radiation intensity occurring at noon, while t_{sr} and t_{ss} designate the times at sunrise and sunset, respectively. The temperature of hot water flowing from the hot water tank to the flat plate collector varies in accordance with the solar radiation intensity during the course of the day. Hence, without loss of generality, we

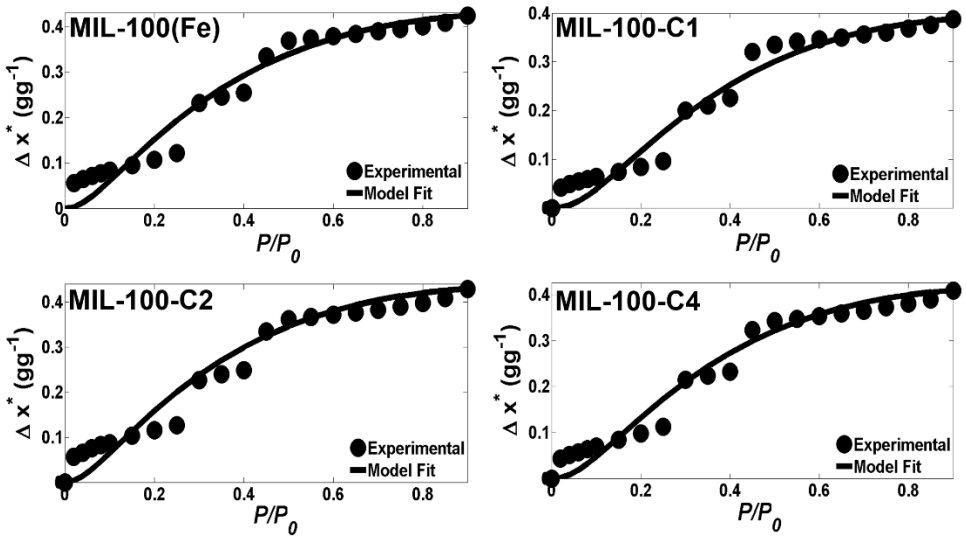

Fig 5.2: Experimental and fitted water adsorption isotherms measured at 298 K for MIL-100(Fe) and MWCNT/MIL-100(Fe) composites.

can assume that the time scale of the temporal derivative of the flat plate collector inlet temperature is the cycle time of the adsorption chiller with the following energy balance [175]:

$$A_{sc}\alpha\tau I = \Omega\frac{dT^{b}_{hw,i}}{dt_{cycle}} + U_{L}A_{sc}\left(T^{b}_{hw,i} - T_{amb}\right) + \dot{m}^{sc}_{hw}C^{w}_{p}\left(T^{b}_{hw,i} - \overline{T^{b}_{hw,o}}\right) \tag{5.7}$$

where α represents the thermal absorption coefficient of the glaze used on the solar collector, and $\overline{T^{b}_{hw,o}}$ can be expressed as:

$$\overline{T^{b}_{hw,o}} = \frac{1}{t_{cycle}}\oint_{t_{cycle}} T^{b}_{hw,o}\,dt \tag{5.8}$$

where $T^{b}_{hw,o}$ is given as:

$$T_{hw,o}^{b} = T_{b}^{d} + \left(T_{hw,i}^{b} - T_{b}^{d}\right)\exp\left(-\frac{U_{b}^{d} A_{b}}{\dot{m}_{hw}^{b} C_{p}^{hw}}\right) \tag{5.9}$$

5.4.2. Adsorption chiller energy balance

Performing energy balance on the adsorption bed yields

$$\begin{aligned} &m_{ads} C_{p}^{ads}\left(T_{b}^{a}\right)\frac{d\,T_{b}^{a}}{dt} + m_{ads} C_{p}^{w}\left[\Delta x_{a}\,\frac{d\,T_{b}^{a}}{dt} + T_{b}^{a}\,\frac{d\,\Delta x_{a}}{dt}\right] + \left(m_{Al} C_{p}^{Al} + m_{Cu} C_{p}^{Cu}\right)\frac{d\,T_{b}^{a}}{dt} - \\ &\dot{m}_{cw}^{b} C_{p}^{cw}\left[T_{cw,i}^{b} - T_{b}^{a} - \left(T_{cw,i}^{b} - T_{b}^{a}\right)\exp\left(-\frac{U_{b}^{a} A_{b}}{\dot{m}_{cw}^{b} C_{p}^{cw}}\right)\right] + \frac{d\,\Delta x_{a}}{dt}\left[m_{ads} C_{p}^{g}\left(T_{b}^{a} - T_{evap}\right) - m_{ads}\Delta H_{a}\left(\Delta x_{a}\right)\right] = 0 \end{aligned} \tag{5.10}$$

Performing energy balance on the desorption bed gives

$$\begin{aligned} &m_{ads} C_{p}^{ads}\left(T_{b}^{d}\right)\frac{d\,T_{b}^{d}}{dt} + m_{ads} C_{p}^{w}\left[\Delta x_{d}\,\frac{d\,T_{b}^{d}}{dt} + T_{b}^{d}\,\frac{d\,\Delta x_{d}}{dt}\right] + \left(m_{Al} C_{p}^{Al} + m_{Cu} C_{p}^{Cu}\right)\frac{d\,T_{b}^{d}}{dt} - \\ &\dot{m}_{hw}^{b} C_{p}^{hw}\left(T_{hw,i}^{b} - T_{hw,o}^{b}\right) - m_{ads}\Delta H_{a}\left(\Delta x_{d}\right)\frac{d\,\Delta x_{d}}{dt} = 0 \end{aligned} \tag{5.11}$$

The evaporator energy balance can be expressed as:

$$\begin{aligned} &\left(m_{evap}^{w} C_{p}^{w} + m_{evap}^{ex} C_{p}^{ex}\right)\frac{d\,T_{evap}}{dt} + \Delta L_{w} m_{ads}\,\frac{d\,\Delta x_{a}}{dt} + m_{ads} C_{p}^{w}\left(T_{con} - T_{evap}\right)\frac{d\,\Delta x_{d}}{dt} - \\ &\dot{m}_{ch}^{evap}\; C_{p}^{ch}\left[T_{ch,i}^{evap} - T_{evap} - \left(T_{ch,i}^{evap} - T_{evap}\right)\exp\left(-\frac{U_{evap}^{ex} A_{evap}^{ex}}{\dot{m}_{ch}^{evap}\; C_{p}^{ch}}\right)\right] = 0 \end{aligned} \tag{5.12}$$

The energy balance for the condenser can be expressed as:

$$\begin{aligned} &\left(m_{con}^{w} C_{p}^{w} + m_{con}^{ex} C_{p}^{ex}\right)\frac{d\,T_{con}}{dt} - \left[-\Delta L_{w} - C_{p}^{g}\left(T_{b}^{d} - T_{con}\right)\right] m_{ads}\,\frac{d\,\Delta x_{d}}{dt} - \\ &\dot{m}_{cw}^{con}\; C_{p}^{cw}\left[T_{cw,i}^{con} - T_{con} - \left(T_{cw,i}^{con} - T_{con}\right)\exp\left(-\frac{U_{con}^{ex} A_{con}^{ex}}{\dot{m}_{cw}^{con}\; C_{p}^{cw}}\right)\right] = 0 \end{aligned} \tag{5.13}$$

The rate of adsorption/desorption of the refrigerant for the relevant bed can be expressed as:

$$\frac{d\Delta x_{a/d}}{dt} - K_{a/d}\left\{\Delta x^{*}_{a/d} - \Delta x_{a/d}\right\} = 0 \tag{5.14}$$

where $K_{a/d} = \frac{F.D_{s0}}{R_p^2}\exp\left(-\frac{E_a}{RT_b^{a/d}}\right)$ represents the adsorption/desorption rate coefficient while *F* represents the particle shape factor of the adsorbent particles.

The mass balance equation can be expressed as:

$$\frac{dm^{w}_{evap}}{dt} + m_{ads}\left(\frac{d\Delta x_a}{dt} + \frac{d\Delta x_d}{dt}\right) = 0 \tag{5.15}$$

The *COP* and *SCP* for the adsorption chiller are defined as:

$$COP = \frac{\dot{m}^{evap}_{ch}\ C^{ch}_p \oint_{t_{cycle}}\left(T^{evap}_{ch,i} - T^{evap}_{ch,o}\right)dt}{\dot{m}^{b}_{hw}\, C^{hw}_p \oint_{t_{cycle}}\left(T^{b}_{hw,i} - T^{b}_{hw,o}\right)dt} \tag{5.16}$$

$$SCP = \frac{\dot{m}^{evap}_{ch}\ C^{ch}_p \oint_{t_{cycle}}\left(T^{evap}_{ch,i} - T^{evap}_{ch,o}\right)dt}{t_{cycle}\ m_{ads}} \tag{5.17}$$

where

$$T^{evap}_{ch,o} = T_{evap} + \left(T^{evap}_{ch,i} - T_{evap}\right)\exp\left(-\frac{U^{ex}_{evap}A^{ex}_{evap}}{\dot{m}^{evap}_{ch}\ C^{ch}_p}\right) \tag{5.18}$$

and

$$T^{b}_{hw,o} = T^{d}_{b} + \left(T^{b}_{hw,i} - T^{d}_{b}\right)\exp\left(-\frac{U^{d}_{b}A_b}{\dot{m}^{bed}_{hw}\ C^{hw}_p}\right) \tag{5.19}$$

More specifically, in a solar-powered refrigeration system, the solar *COP* is expressed as [175]:

$$COP_{\mathrm{sc}} = \frac{\dot{m}_{ch}^{evap} \; C_p^{ch} \oint_{t_{cycle}} \left(T_{ch,i}^{evap} - T_{ch,o}^{evap}\right) dt}{A_c \alpha \tau \, I \, t_{cycle}} \tag{5.20}$$

In a normal operation of an adsorption chiller, the *SCP* and *COP* are observed to fluctuate in given adsorption cooling cycle. In order to evaluate a cycle-averaged performance of the adsorption chiller for a more generic prediction, the mean values of *SCP* and $\overline{COP}_{\mathrm{sc}}$ have been defined as [175]:

$$\overline{COP_{\mathrm{sc}}} = \frac{1}{t_{cycle}} \oint_{t_{cycle}} COP_{\mathrm{sc}} \, dt \tag{5.21}$$

$$\overline{SCP} = \frac{1}{t_{cycle}} \oint_{t_{cycle}} SCP \, dt \tag{5.22}$$

The dependence of heat of adsorption for each adsorbent material on water vapor uptake has been experimentally determined as:

$$\Delta H_{a,\mathrm{MIL-100(Fe)}}\left(\Delta x_{a/d}\right) = \left(-1.15\times10^{4}\right)\Delta x_{a/d} + 2.7607\times10^{6} \tag{5.23}$$

$$\Delta H_{a,\mathrm{MC1}}\left(\Delta x_{a/d}\right) = \left(1.75\times10^{4}\right)\Delta x_{a/d} + 2.653\times10^{6} \tag{5.24}$$

$$\Delta H_{a,\mathrm{MC2}}\left(\Delta x_{a/d}\right) = \left(-9.3\times10^{3}\right)\Delta x_{a/d} + 2.9807\times10^{6} \tag{5.25}$$

$$\Delta H_{a,\mathrm{MC3}}\left(\Delta x_{a/d}\right) = \left(-3.1\times10^{3}\right)\Delta x_{a/d} + 2.2023\times10^{6} \tag{5.26}$$

The values of the basic input parameters and the standard working conditions used for the adsorption chiller, as well as the initial conditions used for the simulations, are listed in Table 5.2, while the values of material-specific properties for each selected adsorbent are mentioned in Table 5.3.

5.5. Model validation

The system of equations (5.6)–(5.15) is solved implicitly *via* numerical integration. A combination of fourth-order Runge-Kutta, fifth-order Adams-Bashforth, and fifth-order Adams-Moulton methods using forward difference substitution in the derivatives has been utilized. A fixed time-step of 0.01 seconds is used in the computation. For the purpose of model validation, the study conducted by Tso et al. [175] has been selected in which numerical modeling of a solar-powered double-bed adsorption chiller using a silica activated carbon/$CaCl_2$ composite adsorbent has been presented. In their study, Tso et al. have employed a flat-plate solar collector with the same three different configurations of glaze which have been selected for the current study. Using the values of the physical parameters used for the adsorption chiller used by Tso et al., the performance measures for the chiller as a function of operation time have been evaluated using equations (5.16)–(5.22). Figure 5.3 shows a comparison of the results presented by Tso et al. [175] with those numerically obtained in this study for the temperature variation of hot water entering and exiting the desorption bed as a function of time. Figure 5.4 shows a comparison of *SCP* as a function of chiller operation time between the results presented by Tso et al., and those numerically computed in this study. It can be seen that both sets of plots shown in Figures 5.3 and 5.4 exhibit similar trends of variation with increasing chiller operation time. However, an exact matching of each of the two sets of plots could not be achieved since

Table 5.2 – Standard working conditions and input parameters used for the simulation.

Parameter	Value	Parameter	Value	Initial Conditions	
R	8.314	m_{ads}	14	T_b^a	298.15
C_p^w	4.18×10^3	m_{Cu}	12.67	T_b^d	298.15
C_p^{cw}	4.176×10^3	m_{Al}	5.33	T_{evap}	298.15
C_p^{hw}	4.175×10^3	m_{evap}^{ex}	12.45	T_{con}	300
C_p^g	1.89×10^3	m_{con}^{ex}	24.28	m_{evap}^w	30
ΔL_w	2.50×10^6	m_{con}^w	5	-	-
C_p^{Cu}	386.00	$T_{hw,i}^b$	353	-	-
C_p^{Al}	905.00	$T_{cw,i}^b$	303	-	-
A_b	1.45	$T_{cw,i}^{con}$	303	-	-
A_{evap}^{ex}	0.665	$T_{ch,i}^{evap}$	287	-	-
A_{con}^{ex}	0.998	$\dot{m}_{hw}^b$	0.4	-	-
U_{con}^{ex}	4070	$\dot{m}_{cw}^b$	0.4	-	-
U_{evap}^{ex}	3550	$\dot{m}_{cw}^{con}$	0.34	-	-
U_b^a	1380	$\dot{m}_{ch}^{evap}$	0.7	-	-
U_b^d	1540	$I_{\max}$	800	-	-
Ω_{sg}	4.97×10^5	α	0.93	-	-
Ω_{dg}	5.10×10^5	τ_{sg}	0.77	-	-
Ω_{TIM}	5.40×10^5	τ_{dg}	0.60	-	-
$U_{L,sg}$	4.94	τ_{TIM}	0.48	-	-
$U_{L,dg}$	2.47	t_{sr}	06:00	-	-
$U_{L,TIM}$	1.57	t_{ss}	18:00	-	-
F	15	R_p	2.5×10^{-6}	-	-

Table 5.3 – Values of material-specific properties for each selected candidate adsorbent.

Property	MIL-100(Fe)	MIL-100-C1	MIL-100-C2	MIL-100-C4
E_a	1.605×10^{5}	1.2161×10^{5}	1.8231×10^{4}	3.8554×10^{4}
D_{s0}	5.2334×10^{12}	8.9442×10^{4}	5.0777×10^{-13}	2.0478×10^{-9}

Tso et al. do not report the values they have used for the following modeling parameters in their study – (*a*) switching time between two consecutive cycles, and (*b*) initial conditions used for (*i*) adsorption bed temperature, (*ii*) desorption bed temperature, (*iii*) evaporator temperature, (*iv*) condenser temperature, and (*v*) mass of the liquid water used in the evaporator.

5.6. Performance prediction of a two-bed adsorption chiller

Since the numerical solution of system of equations (5.6)–(5.22) involves the knowledge of specific heat capacity of adsorbent material as a function of temperature, heat capacity measurements have been performed on a TA Q1000 modulated differential scanning calorimeter under nitrogen flow. The variation of specific heat capacity with temperature for each of the four selected adsorbent materials for 313.15 K $\leq T \leq$ 413.15 K can be expressed in $Jkg^{-1}K^{-1}$ as:

$$C_p^{\text{MIL}-100(\text{Fe})}(T) = 33.3T - 5825.9 \tag{5.27}$$

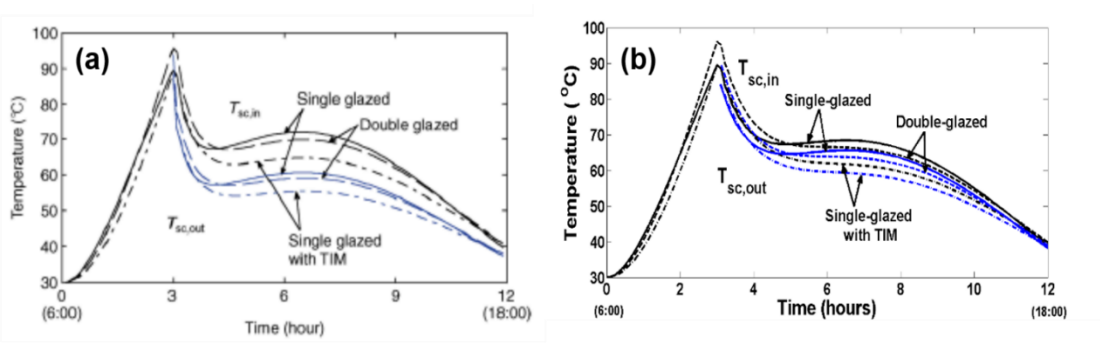

Fig 5.3: Comparison of solar collector inlet and outlet temperatures for numerical validation of proposed model – **(a)** Tso et al. [175], **(b)** current study.

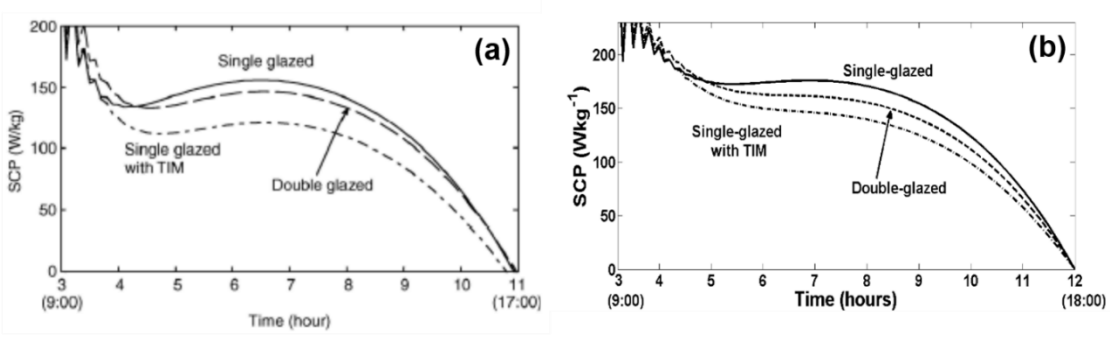

Fig 5.4: Comparison of specific cooling power of adsorption chiller for numerical validation of proposed model – **(a)** Tso et al. [175], **(b)** current study.

$$C_p^{\text{MIL-100-C1}}(T) = 17T - 1978.1 \tag{5.28}$$

$$C_p^{\text{MIL-100-C2}}(T) = 42T - 10134 \tag{5.29}$$

$$C_p^{\text{MIL-100-C4}}(T) = 22.9T - 4376.7 \tag{5.30}$$

A desorption/adsorption time ratio of 0.85, and a preheating/precooling switching time of 45 s have been used for all simulations. Figure 5.5 presents the variation of solar collector

inlet and outlet temperatures with chiller operation time for each of the four selected adsorbent materials. A solar collector area of 35 m^2 and a pre-heating period of 2.67 hours has been used to generate the figure. Furthermore, a S-G solar collector has been used for MIL-100-C1–2 and MIL-100-C4, while a D-G collector has been employed for MIL-100(Fe). It is evident that the use of an additional glaze increases the solar collector inlet temperature during the pre-heating period. However, during the course of chiller operation, it can be seen that the incorporation of MWCNTs inside MIL-100(Fe) increases both the solar collector inlet and outlet temperatures. This is attributed to the relatively higher thermal conductivity of MWCNT/MIL-100(Fe) composites as compared to MIL-100(Fe) due to the presence of MWCNTs. Hence, it can be expected that the desorption of water vapor from the adsorbent during the desorption phase can occur at relatively lower temperatures for the three MWCNT-incorporated materials as compared to MIL-100(Fe), which is expected to result in higher value of *SCP* during chiller operation.

Figure 5.6 presents the variation of evaporator temperature with chiller operation time for each of the four adsorbent materials. A solar collector area of 35 m^2, a pre-heating period of 2.67 hours, and a S-G solar collector has been employed to generate each of the four curves shown in the figure. It can be observed that both MIL-100(Fe) and MIL-100-C1 result in concave variations in T_{evap}, while both MIL-100-C2 and MIL-100-C4 are characterized by convex variations during chiller operation time. Furthermore, both MIL-100-C2 and MIL-100-C4 result in much lower minimum evaporator temperatures as compared to MIL-100(Fe) and MIL-100-C1, which shows that a threshold MWCNT content is needed for improvement in thermal conductivity of MIL-100(Fe) above which a

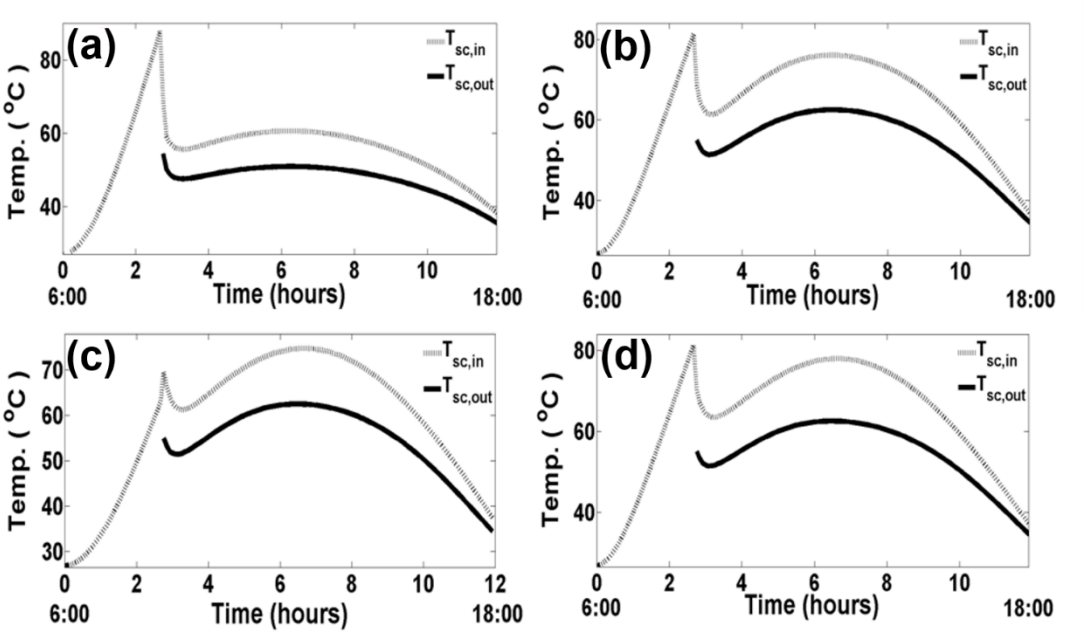

Fig 5.5: Solar collector inlet and outlet temperature variations with chiller operation time for **(a)** MIL-100(Fe), **(b)** MIL-100-C1, **(c)** MIL-100-C2 and **(d)** MIL-100-C4.

relatively lower required temperature for vapor desorption eventually results in a lower minimum evaporator temperature during the course of chiller operation.

Figure 5.7 presents the variation of adsorption and desorption rate coefficients with chiller operation time for each of the four adsorbent materials. A solar collector area of 10 m^2, a pre-heating period of 2.67 hours, and a S-G solar collector with TIM has been employed to generate each of the four sub-plots shown in the figure. As evident, the highest values of $K_{a/d}$ are exhibited by MIL-100(Fe) since MWCNTs are known to be hydrophobic and act as obstacles towards free ad-/desorption of water molecules across the pores of MIL-100(Fe) in case of MWCNT/MIL-100 composites. However, a comparison of Figures 5.7 (b–d) with Figure 5.7 (a) reveals that there is a comparatively lower difference between the

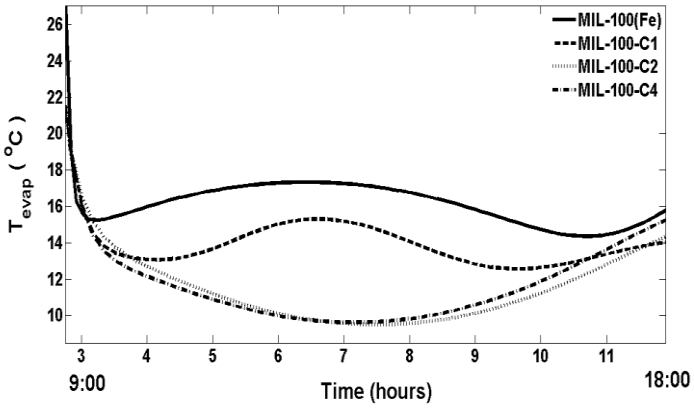

Fig 5.6: Variation of evaporator temperature with chiller operation time for each of the four selected adsorbent materials.

maximum values of K_a and K_d for MIL-100-C1–2 and MIL-100-C4 than in the case of MIL-100(Fe) which shows a relatively higher stability of performance of adsorption chiller in the context of durability during long-term service in commercial applications. Figure 5.8 presents the time-variation profiles of $\overline{SCP}$ for each solar collector configuration with an initial preheating period of 2.67 hours, and a solar collector area of 35 m^2. It is evident that $\overline{SCP}$ gradually increases as the solar radiation intensity rises with the passage of time, till it achieves its peak value within an interval between 1 p.m. and 2 p.m., and then gradually decreases till sunset. It can been further seen that all three solar collector configurations result in very similar time-variation profiles for $\overline{SCP}$, except the S-G cover with TIM which results in relatively lower peak values of $\overline{SCP}$ for each adsorbent material. Figure 5.9 presents the time-variation profiles of $\overline{COP_{sc}}$ for each solar collector configuration with an initial preheating period of 2.67 hours, and a solar collector area of 35 m^2. It can be seen

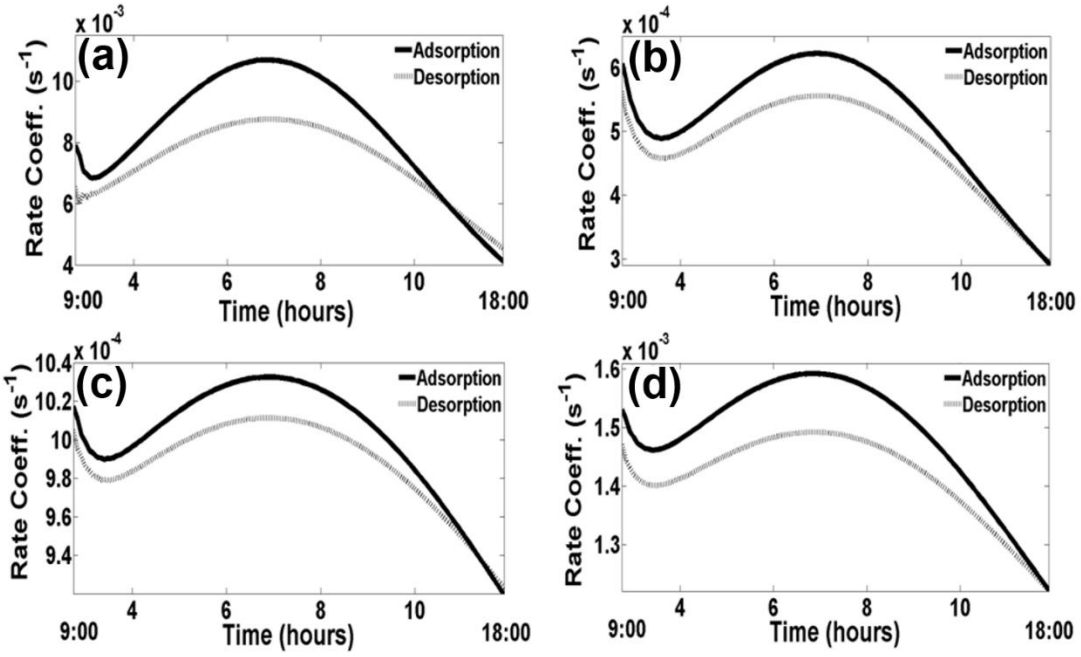

Fig 5.7: Variation of adsorption and desorption rate coefficients with chiller operation time for the four selected adsorbent materials: **(a)** MIL-100(Fe), **(b)** MIL-100-C1, **(c)** MIL-100-C2, and **(d)** MIL-100-C4.

that, unlike $\overline{SCP}$, a more or less constant value of $\overline{COP_{sc}}$ is observed for each adsorbent material from the start of chiller operation till around 5 p.m., after which a sudden decline can be noticed due to a significant decrease in the intensity of solar radiation incident upon the collector. However, the highest value of $\overline{COP_{sc}}$ is observed for the S-G cover with TIM which resulted in the lowest peak value of $\overline{SCP}$. Figure 5.10 presents the time-variation profiles of *COP* for each solar collector configuration with an initial preheating period of 2.67 hours, and a solar collector area of 35 m^2. It can be noticed that the profile variation is not as constant throughout the day as observed for the case of $\overline{COP_{sc}}$, and a minor peak

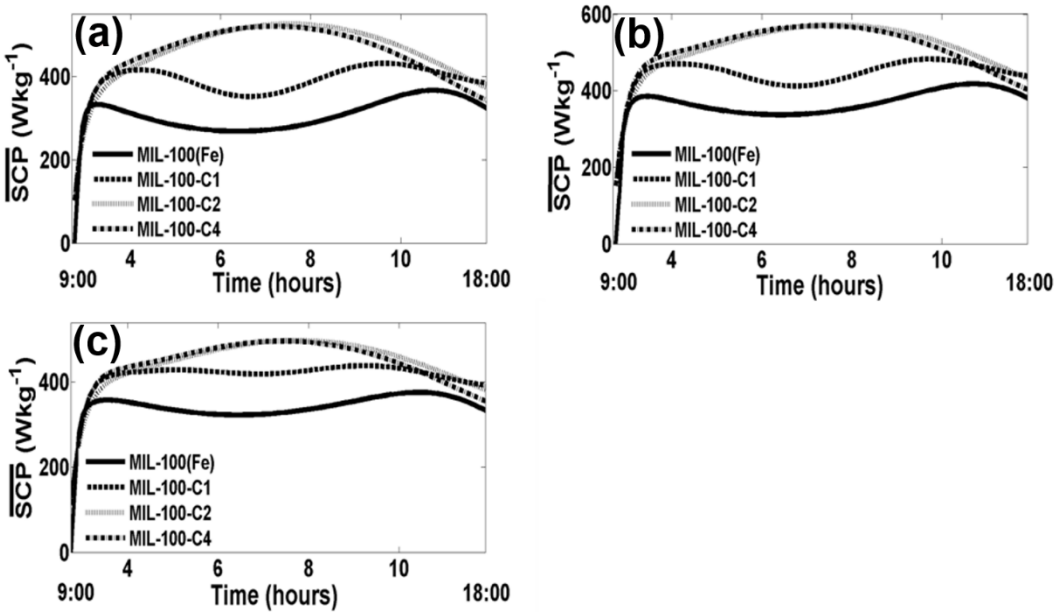

Fig 5.8: Variation of $\overline{SCP}$ as a function of chiller operation time for solar collector using **(a)** S-G cover, **(b)** D-G cover, and **(c)** S-G cover with TIM (initial preheating period of 2.67 hrs).

value can be seen within an interval of 1–2 p.m. The solar collector using S-G cover results in the highest value for *COP* for the four adsorbent materials throughout the course of chiller operation. A close examination of Figures 5.8–5.10, therefore, indicates that both *COP* and $\overline{SCP}$ are somehow correlated with respect to the performance prediction of the adsorption chiller during the course of its operation; $\overline{COP_{sc}}$, however, represents an entirely independent measure which is more sensitive to the type of collector configuration resulting in the most appropriate input of radiation intensity required for an optimum functioning of the adsorption chiller. Table 5.4 summarizes the peak values of the three performance measures observed during the course of chiller operation with an initial

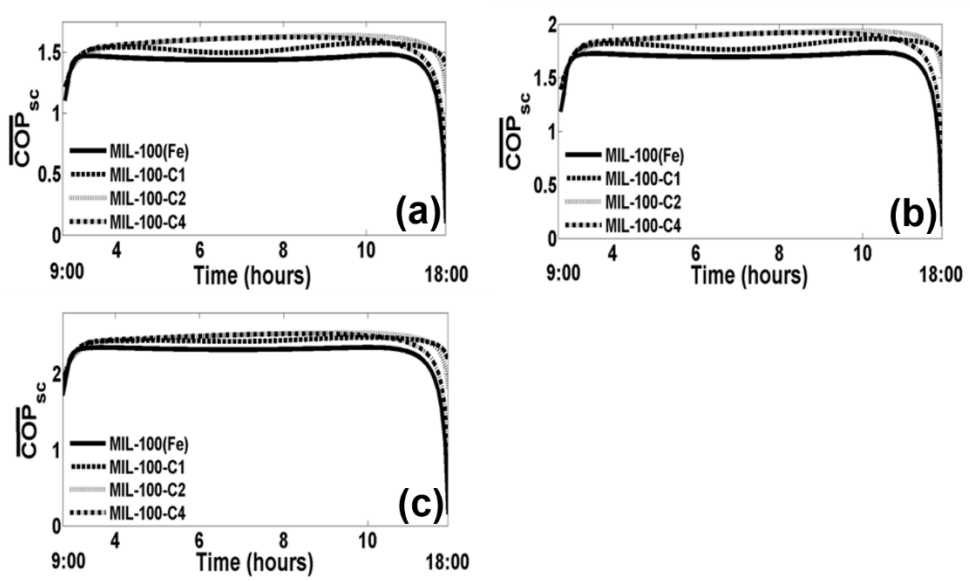

Fig 5.9: Variation of $\overline{COP_{sc}}$ as a function of chiller operation time for solar collector using **(a)** S-G cover, **(b)** D-G cover, and **(c)** S-G cover with TIM (initial preheating period of 2.67 hrs).

preheating period of 2.67 hours and a collector area of 35 m^2 for each of the four adsorbent materials and the three solar collector configurations used for the study. It can be generally observed that all the three performance measures attain their highest values for MIL-100-C2 being the adsorbent material for the adsorption chiller, and again start to decline for the case of MIL-100-C4. More specifically, in terms of solar collector configuration, the D-G collector results in the highest value of $\overline{SCP}$, the S-G collector with TIM results in the highest value of $\overline{COP_{sc}}$, while the S-G collector results in the highest value of *COP*.

Figure 5.11 shows the variation of minimum evaporator temperature, as well as the absolute difference between the maximum adsorption and desorption rate coefficients, with

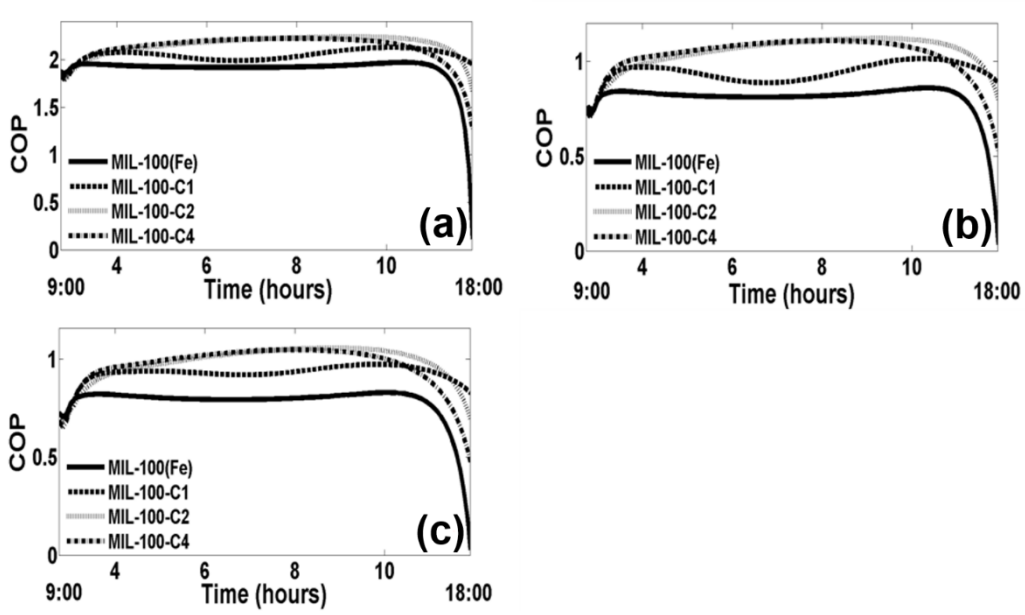

Fig 5.10: Variation of *COP* as a function of chiller operation time for solar collector using **(a)** S-G cover, **(b)** D-G cover, and **(c)** S-G cover with TIM (initial preheating period of 2.67 hrs).

the solar collector surface area for the case of MIL-100-C2. It can be observed that $T_{evap,\min}$ decreases while $\left|K_{a,\max} - K_{d,\max}\right|$ increases with increase in the value of A_c. It can be further observed that, for all values of A_c, the S-G collector results in the lowest $T_{evap,\min}$, while the S-G collector with TIM results in lowest $\left|K_{a,\max} - K_{d,\max}\right|$. However, since there is a negligible difference in the values of $T_{evap,\min}$ obtained using S-G and D-G collectors at A_c = 35, and in the values of $\left|K_{a,\max} - K_{d,\max}\right|$ evaluated using D-G and S-G collector with TIM at A_c = 10, we can conclude that a D-G solar collector is recommended for

Table 5.4 – Peak values of $\overline{SCP}$, $\overline{COP_{sc}}$ and *COP* for each of the four adsorbent materials and the three solar collector configurations used for the study (initial preheating period of 2.67 hrs).

	S-G			D-G			S-G with TIM		
Adsorbent	$\overline{SCP}$	$\overline{COP_{sc}}$	***COP***	$\overline{SCP}$	$\overline{COP_{sc}}$	***COP***	$\overline{SCP}$	$\overline{COP_{sc}}$	***COP***
MIL-100(Fe)	366.6	1.48	1.97	418.0	1.73	0.86	375.9	2.35	0.83
MIL-100-C1	431.3	1.58	2.13	482.4	1.86	1.02	438.6	2.48	0.98
MIL-100-C2	525.9	1.64	2.24	571.6	1.94	1.12	497.8	2.54	1.06
MIL-100-C4	520.4	1.62	2.23	569.8	1.92	1.11	496.5	2.53	1.05

achieving a high cooling capability coupled with a more stable functioning of the adsorption chiller in the context of commercial application. Figure 5.12 displays the variation of the cycle-averaged values of $\overline{SCP}$ and $\overline{COP_{sc}}$ with solar collector area for the three collector configurations. A pre-heating time of 2.67 hours and MIL-100-C2 as the adsorbent material have been employed to generate the two sub-plots shown in the figure. It can be observed that the cycle-averaged value of $\overline{SCP}$ increases, while the cycle-averaged value of $\overline{COP_{sc}}$ decreases with increasing collector area. It is worth mentioning here that $\overline{SCP}$ is a measure of the cooling power of the adsorption chiller per unit adsorbent mass as highlighted in equation (5.17). However, since the mass of the adsorbent is kept constant, an increase in the total amount of solar energy entering the collector with

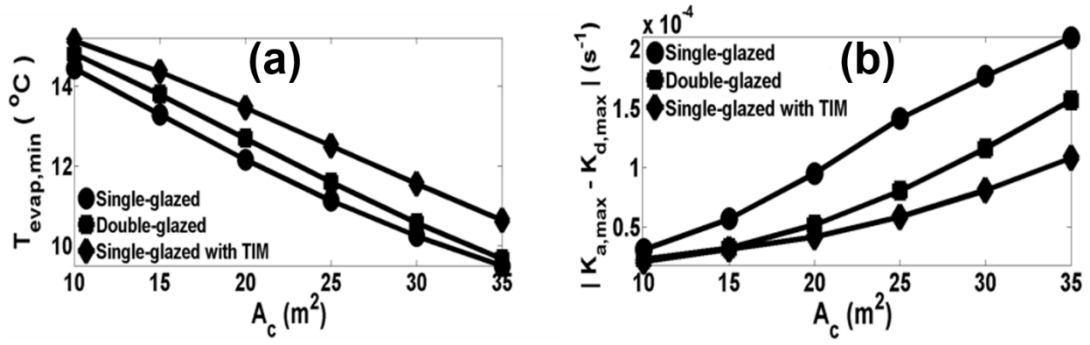

Fig 5.11: Variation of **(a)** minimum evaporator temperature, and **(b)** absolute difference between maximum adsorption and desorption rate coefficients, for different collector configurations and MIL-100-C2 as the adsorbent material.

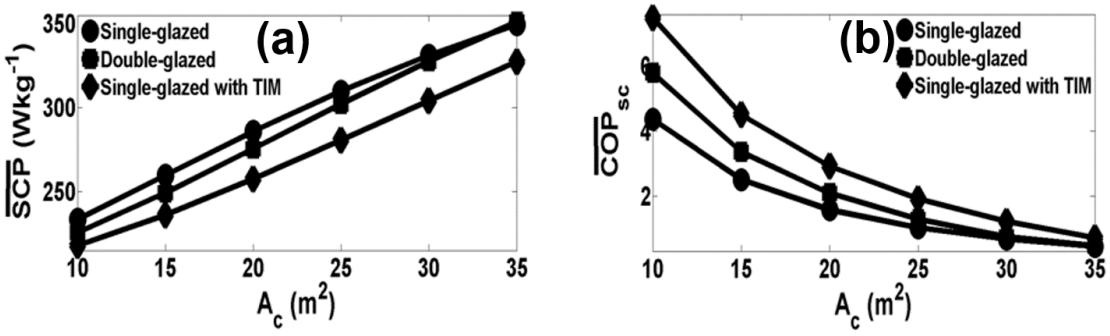

Fig 5.12: Variation of the cycle-averaged values of **(a)** $\overline{SCP}$ and **(b)** $\overline{COP_{sc}}$ with solar collector surface area for the three selected collector configurations for MIL-100-C2.

increasing collector area is expected to accelerate the rate of refrigerant desorption from a fixed volume of the adsorbent thus increasing the cooling power of the system. On the other hand, $\overline{COP_{sc}}$ is a measure of the cooling power of the adsorption chiller normalized

with respect to the total amount of solar energy entering the collector as evident from equation (5.20). However, since the rate of increase of solar energy input with increasing collector area has been experienced to be higher than the corresponding rate of increase of cooling power of the chiller in the numerical simulation, a resultant decline $\overline{COP_{sc}}$ is expected with increasing collector area as physically observed in Figure 5.12 (b). Finally, it can be seen in Figure 5.12 that the sequence of collector configurations resulting in the lowest-to-highest (or vice-versa) values of $\overline{SCP}$, for a fixed collector area in Figure 5.12 (a), appears as an exactly inverse sequence in case of $\overline{COP_{sc}}$ for the same collector area in Figure 5.12 (b).

Table 5.5 summarizes the peak values of the three performance measures observed during the course of chiller operation with an initial preheating period of 1.67 hours and a collector area of 35 m^2 for each of the four adsorbent materials and the three solar collector configurations used for the study. As observed earlier in Table 5.4, all the three performance measures attain their highest values for MIL-100-C2 being the adsorbent material for the adsorption chiller, and again start to decline for the case of MIL-100-C4. More specifically, the value of $\overline{COP_{sc}}$ drops very sharply when the adsorbent material is shifted from MIL-100-C2 to MIL-100-C4. In terms of solar collector configuration, the D-G collector results in the highest value of $\overline{SCP}$, the S-G collector with TIM results in the highest value of $\overline{COP_{sc}}$, while the S-G collector results in the highest value of *COP*. These are exactly the same observations which have been deduced earlier from Table 5.4. Finally, a comparison of Tables 5.4 and 5.5 reveals that the values of $\overline{COP_{sc}}$ and *COP* remain more or less unaffected when the initial pre-heating period is reduced by 1 hour; however, there

Table 5.5 – Peak values of $\overline{SCP}$, $\overline{COP_{sc}}$ and *COP* for each of the four adsorbent materials and the three solar collector configurations used for the study (initial preheating period of 1.67 hrs).

	S-G			D-G			S-G with TIM		
Adsorbent	$\overline{SCP}$	$\overline{COP_{sc}}$	***COP***	$\overline{SCP}$	$\overline{COP_{sc}}$	***COP***	$\overline{SCP}$	$\overline{COP_{sc}}$	***COP***
MIL-100(Fe)	271.6	1.49	1.98	272.0	1.75	0.87	270.2	2.37	0.83
MIL-100-C1	336.4	1.58	2.13	336.3	1.87	1.02	332.8	2.49	0.98
MIL-100-C2	430.8	1.64	2.24	424.5	1.94	1.12	390.5	2.55	1.06
MIL-100-C4	425.2	0.10	2.23	422.9	0.13	1.11	389.4	0.12	1.05

is a significant decline observed in the values of $\overline{SCP}$ for each of the 12 solar collector-adsorbent material combinations when the initial pre-heating period is reduced from 2.67 to 1.67 hours.

It can be noticed from the foregoing discussion that MIL-100-C2 results in the highest values of all the three performance measures for the three types of solar collector configurations as well as the two initial preheating periods selected for the study. The most probable reason for this observation is the relatively higher water vapor uptake exhibited by this material as compared to MIL-100(Fe), MIL-100-C1, and MIL-100-C4 (Figure 4.14). For this reason, this material is recommended for use as adsorbent in commercial-scale adsorption chillers.

5.7. Conclusions

The following conclusions can be drawn regarding the performance prediction of the solar adsorption chiller with the three selected collector configurations and four adsorbent materials:

1. MIL-100-C2 results in the highest predicted peak values for all the three performance measures, $\overline{SCP}$, and *COP*, regardless of which combination of the three selected solar collector configurations and the two initial preheating periods is used.
2. The values of $\overline{COP_{sc}}$ and *COP* remain more or less unaffected when the initial pre-heating period is reduced by 1 hour; however, there is a significant decline observed in the values of $\overline{SCP}$ for each of the 12 selected solar collector-adsorbent material combinations when the initial pre-heating period is reduced from 2.67 to 1.67 hours.
3. The cycle-averaged value of $\overline{SCP}$ increases, while the cycle-averaged value of $\overline{COP_{sc}}$ decreases with increasing solar collector surface area, except for the case of single-glazed solar collector for which the value of $\overline{COP_{sc}}$ starts to increase gradually beyond A_c = 15.
4. The sequence of collector configurations which results in increasing or decreasing values of $\overline{SCP}$, for a fixed value of solar collector surface area, appears as an exactly inverse sequence in case of $\overline{COP_{sc}}$ for the same value of collector area.
5. The minimum evaporator temperature is observed to decrease whereas the absolute difference between the maximum adsorption and desorption rate coefficients is observed to increase with increasing solar collector surface area.

6. A double-glazed solar collector and MIL-100-C2 as the adsorbent material appears to be the most appropriate combination for achieving a high cooling capability coupled with a more stable functioning of the adsorption chiller in the context of commercial application.

CHAPTER 6

CONCLUSIONS AND RECOMMENDATIONS

6.1. Research outcome and cost analysis

This dissertation presents four types of graphene-incorporated MOF-based composites as candidate adsorbent materials for use in solar-powered adsorption chillers using water as refrigerant – MWCNT/MIL-100(Fe), GO/MIL-100(Fe), MWCNT/MIL-101(Cr) and GO/MIL-101(Cr). Since the use of trivalent Fe is known to be environmentally friendly, while the use of trivalent Cr requires precautionary measures if dealt in exceptionally large quantities, the use of first two composite adsorbents seems favorable over the last two composites in the context of a commercial application. Despite the fact that the MWCNT/MIL-101(Cr) composite containing 6.9 wt % MWCNTs results in a water vapor uptake of 1.72 gg^{-1}, which according to the best knowledge of the author is the highest uptake ever reported for a water-stable MOF, the health and safety concerns raised by the environmental protection agency pertaining to the practical use of a Cr-based adsorbent for commercial adsorption chillers is expected to be a definite issue. In addition, the hydrothermal cyclic stability measured in this work for MWCNT/MIL-101(Cr) composite has not been observed to be better than either of the first two types of composites in the context of commercial chiller applications. With regards to cost-effectiveness as a means to assess industrial scalability, the retail price of $Cr(NO_3)_3.9H_2O$ (99% purity) is \$2200–2350 per metric ton [179] compared to \$100–800 per metric ton for $Fe(NO_3)_3.9H_2O$ (99% purity) [180], while the retail price of BDC is \$800–1500 per metric ton [181] compared

to \$150–2000 per metric ton for BTC [182]. This cost comparison is illustrated in a graphical format in Figure 6.1. As evident by the size comparison of the two double-sided arrows shown in the figure, the combination of $Fe(NO_3)_3.9H_2O$ with BTC seems more economical than the combination of $Cr(NO_3)_3.9H_2O$ with BDC as far as the commercial-scale synthesis of each of the two selected MOFs is concerned.

In other words, a cost-effective industrial-scale of synthesis of MIL-100(Fe) and its composites is also favored over MIL-101(Cr) apart from environmental concerns pertaining to the presence of Cr as discussed above. Table 6.1 summarizes the maximum water vapor uptakes at 298 K, as well as the cyclic stabilities for each of the four types of composites with the respective weight fractions of MWCNTs/GO, where the values have been normalized *w.r.t.* the corresponding value observed for the base MOF. It can be easily seen that the MWCNT/MIL-101(Cr) composite containing 6.9 wt% MWCNTs outperforms all the other materials *w.r.t.* maximum water uptake, while the GO/MIL-100(Fe) composite containing 6.5 wt% GO shows the highest cyclic stability amongst all the materials on exposure to 21 consecutive adsorption-desorption cycles. However, a closer examination of Table 6.1 suggests that the most optimum combination of uptake and cyclic stability is exhibited by the GO/MIL-100(Fe) composite containing 16 wt% GO which has been observed to exhibit a 22 wt% higher uptake than pristine MIL-100(Fe) at 298 K, and a 50% lower uptake loss measured between the first and the last cycles during cyclic adsorption-desorption (Section 4.5). Figure 6.2 displays the normalized performances in terms of the maximum water uptakes and the corresponding cyclic stabilities for the respective weight percentages of MWCNTs or GO for each of the four types of composites. It can be observed that the best combination of water uptake and cyclic

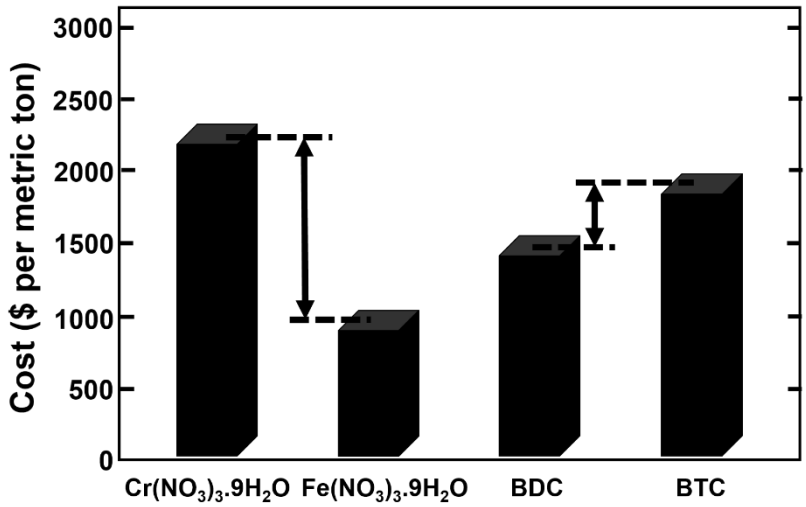

Fig 6.1: A comparison of retail price of each of the four raw materials needed for the synthesis of MIL-100(Fe) and MIL-101(Cr) [179–182].

stability is exhibited by the 17.75 wt% GO/MIL-100(Fe) composite. Hence, the outcome of this study recommends the use of a GO/MIL-100(Fe) composite containing 17.75 wt% GO as the most performance-efficient and cost-effective adsorbent material for use in commercial scale adsorption chillers using water as refrigerant.

6.2. Value to the Kingdom of Saudi Arabia

In an adsorption refrigeration system, hot water from a hot water storage tank is used to desorb the refrigerant from the desorption bed as shown schematically in Figure 2.1. However, the source of heating the water stored in the hot water tank is completely arbitrary which can be either thermal, electrical, solar, or even waste heat released from the industrial sector [17]. The vapor-compression refrigeration systems generally utilize an electrically-driven compressor where the source of electricity most commonly employed is hydropower, and rarely solar energy which is then converted into electrical power using

Table 6.1 – Maximum water vapor uptakes at 298 K and corresponding cyclic stabilities for each adsorbent material category selected in the study.

Adsorbent material	MWCNT/GO content (wt%)	Normalized max. uptake (%)	Normalized cyclic stability (%)
MIL-100(Fe)	0	100	100
MWCNT/MIL-100(Fe)	3.74	91.33	111.74
	8.13	101.20	85.72
	13.99	96.25	99.84
GO/MIL-100(Fe)	10.14	95.69	124.58
	19.99	79.91	100.41
	17.75	**124.97**	**122.15**
MIL-101(Cr)	0	100	100
MWCNT/MIL-101(Cr)	3.5	124.06	85.90
	5.1	132.71	91.54
	6.9	179.48	86.41
GO/MIL-101(Cr)	2.7	90.31	93.59
	6.97	91.46	103.53
	11.6	96.44	46.98

Note: Cyclic stability is defined as uptake recorded at last cycle as a percentage of uptake recorded at first cycle.

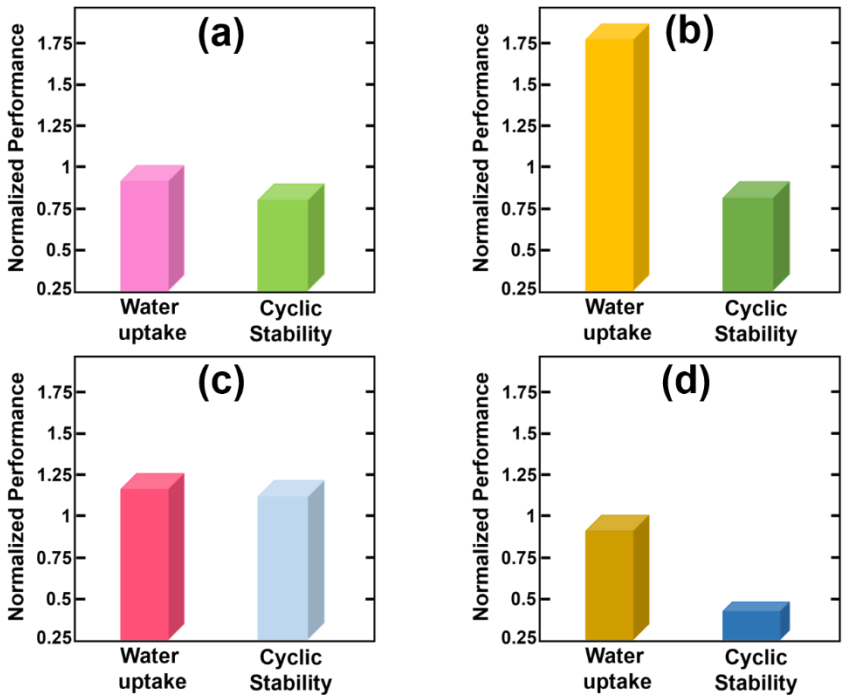

Fig 6.2: A comparison of normalized performances in terms of maximum water uptake and corresponding cyclic stability for each type of composite selected in the study: **(a)** 8.13 wt% MWCNT/MIL-100(Fe), **(b)** 6.9 wt% MWCNT/MIL-101(Cr), **(c)** 17.75 wt% GO/MIL-100(Fe) and **(d)** 11.6 wt% GO/MIL-101(Cr).

solar modules. However, the most highly efficient solar panels available commercially are capable of converting a maximum of 22% of the incident solar energy into electrical power which cannot be considered a commercially feasible value [183]. Moreover, considering the volume of the hot water storage tanks designed for commercial adsorption chiller applications, a tremendous amount of electricity consumption would be involved in induction heating along with the associated corrosion-related problems. In contrast, a solar adsorption refrigeration system makes direct use of the incident solar rays to heat up the

water in the hot water storage tank during an initial preheating period employing efficiently designed solar collector configurations (Figure 5.1). The Kingdom of Saudi Arabia is well-known for its geographical location in the so-called “sun-belt” making it one of the largest solar energy producers worldwide [184]. Hence, the concept of solar-powered adsorption refrigeration systems becomes most applicable to a country like Saudi Arabia given the continuously rising demands of refrigeration and air-conditioning in this region with growing population along with the corresponding increase in the unit cost of electricity, as well as the uncontrollable emission of flue gases like Carbon dioxide (CO_2), Sulphur dioxides (SO_2) and nitrogen oxides (NO_x) from the burning of fossil fuels for electrical power generation, which are a constant obstacle towards a clean environment and healthy living standards for its inhabitants at large [184].

APPENDICES

Appendix A: Acid treatment of MWCNTs and GNPs

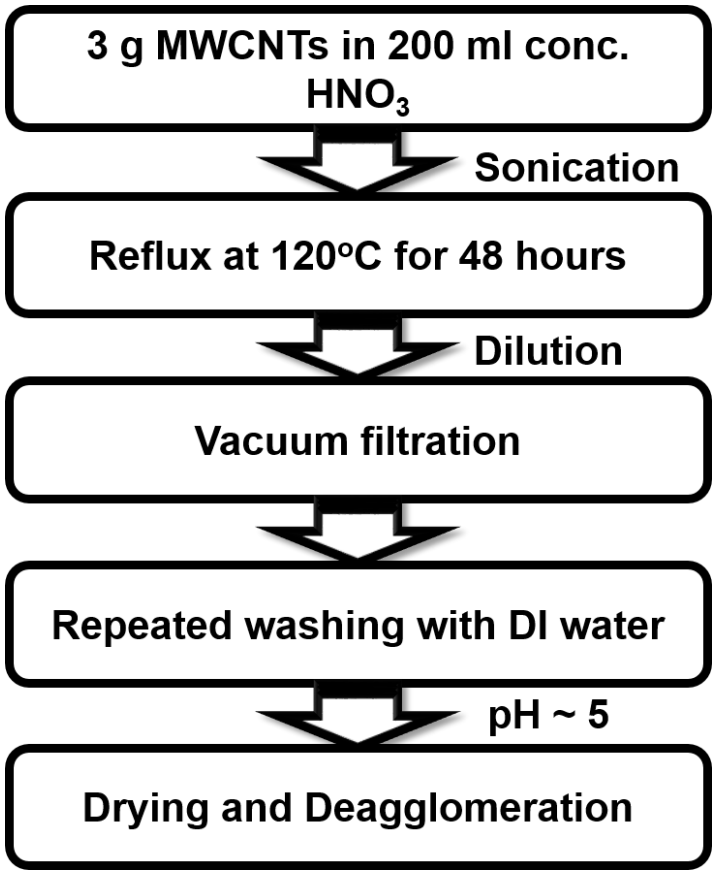

Fig A.1: Flow chart showing the acid-treatment of MWCNTs

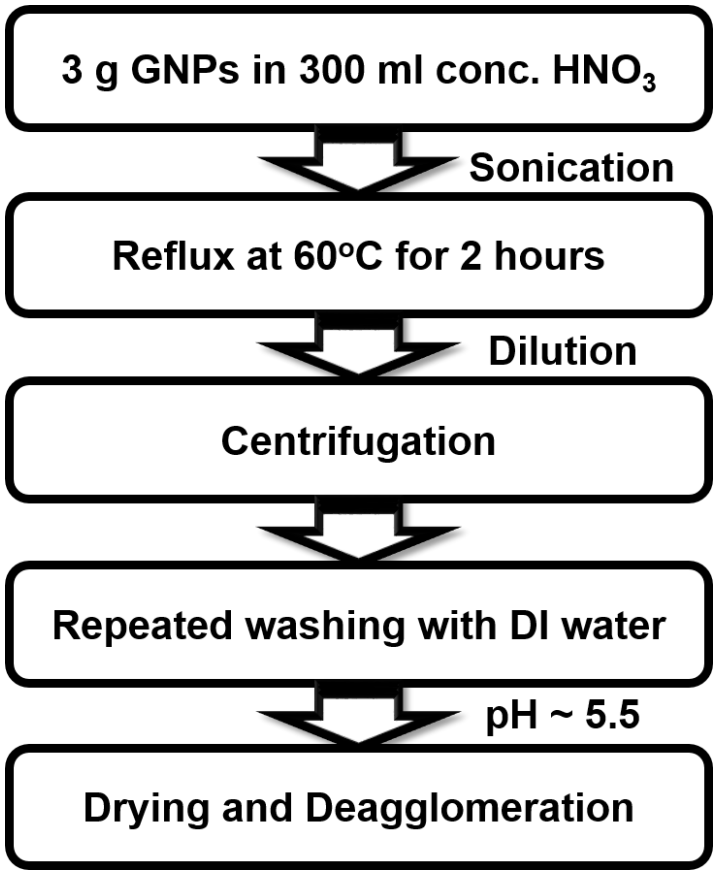

Fig A.2: Flow chart showing the acid-treatment of GNPs

Appendix B: Synthesis of MWCNT/ or GNP/MIL-100(Fe) composites

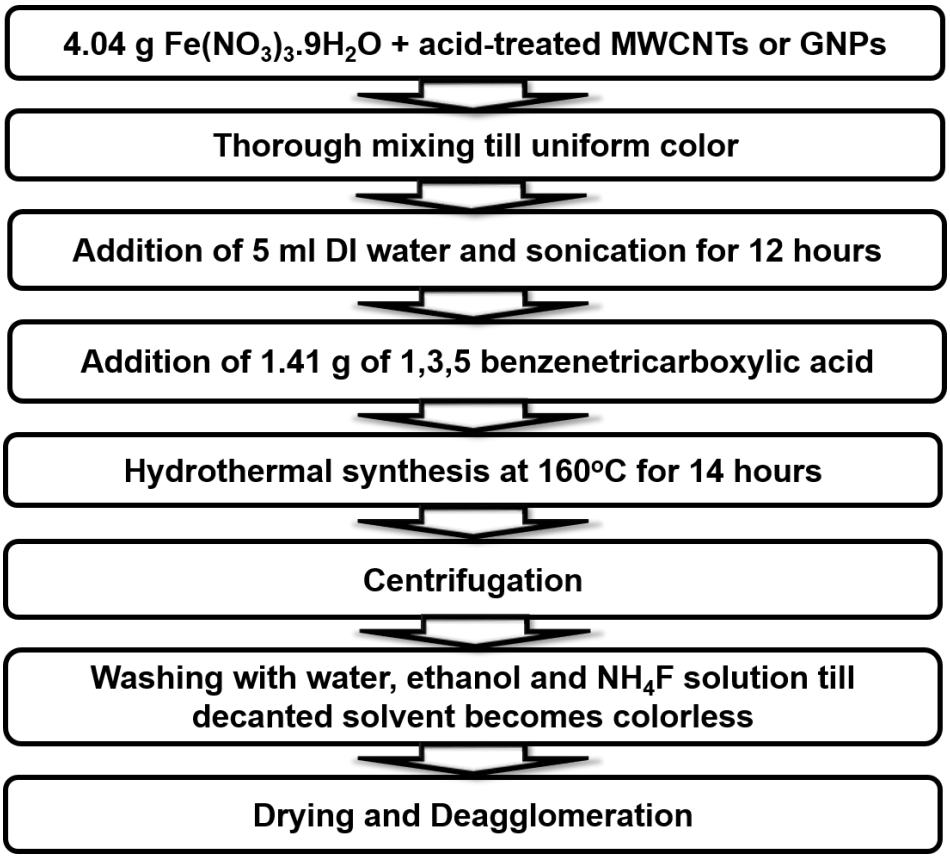

Fig B.1: Flow chart showing the synthesis of MWCNT/ or GNP/MIL-100(Fe) composites.

Appendix C: Synthesis of MWCNT/ or GNP/MIL-101(Cr) composites

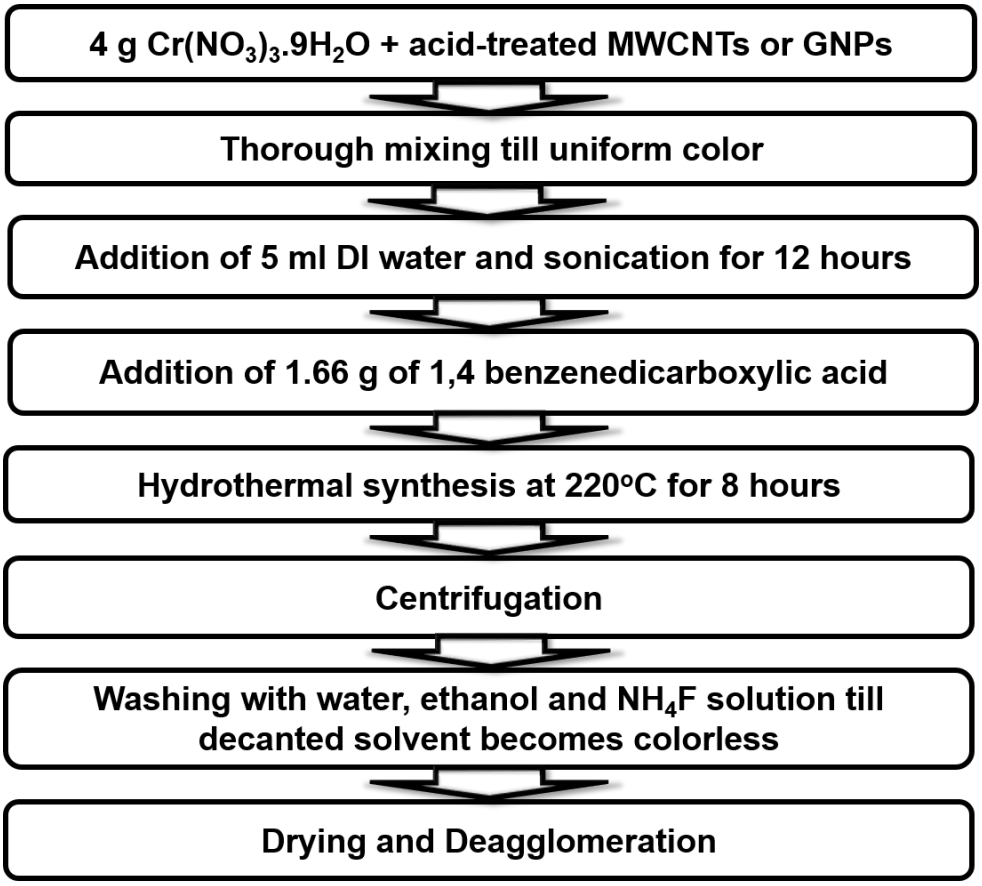

Fig C.1: Flow chart showing the synthesis of MWCNT/ or GNP/MIL-101(Cr) composites.

Appendix D: Error analysis for BET surface area estimation for MIL-100(Fe), MIL-101(Cr) and MWCNT/MIL-100(Fe) composites

Table D.1 – Error analysis regarding measurement of BET surface area.

Material	**BET surface area measurement trials (m^2g^{-1})**						**Mean**	**Std. Dev.**	**Error (%)**
	1	2	3	4	5	6			
MIL-100(Fe)	1360	1374	1575	1442	1320	1390	1410	90.05	6.40
MIL-101(Cr)	3650	3960	-	-	-	-	3805	219.20	5.76
MIL-100-C1	1011	1140	-	-	-	-	1076	91.22	8.48

Note:

Reported value for MIL-100(Fe) using same synthesis method = 1520 m^2g^{-1} [136].

Reported value for MIL-101(Cr) using same synthesis method = 3314 m^2g^{-1} [135].

MIL-100(C1) = 5.9 wt% MWCNT/MIL-100(Fe) composite.

MIL-101(C2) = 3.5 wt% MWCNT/MIL-101(Fe) composite.

MIL-101(C3) = 3.74 wt% MWCNT/MIL-100(Fe) composite.

$$\% \text{ Error} = \frac{\text{Std. Dev.}}{\text{Mean}} \times 100$$

NOMENCLATURE

A	heat transfer area (m^2)
C_p	specific heat capacity (J kg^{-1} K^{-1})
D_{s0}	pre-exponential constant for surface diffusion (m^2 sec^{-1})
E	activation energy (J mol^{-1})
I	solar radiation intensity (W m^{-2})
$\dot{m}$	mass flow rate (kg sec^{-1})
P	water vapor pressure (Pa)
R	specific gas constant (J kg^{-1} K^{-1})
R_p	average particle radius (m)
T	temperature (K)
U	overall heat transfer coefficient (W m^{-2} K^{-1})
t	time (s)

Subscripts/Superscripts

ads	adsorbent
a	adsorption
Al	aluminum heat exchanger tubes
b	bed
ch	chilled water
con	condenser
Cu	copper heat exchanger tubes
cw	cooling water
d	desorption
dg	double-glazed
evap	evaporator tubes
g	water vapor
hw	heating water
i	inlet
L	loss
m	matrix
o	outlet
r	refrigerant
s	saturation
sc	solar collector
sg	single-glazed
sr	sunrise
ss	sunset
w	water

Greek symbols

ΔH	enthalpy of adsorption (J kg^{-1})
ΔL	vaporization enthalpy (J kg^{-1})
τ	transmissivity
Δx	differential amount of vapor refrigerant adsorbed ($kg^{-1}kg^{-1}$)
Ω	lumped capacitance (J K^{-1})

REFERENCES

[1] K. Sumathy, L. Yong, H.M. Steinhagen, H. Kerskes, Performance analysis of a modified two-bed solar-adsorption air-conditioning system, Int. J. Energ. Res. 33 (2009) 675–686.

[2] N.H. Abu Hamdeh, M.A. Al-Muhtaseb, Optimization of solar adsorption refrigeration system using experimental and statistical techniques, Energy Convers. Manage. 51 (2010) 1610–1615.

[3] G.M. Tashtoush, A Statistical Approach to Optimize the Solar Adsorption Refrigeration System, Energy Sci. Tech. 3 (2) (2012) 18–28.

[4] M. Laidi, S. Hanini, Optimal Solar COP Prediction of a Solar-Assisted Adsorption Refrigeration System Working with Activated Carbon/Methanol as Working Pairs using Direct and Inverse Artificial Neural Network, Int. J. Refrig. 36 (2013) 247–257.

[5] N.O. Omisanya, C.O. Folayan, S.Y. Aku, S.S. Adefila, R.B.O. Suleiman, Comparison of Experimental Measurements and Simulation of Solar (Zeolite 4A-Water) Adsorption Refrigerator Using Trnsys and Matlab Softwares, Rev. Appl. Phys. 2 (4) (2013) 114–127.

[6] R.G. Oliveira, R.Z. Wang, J.K. Kiplagat, C.Y. Wang, Novel composite sorbent for resorption systems and for chemisorption air conditioners driven by low generation temperature, Renew. Energy 34 (2009) 2757–2764.

[7] L. Wang, L. Chen, H.L. Wang, D.L. Liao, The adsorption refrigeration characteristics of alkaline-earth metal chlorides and its composite adsorbents, Renew. Energy 34 (2009) 1016–1023.

[8] H. Huang, T. Oike, F. Watanabe, Y. Osaka, N. Kobayashi, M. Hasatani, Development research on composite adsorbents applied in adsorption heat pump, Appl. Therm. Eng. 30 (2010) 1193–1198.

[9] L.W. Wang, Z. Tamainot-Telto, R. Thorpe, R.E. Critoph, S.J. Metcalf, R.Z. Wang, Study of thermal conductivity, permeability, and adsorption performance of consolidated composite activated carbon adsorbent for refrigeration, Renew. Energy 36 (2011) 2062–2066.

[10] C.Y. Tso, C.Y.H. Chao, Activated carbon, silica-gel and calcium chloride composite adsorbents for energy efficient solar adsorption cooling and dehumidification systems, Int. J. Refrig. 35 (2012) 1626–1638.

[11] H. Li, X. Bu, L. Wang, Z. Lu, W. Ma, Composite adsorbents of $CaCl_2$ and sawdust prepared by carbonization for ammonia adsorption refrigeration, Front. Energy 6 (4) (2012) 356–360.

[12] A. Freni, A. Sapienza, I.S. Glaznev, Y.I. Aristov, G. Restucci, Experimental testing of a lab-scale adsorption chiller using a novel selective water sorbent “silica modified by calcium nitrate”, Int. J. Refrig. 35 (2012) 518–524.

[13] K.C. Chan, C.Y.H. Chao, G.N. Sze-To, K.S. Hui, Performance predictions for a new zeolite 13X/$CaCl_2$ composite adsorbent for adsorption cooling systems, Int. J. Heat Mass Tran. 55 (2012) 3214–3224.

[14] XB Bu, LB Wang, HS Li, ZN Lu, "Preparation of composite adsorbent of sawdust and $CaCl_2$ by carbonization method for creating pore", Sci China Technol Sc., 55(9) (2012) 2404–2408.

[15] L. Wang, X. Bu, H. Li, W. Ma, Preparation and performance testing of composite adsorbents for solar adsorption refrigeration, Adsorpt. Sci. Technol., 31 (7) (2013) 573–582.

[16] H. Ye, Z. Yuan, S. Li, L. Zhang, Activated carbon fiber cloth and $CaCl_2$ composite sorbents for a water vapor sorption cooling system, Appl. Therm. Eng., 62 (2014) 690–696.

[17] S. K. Henninger, F. Jeremias, H. Kummer, C. Janiak, "MOFs for Use in Adsorption Heat Pump Processes", Eur. J. Inorg. Chem., 2012 (2012) 2625-2634.

[18] C. Li, R.Z. Wang, L.W. Wang, T.X. Li, Y. Chen, 2013, "Experimental Study on an Adsorption Icemaker Driven by Parabolic Trough Solar Collector,"Renewable Energy, 57, pp. 223-233.

[19] M. Alkhair, M. Y. Sulaiman, K. Sopian, C. H. Lim, E. Salleh, S. Mat, B. B. Saha, "Design and Modeling of One Refrigeration Ton Solar Assisted Adsorption Air Conditioning System", J Sol Energy Eng., 137 (2015) 011005-1–011005-9.

[20] T. Núñez, H.-M. Henning, W. Mittelbach, "Adsorption Cycle Modelling: Characterization and Comparison of Materials", Proc. of International Sorption Heat Pump Conference, 1999 (1999).

[21] Y.I. Aristov, M.M. Tokarev, A. Freni, I.S. Glaznev, G. Restuccia, "Kinetics of water adsorption on silica Fuji Davison RD", Microporous Mesoporous Mater., 96 (2006) 65-71.

[22] B.B. Saha, A. Akisawa, T. Kashiwagi, “Silica gel water advanced adsorption refrigeration cycle”, Energy, 22 (1997) 437-447.

[23] K.C. Ng, H.T. Chua, C.Y. Chung, C.H. Loke, T. Kashiwagi, A. Akisawa, B.B. Saha, “Experimental investigation of the silica gel-water adsorption isotherm characteristics”, Appl. Therm. Eng., 21 (2001) 1631-1642.

[24] D. Wang, Z. Xia, J. Wu, R. Wang, H. Zhai, W. Dou, “Study of a novel silica gel–water adsorption chiller. Part I. Design and performance prediction”, Int. J. Refrig., 28 (2005) 1073-1083.

[25] T. Núñez, W. Mittelbach, H.-M. Henning, “Development of an adsorption chiller and heat pump for domestic heating and air-conditioning applications”, Appl. Therm. Eng., 27 (2007) 2205-2212.

[26] E.-P. Ng, S. Mintova, “Nanoporous materials with enhanced hydrophilicity and high water sorption capacity”, Microporous Mesoporous Mater., 114 (2008) 1-26.

[27] S. K. Henninger, F. Jeremias, H. Kummer, P. Schossig, H-M Henning, “Novel sorption materials for solar heating and cooling”, Energy Procedia, 30 (2012) 279-288.

[28] S.K. Henninger, F.P. Schmidt, H.M. Henning, “Characterisation and improvement of sorption materials with molecular modeling for the use in heat transformation applications”, Adsorption, 17 (2011) 833-843.

[29] S.K. Henninger, F.P. Schmidt, H.M. Henning, “Water adsorption characteristics of novel materials for heat transformation applications”, Appl. Therm. Eng., 30 (2010) 1692-1702.

[30] H. van Heyden, G. Munz, L. Schnabel, F. Schmidt, S. Mintova, T. Bein, "Kinetics of water adsorption in microporous aluminophosphate layers for regenerative heat exchangers", Appl. Therm. Eng., 29 (2009) 1514-1522.

[31] H. van Heyden, S. Mintova, T. Bein, "AlPO-18 nanocrystals synthesized under microwave irradiation", J. Mater. Chem., 16 (2006) 514-518.

[32] J. Bauer, R. Herrmann, W. Mittelbach, W. Schwieger, "Zeolite/aluminum composite adsorbents for application in adsorption refrigeration", Int. J. Energ. Res., 33 (2009) 1233-1249.

[33] C. Janiak, "Funk .tionelle organische Zeolith-Analoga auf der Grundlage metallorganischer Koordinationsnetzwerke", Angew. Chem., 109 (1997) 1499-1502.

[34] C. Janiak, "Functional Organic Analogues of Zeolites Based on Metal- Organic Coordination Frameworks", Angew. Chem. Int. Ed. Engl., 36 (1997) 1431-1434.

[35] H. Li, M. Eddaoudi, M. O'Keeffe, O. M. Yaghi, "Design and synthesis of an exceptionally stable and highly porous metal-organic framework", Nature, 402 (1999) 276-279.

[36] O. M. Yaghi, M. O'Keeffe, N. W. Ockwig, H. K. Chae, M. Eddaoudi, J. Kim, "Reticular synthesis and the design of new material", Nature, 423 (2003) 705-714.

[37] J. Rowsell, O. M. Yaghi, "Metal–organic frameworks: a new class of porous materials", Microporous Mesoporous Mater., 73 (2004) 3-14.

[38] G. Férey, C. Mellot-Draznieks, C. Serre, F. Millange, J. Dutour, S. Surblé, I. Margiolaki, "A Chromium Terephthalate-Based Solid with Unusually Large Pore Volumes and Surface Area", Science, 309 (2005) 2040-2042.

[39] G. Férey, “Hybrid porous solids: past, present, future”, Chem. Soc. Rev., 37 (2008) 191-214.

[40] G. Férey, C. Serre, “Large breathing effects in three-dimensional porous hybrid matter: facts, analyses, rules and consequences”, Chem. Soc. Rev., 38 (2009) 1380-1399.

[41] G. Férey, “Some suggested perspectives for multifunctional hybrid porous solids”, Dalton Trans., (2009) 4400-4415.

[42] R. J. Kuppler, D. J. Timmons, Q.-R. Fang, J.-R. Li, T. A. Makal, M. D. Young, D. Yuan, D. Zhao, W. Zhuang, H.-C. Zhou, “Potential applications of metal-organic frameworks”, Coord. Chem. Rev., 253 (2009) 3042-3066.

[43] K. Hindson, “Quo vadis MOFs?”, Eur. J. Inorg. Chem., (2010) 3683.

[44] S. Kitagawa, S. Natarajan, “Targeted Fabrication of MOFs for Hybrid Functionality”, Eur. J. Inorg. Chem., (2010) 3685.

[45] J. Ehrenmann, S.K. Henninger, C. Janiak, “Water Adsorption Characteristics of MIL-101 for Heat-Transformation Applications of MOFs”, Eur. J. Inorg. Chem., 2011 (2011) 471-474.

[46] S.K. Henninger, F. Jeremias, J. Ehrenmann, C. Janiak, “The potential of PCPs/MOFs for the use in Adsorption Heat Pump processes”, In: International Sorption Heat Pump Conference (ISHPC11), IIR/AICARR, Padova, Italy, 2011, pp. 415-424.

[47] F. Jeremias, A. Khutia, S.K. Henninger, C. Janiak, “MIL-100(Al, Fe) as water adsorbents for heat transformation purposes – a promising application”, J. Mater. Chem., 22 (2012) 10148-10151.

[48] P. Küsgens, M. Rose, I. Senkovska, H. Fröde, A. Henschel, S. Siegle, S. Kaskel, "Characterization of metal-organic frameworks by water adsorption", Microporous Mesoporous Mater., 120 (2009) 325-330.

[49] P. Küsgens, A. Zgaverdea, H.-G. Fritz, S. Siegle, S. Kaskel, "Metal-Organic Frameworks in Monolithic Structures", J. Am. Ceram. Soc., 93 (2010) 2476-2479.

[50] G. Akiyama, R. Matsuda, S. Kitagawa, "Highly Porous and Stable Coordination Polymers as Water Sorption Materials", Chem. Lett., 39 (2010) 360-361.

[51] O. M. Yaghi, M. O'Keeffe, N. W. Ockwig, H. K. Chae, M. Eddaoudi, J. Kim, "Reticular synthesis and the design of new materials", Nature, 423 (2003) 705-714.

[52] S. Kitagawa, R. Kitaura, S.-I. Noro, "Functional porous coordination polymers", Angew. Chem. Int. Ed., 43 (2004) 2334-2375.

[53] H. Li, M. Eddaoudi, T. L. Groy, O. M. Yaghi, "Establishing microporosity in open metal-organic frameworks: gas sorption isotherms for Zn(BDC) (BDC = 1,4-benzenedicarboxylate)", J. Am. Chem. Soc., 120 (1998) 8571-8572.

[54] H. Li, M. Eddaoudi, M. O'Keeffe, O. M. Yaghi, "Design and synthesis of an exceptionally stable and highly porous metal-organic framework", Nature, 402 (1999) 276-279.

[55] G. Blanita, D. Lupu, M. Lazar, A. R. Biris, V. Pascalau, O. Ardelean, I. Coldea, I. Misan, G. Popeneciu, M. Vlassa, "The effect of solution/free volume ratio on the MOF-5 characteristics", J. Phys.: Conf. Ser., 182 (2009) 012047-012049.

[56] R. J. Dombrowski, D. R. Hyduke, C. M. Lastoskie, "Pore Size Analysis of Activated Carbons from Argon and Nitrogen Porosimetry Using Density Functional Theory", Langmuir, 16 (2000) 5041-5050.

[57] R. F. S. Lenza, W. L. Vasconcelos, “Preparation of Silica by Sol-Gel Method Using Formamide”, Mater. Res., 4(3) (2001) 189-194.

[58] P. Pérez-Romo, H. Armendáriz-Herrera, J. S. Valente, M. de Lourdes Guzmán-Castillo, F. Hernández-Beltrán, J. J. Fripiat, “Crystallization of faujasite Y from seeds dispersed on mesoporous materials”, Micropor. Mesopor. Mat., 132 (2010) 363-374.

[59] H. Furukawa, K. E. Cordova, M. O’Keeffe, O. M. Yaghi, “The Chemistry and Applications of Metal-Organic Frameworks”, Science, 341 (2013) 974-986.

[60] Y. Yang, L. Ge, V. Rudolph, Z. Zhu, “In situ synthesis of zeolitic imidazolate frameworks/carbon nanotube composites with enhanced CO_2 adsorption”, Dalton Trans., 43 (2014) 7028-7036.

[61] K.P. Prasanth, P. Rallapalli, M. C. Raj, H.C. Bajaj, R. V. Jasra, “Enhanced hydrogen sorption in single walled carbon nanotube incorporated MIL-101 composite metaleorganic Framework”, Int. J. Hydrogen Eng., 36 (2011) 7594-7601.

[62] S. J. Yang, J. Y. Choi, H. K. Chae, J. H. Cho, K. S. Nahm, C. R. Park, “Preparation and Enhanced Hydrostability and Hydrogen Storage Capacity of CNT@MOF-5 Hybrid Composite”, Chem. Mater., 21 (2009) 1893-1897.

[63] Y. Zhao, H. Ding, Q. Zhong, “Synthesis and characterization of MOF-aminated graphite oxide composites for CO_2 capture”, Appl. Surf. Sci., 284 (2013) 138-144.

[64] H. Jiang, Y. Feng, M. Chen, Y. Wang, “Synthesis and hydrogen-storage performance of interpenetrated MOF-5/MWCNTs hybrid composite with high mesoporosity”, Int. J. Hydrogen Energ., 38 (2013) 10950-10955.

[65] D. Liu, J. J. Purewal, J. Yang, A. Sudik, S. Maurer, U. Mueller, J. Ni, D.J. Siegel, "MOF-5 composites exhibiting improved thermal conductivity", Int. J. Hydrogen Energ., 37 (2012) 6109-6117.

[66] M. Dupont, J. J. Guilleminot, F. Menuier, P. Nguyen, "Study of solar ice conservators using day night intermittent zeolite 13X–water cycle in temperate and tropical climates", Proceedings of meetings of Commission E1–E2, Jerusalem (issued by International Institute of Refrigeration), (1982) 193–200.

[67] Ph. Grenier, J. J. Guilleminot, M. Mester, F. Menuier, M. Pons, "Experimental results on a 12 m^2 solar powered coldstore using the intermittent zeolite 13X–water cycle", In: Solar World Congress, vol. 1, Pergamon Press (edited by S. V. Szokolay), (1984) p. 353.

[68] M. Pons, J. J. Guilleminot, "Design of a solar powered solid adsorption ice-maker", ASME J. of Solar Engineering, 108 (1986) 332–337.

[69] R. H. B. Exell, S. C. Bhattacharya, K. Sridha, Y. R. Upadhyaya, P. Wibulswas, "A charcoal-methanol solar refrigerator", ISES Solar World Congress, Hamburg, Germany, Sep. 13–18, 1987.

[70] M. Pons, P.H. Grenier, "Experimental data on a solar-powered ice maker using activated carbon and methanol adsorption pair", ASME. J. Solar Energy Eng., 109 (1987) 303–310.

[71] R. P. Klüppel, J. M. Gurgel, "Solar adsorption cooling using silica gel/water", Advances in solar energy technology, 3 (1987) 2627–2631.

[72] R.E. Critoph, "Laboratory testing of an ammonia carbon solar refrigerator", ISES, Solar World Congress, Budapest, Hungary, Aug. 23–26, 1993.

[73] S. K. Phillip, A. K. Singhal, C. S. Rao, S. Mohan, G. D. Sootha, "Zeolite based solar refrigerator", Research Report Sardal Patel Renewable Energy Research Institute, Gujrat, India, 1993.

[74] O. St. C. Headley, A. F. Kothdiwala, I. A. McDoom, "Charcoal-methanol adsorption refrigerator powered by a compound parabolic concentrating solar collector", Sol. Energy 53(2) (1994) 191–197.

[75] R. E. Critoph, "Evaluation of alternative refrigerant - adsorbent pairs for refrigeration cycles", Applied Thermal Engineering, 16(11) (1996) 891–900.

[76] K. Oertel, M. Fischer, "Adsorption cooling system for cold storage using methanol/silica gel", Applied Thermal Engineering, 18 (1998) 773–786.

[77] R. Z. Wang, J. Y. Wu, Y. X. Xu, Y. Teng, W. Shi, "Experiment on a continuous heat regenerative adsorption refrigerator using spiral plate heat exchanger as adsorbers", Appl. Thermal Engng., 18(1-2) (1998) 13–23.

[78] K. Sumathy, Z. F. Li, "Experiments with solar-powered adsorption ice-maker", Renewable Energy, 16(1-4) (1999) 704 707.

[79] R. Z. Wang, M. Li, Y. X. Xu, J. Y. Wu "An energy efficient hybrid system of solar powered water heater and adsorption ice maker", Solar Energy, 68(2) (2000) 189–195.

[80] Z. F. Li, K. Sumathy, "A solar-powered ice-maker with the solid adsorption pair of activated carbon and methanol", Int. J. Energy Res. 23(6) (1999) 517–527.

[81] R. Z. Wang, J. Y. Wu, Y. X. Xu, W. Wang, "Performance researches and improvements on heat regenerative adsorption refrigerator and heat pump", Energ. Convers. Manage., 42(2) (2001) 233–249.

[82] C. H. Li, R. Z. Wang, Y. Z. Lu, “Investigation of a novel combined cycle of solar powered adsorption-ejection refrigeration system”, Renewable Energy, 26(4) (2002) 611–622.

[83] G. Restuccia, A. Freni, S. Vasta, Y. Aristov, “Selective water sorbent for solid sorption chiller: experimental results and modeling”, Int. J. Refrigeration, 27 (2004) 284–293.

[84] F. Aghbalou, A. Mimet, F. Badia, J. Illa, A. El Bouardi, J. Bougard, “Heat and Mass Transfer During Adsorption of Ammonia in a Cylindrical Adsorbent Bed: Thermal Performance Study of a Combined Parabolic Solar Collector, Water Heat Pipe and Adsorber Generator Assembly”, Appl. Therm. Eng., 24(17–18) (2004) 2537–2555.

[85] C. Hildbrand, P. Dind, M. Pons, F. Buchter, “A New Solar Powered Adsorption Refrigerator With High Performance”, Sol. Energy, 77(3) (2004) 311–318.

[86] S. G. Wang, R. Z. Wang, X. R. Li, “Research and development of consolidated adsorbent for adsorption systems”, Renewable Energy, 30 (2005) 1425–1441.

[87] D.C. Wang, J. Y. Wu, Z. Z. Xia, H. Zhai, R. Z. Wang, W. D. Dou, “Study of a novel silica gel-water adsorption chiller. Part II: Experimental study”, Int. J. Ref. 28(7) (2005) 1084– 1091.

[88] F. Lemmini, A. Errougani, “Building and Experimentation of a Solar Powered Adsorption Refrigerator”, Renewable Energy, 30(13) (2005) 1989–2003.

[89] H. L. Luo, Y. J. Dai, R. Z. Wang, J. Y. Wu, Y. X. Xu, J. M. Shen, “Experimental Investigation of a Solar Adsorption Chiller Used for Grain Depot Cooling”, Appl. Therm. Eng., 26(11–12) (2006) 1218–1225.

[90] I. I. El-Sharkawy, K. Kuwahara, B. B. Saha, S. Koyama, K. C. Ng, "Experimental investigation of activated carbon fibers/ethanol pairs for adsorption cooling system application", Appl. Thermal Engng., 26(8-9) (2006) 859–865.

[91] Y. Liu, K. C. Leong, "Numerical study of a novel cascading adsorption cycle", Int. J. Ref., 29(2) (2006) 250–259.

[92] N. M. Khattab, "Simulation and Optimization of a Novel Solar-Powered Adsorption Refrigeration Module", Sol. Energy, 80(7) (2006) 823–833.

[93] T. Nunez, W. Mittelbach, H. M. Henning, "Development of an adsorption chiller and heat pump for domestic heating and air-conditioning applications", Appl. Thermal Engng., 27(13) (2007) 2205–2212.

[94] H. L. Luo, R. Z. Wang, Y. J. Dai, J. Y. Wu, J. M. Shen, B. B. Zhang, "An Efficient Solar-Powered Adsorption Chiller and Its Application in Low-Temperature Grain Storage", Sol. Energy, 81(5) (2007) 607–613.

[95] E. E. Anyanwu, N. V. Ogueke, "Transient Analysis and Performance Prediction of a Solid Adsorption Solar Refrigerator", Appl. Therm. Eng., 27(14–15) (2007) 2514–2523.

[96] M. I. González, L. R. Rodríguez, "Solar Powered Adsorption Refrigerator With CPC Collection System: Collector Design and Experimental Test", Energy Convers. Manage., 48(9) (2007) 2587–2594.

[97] M. Z. I. Khan, B. B. Saha, K. C. A. Alam, A. Akisawa, T. Kashiwagi, "Study on Solar/Waste Heat Driven Multi-Bed Adsorption Chiller With Mass Recovery", Renewable Energy, 32(3) (2007) 365–381.

[98] K. Daou, R. Wang, G. Yan, Z. Xia, “Theoretical comparison of the refrigerating performances of a $CaCl_2$ impregnated composite adsorbent to those of the host silica gel”, Int. J. Therm. Sci., 47(1) (2008) 68–75.

[99] H. Demir, “An experimental and theoretical study on the improvement of adsorption heat pump performance”, Ph.D. thesis, Chemical Engineering, İzmir Institute of Technology, İzmir, Turkey (2008).

[100] M. Elnekave, “Adsorption heat pumps for providing coupled heating and cooling effects in olive oil mills”, Int. J. Energ. Res., 32(6) (2008) 559–568.

[101] I. El-Sharkawy, B. Saha, S. Koyama, J. He, K. Ng, C. Yap, “Experimental investigation on activated carbon–ethanol pair for solar powered adsorption cooling applications”, Int. J. Ref., 31(8) (2008) 1407–1413.

[102] M. Kubota, T. Ueda, R. Fujisawa, J. Kobayashi, F. Watanabe, N. Kobayashi, M. Hasatani, “Cooling output performance of a prototype adsorption heat pump with fin-type silica gel tube module”, Appl. Therm. Eng., 28(2-3) (2008) 87–93.

[103] Y. Liu, K. C. Leong, “Numerical modeling of a zeolite/water adsorption cooling system with non-constant condensing pressure”, Int. Commun. Heat Mass 35(5) (2008) 618–622.

[104] N. V. Ogueke, E. E. Anyanwu, “Design Improvements for a Collector/ Generator/Adsorber of a Solid Adsorption Solar Refrigerator”, Renewable Energy, 33(11) (2008) 2428–2440.

[105] B. Saha, A. Chakraborty, S. Koyama, Y. Aristov, “A new generation cooling device employing CaCl2-in-silica gel–water system”, Int. J. Heat Mass Tran., 52(1-2) (2009) 516–524.

[106] J. Y. San, H. C. Hsu, “Performance of a multi-bed adsorption heat pump using SWS-1L composite adsorbent and water as the working pair”, Appl. Therm. Eng., 29(8-9) (2009) 1606–1613.

[107] D. C. Wang, J. P. Zhang, “Design and performance prediction of an adsorption heat pump with multi-cooling tubes”, Energ. Convers. Manage., 50(5) (2009) 1157–1162.

[108] Z. Z. Xia, R. Z. Wang, D. C. Wang, Y. L. Liu, J. Y. Wu, C. Chen, “Development and comparison of two-bed silica gel-water adsorption chillers driven by low-grade heat source”, Int. J. Therm. Sci., 48(5) (2009) 1017–1025.

[109] R. J. H. Grisel, S. F. Smeding, R. de Boer, “Waste heat driven silica gel/water adsorption cooling in trigeneration”, Appl. Therm. Eng., 30(8-9) (2010) 1039–1046.

[110] H. Z. Hassan, A. A. Mohamad, R. Bennacer, “Simulation of an adsorption solar cooling system”, Energy, 36(1) (2011) 530–537.

[111] Y. I. Aristov, G. Restuccia, G. Cacciola, V. Parmon, Appl. Therm. Eng., 22 (2002) 191–204.

[112] S. K. Henninger, F. P. Schmidt, H.-M. Henning, Appl. Therm. Eng., 30 (2010) 1692–1702.

[113] J. Canivet, A. Fateeva, Y. Guo, B. Coasne, D. Farrusseng, “Water adsorption in MOFs: fundamentals and applications”, Chem. Soc. Rev., 43 (2014) 5594–5617.

[114] L. Huang, H. Wang, J. Chen, Z. Wang, J. Sun, D. Zhao, Y. Yan, “Synthesis, morphology control, and properties of porous metal–organic coordination polymers”, Microporous Mesoporous Mater., 58 (2003) 105–114.

[115] T. J. Wu, L. J. Shen, M. Luebbers, C. H. Hu, Q.M. Chen, Z. Ni, R. I. Masel, "Enhancing the stability of metal–organic frameworks in humid air by incorporating water repellent functional groups", Chem. Commun., 46 (2010) 6120–6122.

[116] S. Hausdorf, J. Wagler, R. Mossig, F. Mertens, "Proton and Water Activity-Controlled Structure Formation in Zinc Carboxylate-Based Metal Organic Frameworks", J. Phys. Chem. A, 112 (2008) 7567–7576.

[117] S.K. Henninger, H.A. Habib, C. Janiak, "MOFs as Adsorbents for Low Temperature Heating and Cooling Applications", J. Am. Chem. Soc., 131 (2009) 2776–2777.

[118] A. Rezk, R. Al-Dadah, S. Mahmoud, A. Elsayed, "Experimental investigation of metal organic frameworks characteristics for water adsorption chillers", P. I. Mech. Eng. C-J. Mec., 227 (2013) 992–1005.

[119] C. Janiak, S.K. Henninger, "Porous Coordination Polymers as Novel Sorption Materials for Heat Transformation Processes", Chimia, 67 (2013) 419–424.

[120] F. Jeremias, V. Lozan, S. Henninger, C. Janiak, "Programming MOFs for water sorption: amino-functionalized MIL-125 and UiO-66 for heat transformation and heat storage applications", Dalton Trans., 42 (2013) 15967-15973.

[121] A. Khutia, H. U. Rammelberg, T. Schmidt, S. Henninger, C. Janiak, "Water Sorption Cycle Measurements on Functionalized MIL-101Cr for Heat Transformation Application", Chem. Mater., 25 (2013) 790-798.

[122] G. Akiyama, R. Matsuda, H. Sato, A. Hori, M. Takata, S. Kitagawa, “Effect of functional groups in MIL-101 on water sorption behavior”, Microporous Mesoporous Mater., 157 (2012) 89–93.

[123] A. O. Yazaydin, A. I. Benin, S. A. Faheem, P. Jakubczak, J. J. Low, R. R. Willis, R. Q. Snurr, “Enhanced CO_2 Adsorption in Metal-Organic Frameworks via Occupation of Open-Metal Sites by Coordinated Water Molecules”, Chem. Mater., 21 (2009) 1425–1430.

[124] J. Yang, A. Grzech, F. M. Mulderb, T. J. Dingemans, “Methyl modified MOF-5: a water stable hydrogen storage material”, Chem. Commun., 47 (2011) 5244–5246.

[125] J. G. Nguyen, S. M. Cohen, “Moisture-Resistant and Superhydrophobic Metal−Organic Frameworks Obtained via Postsynthetic Modification”, J. Am. Chem. Soc., 132 (2010) 4560–4561.

[126] J. J. Low, A. I. Benin, P. Jakubczak, J. F. Abrahamian, S. A. Faheem, R. R. Willis, “Virtual High Throughput Screening Confirmed Experimentally: Porous Coordination Polymer Hydration”, J. Am. Chem. Soc., 131 (2009) 15834 –15842.

[127] I. J. Kang, N. A. Khan, E. Haque, S. H. Jhung, “Chemical and Thermal Stability of Isotypic Metal–Organic Frameworks: Effect of Metal Ions”, Chem. Eur. J., 17 (2011) 6437 – 6442.

[128] J. H. Cavka, S. Jakobsen, U. Olsbye, N. Guillou, C. Lamberti, S. Bordiga, K. P. Lillerud, “A New Zirconium Inorganic Building Brick Forming Metal Organic Frameworks with Exceptional Stability”, J. Am. Chem. Soc., 130 (2008) 13850−13851.

[129] P. D. C. Dietzel, Y. Morita, R. Blom, H. Fjellvag, “An In Situ High-Temperature Single-Crystal Investigation of a Dehydrated Metal–Organic Framework Compound and Field-Induced Magnetization of One-Dimensional Metal–Oxygen Chains”, Angew. Chem., Int. Ed., 44 (2005) 6354−6358.

[130] D. Ma, Y. Li, Z. Li, “Tuning the moisture stability of metal–organic frameworks by incorporating hydrophobic functional groups at different positions of ligands”, Chem. Commun., 47 (2011) 7377–7379.

[131] K. A. Cychosz, A. J. Matzger, “Water Stability of Microporous Coordination Polymers and the Adsorption of Pharmaceuticals from Water”, Langmuir, 26 (2010) 17198−17202.

[132] C. Serre, “Superhydrophobicity in Highly Fluorinated Porous Metal–Organic Frameworks”, Angew. Chem., Int. Ed., 51 (2012) 6048−6050.

[133] D.-Y. Hong, Y. K. Hwang, C. Serre, G. Férey, J.-S. Chang, “Porous Chromium Terephthalate MIL-101 with Coordinatively Unsaturated Sites: Surface Functionalization, Encapsulation, Sorption and Catalysis”, Adv. Funct. Mater., 19 (2009) 1537-1552.

[134] F. Jeremias, D. Fröhlich, C. Janiak, S. K. Henninger, “Water and methanol sorption on MOFs for cycling heat transformation processes”, New J. Chem., 38 (2014) 1846-1852.

[135] Q. Liu, L. Ning, S. Zheng, M. Tao, Y. Shi, Y. He, “Adsorption of Carbon Dioxide by MIL-101(Cr): Regeneration Conditions and Influence of Flue Gas Contaminants”, Sci. Rep., 10(3) (2013) 02916.

[136] Y.-K. Seo, J. W. Yoon, J. S. Lee, U.-H. Lee, Y. K. Hwang, C.-H. Jun, P. Horcajada, C. Serre, J.-S. Chang, "Large scale fluorine-free synthesis of hierarchically porous iron(III) trimesate MIL-100(Fe) with a zeolite MTN topology", Microporous Mesoporous Mater., 157 (2012) 137-145.

[137] P. M. Schoenecker, C. G. Carson, H. Jasuja, C. J. J. Flemming, K. S. Walton, "Effect of Water Adsorption on Retention of Structure and Surface Area of Metal–Organic Frameworks", Ind. Eng. Chem. Res., 51 (2012) 6513-6519.

[138] G. E. Cmarik, M. Kim, S. M. Cohen, K. S. Walton, "Tuning the adsorption properties of UiO-66 via ligand functionalization", Langmuir, 28 (2012) 15606-15613.

[139] H. Jasuja, J. Zang, D. S. Sholl, K. S. Walton, "Rational Tuning of Water Vapor and CO_2 Adsorption in Highly Stable Zr-Based MOFs", J. Phys. Chem. C, 116 (2012) 23526-23532.

[140] N. U. Qadir, S. A.M. Said, H. M. Bahaidarah, "Structural stability of metal organic frameworks in aqueous media – Controlling factors and methods to improve hydrostability and hydrothermal cyclic stability", Microporous Mesoporous Mater., 201 (2015) 61-90.

[141] E. Katz, A. Shipweay, I. Willner "Chemically functionalized nanoparticles: Synthesis, Properties and Applications", Book Chapter, In: Nanoscale Materials, Kluwer Academic Publishers, 2003, pp 5–78.

[142] V. Georgakilas, M. Otyepka, A. B. Bourlinos, V. Chandra, N. D. Kim, K. C. Kemp, P. Hobza, R. Zboril, K. S. Kim, "Functionalization of Graphene: Covalent and Non-

Covalent Approaches, Derivatives and Applications", Chem. Rev., 112(11) **(**2012) 6156-6214.

[143] V. Agostoni, P. Horcajada, V. Rodriguez-Ruiz, H. Willaime, P. Couvreur, C. Serre, R. Gref, "'Green fluorine-free mesoporous iron(III) trimesate nanoparticles for drug delivery", Green Materials, Vol. 1, Issue GMAT4, (2013) 209–217.

[144] B. Ahmadi-Moghadam, M. Sharafimasooleh, S. Shadlou, F. Taheri, "Effect of functionalization of graphene nanoplatelets on the mechanical response of graphene/epoxy composites", Mater. Des., 66 (2015) 142–149.

[145] J. Liu, A. G. Rinzler, H. Dai, J. H. Hafner, R. K. Bradley, P. J. Boul, A. Lu, T. Iverson, K. Shelimov, C. B. Huffman, F. Rodriguez-Macias, Y-S Shon, T. R. Lee, D. T. Colbert, R. E. Smalley, "Fullerene pipes", Science, 280 (1998) 1253–1256.

[146] A. G. Márquez, A. Demessence, A. E. Platero-Prats, D. Heurtaux, P. Horcajada, C. Serre, J.-S. Chang, G. Férey, V. A. de la Peña-O'Shea, C. Boissière, D. Grosso, C. Sanchez, "Green Microwave Synthesis of MIL-100(Al, Cr, Fe) Nanoparticles for Thin-Film Elaboration", Eur. J. Inorg. Chem., 2012 (2012), 5165-5174.

[147] T. B. Čelič, N. Z. Logar, M. Rangus, V. Kaučič, "Study of the solvent effect of the synthesis of two porous iron carboxylates: MIL-100(Fe) and MIL-45(Fe)", In: Proceedings of the 4th Slovenian-Croatian Symposium on Zeolites, 17th-18th Oct., 2011, Ljubljana, Slovenia, pp 57-60.

[148] P. Horcajada, S. Surblé, C. Serre, D.-Y. Hong, Y.-K. Seo, J.-S. Chang, J.-M. Grenèche, I. Margiolaki, G. Férey, "Synthesis and catalytic properties of MIL-100(Fe), an iron(III) carboxylate with large pores", Chem. Commun., (2007) 2820-2822.

[149] J. Shi, S. Hei, H. Liu, Y. Fu, F. Zhang, Y. Zhong, W. Zhu, “Synthesis of MIL-100(Fe) at Low Temperature and Atmospheric Pressure”, Journal of Chemistry, Vol. 2013, Article ID: 792827, 4 pages.

[150] I. Ahmed, J. Jeon, N. A. Khan, S. H. Jhung, “Synthesis of a Metal−Organic Framework, Iron- Benezenetricarboxylate, from Dry Gels in the Absence of Acid and Salt”, Cryst. Growth Des., 12 (2012) 5878-5881.

[151] A. Dhakshinamoorthy, M. Alvaro, Y. K. Hwang, Y.-K. Seo, A. Corma, H. Garcia, “Intracrystalline diffusion in Metal Organic Framework during heterogeneous catalysis: Influence of particle size on the activity of MIL-100 (Fe) for oxidation reactions”, Dalton Trans., 40 (2011) 10719-10724.

[152] R. Canioni, C. Roch-Marchal, F. Sécheresse, P. Horcajada, C. Serre, M. Hardi-Dan, G. Férey, J.-M. Grenèche, F. Lefebvre, J.-S. Chang, Y.-K. Hwang, O. Lebedev, S. Turner, G. V. Tendeloo, “Stable polyoxometalate insertion within the mesoporous metal organic framework MIL-100(Fe)”**,** J. Mater. Chem., 21 (2011) 1226-1233.

[153] C. M. Granadeiro, A. D. S. Barbosa, S. Ribeiro, I. C. M. S. Santos, B. de Castro, L. Cunha-Silva, S. S. Balula, “Oxidative catalytic versatility of a trivacant polyoxotungstate incorporated into MIL-101(Cr)”, Catal. Sci. Technol., 4 (2014) 1416-1425.

[154] C. Shi, L. Chen, Z. Xu, Y. Jiao, Y. Li, C. Wang, M. Shan, Z. Wang, Q. Guo, “Monitoring influence of chemical preparation procedure on the structure of graphene nanosheets”, Physica E, 44 (2012) 1420-1424.

[155] A. Khutia, H. U. Rammelberg, T. Schmidt, S. Henninger, C. Janiak, "Water Sorption Cycle Measurements on Functionalized MIL-101Cr for Heat Transformation Application", Chem. Mater. 25 (2013) 790-798.

[156] S. K. Henninger, G. Munz, K.-F. Ratzsch, P. Schossig, "Cycle stability of sorption materials and composites for the use in heat pumps and cooling machines", Renew. Energ., 36 (2011) 3043-3049.

[157] S. Goyanes, G.R. Rubiolo, A. Salazar, A. Jimeno, M.A. Corcuera, I. Mondragon, "Carboxylation Treatment of Multiwalled Carbon Nanotubes Monitored by Infrared and Ultraviolet Spectroscopies and Scanning Probe Microscopy", Diamond Relat. Mater., 16 (2007) 412–417.

[158] W.M. Davis, C.L. Eriekson, C.T. Johnston, J.J. Delfino, J.E. Porter, "Quantitative Fourier Transform Infrared Spectroscopic Investigation of Humic Substance Functional Group Composition", Chemosphere, 38 (1999) 2913–2928.

[159] J. Shi, S. Hei, H. Liu, Y. Fu, F. Zhang, Y. Zhong, W. Zhu, "Synthesis of MIL-100(Fe) at Low Temperature and Atmospheric Pressure", Journal of Chemistry, Vol. 2013, Article ID: 792827, 4 pages.

[160] R. Liang, R. Chen, F. Jing, N. Qin, L. Wu, "Multifunctional polyoxometalates encapsulated in MIL-100(Fe): highly efficient photocatalysts for selective transformation under visible light", Dalton Trans., 44 (2015) 18227–18236.

[161] S.I. Cha, K.T. Kim, K.H. Lee, C.B. Mo, S.H. Hong, "Strengthening and toughening of carbon nanotube reinforced alumina nanocomposite fabricated by molecular level mixing process", Scripta Mater., 53 (2005) 793–797.

[162] M. G. I. Galinato, C. M. Whaley, N. Lehnert, "Vibrational Analysis of the Model Complex (μ-edt)[Fe(CO)$_3$]$_2$ and Comparison to Iron-only Hydrogenase: The Activation Scale of Hydrogenase Model Systems", Inorg Chem. 49(7) 2010 3201–3215.

[163] F. Zhang, J. Shi, Y. Jin, Y. Fu, Y. Zhong and W. Zhu, "Facile synthesis of MIL-100(Fe) under HF-free conditions and its application in the acetalization of aldehydes with diols", Chem. Eng. J., 259 (2015) 183–190.

[164] K. Y. Lee, M. Kim, J. Hahn, J. S. Suh, I. Lee, K. Kim and S. W. Han, "Assembly of metal nanoparticle-carbon nanotube composite materials at the liquid/liquid interface", Langmuir, 22 (2006) 1817–1821.

[165] T. Zhao, F. Jeremias, I. Boldog, B. Nguyen, S. K. Henninger, C. Janiak, "High-yield, fluoride-free and large-scale synthesis of MIL-101(Cr)", Dalton Trans., 44 (2015) 16791–16801.

[166] S. H. Jhung, J.–H. Lee, J. W. Yoon, C. Serre, G. Férey, J.-S. Chang, "Microwave Synthesis of Chromium Terephthalate MIL-101 and Its Benzene Sorption Ability", Adv. Mater., 19 (2007) 121–124.

[167] D. W. Brown, A. J. Floyd, M. Sainsbury, Organic Spectroscopy, Willey, New York, 1988.

[168] V. H. Pham, T. V. Cuong, S. H. Hur, E. Oh, E. J. Kim, E. W. Shin, J. S. Chung, "Chemical functionalization of graphene sheets by solvothermal reduction of a graphene oxide suspension in N-methyl-2-pyrrolidone", J. Mater. Chem., 21 (2011) 3371–3377.

[169] J. Oh, J.–H. Lee, J. C. Koo, H. R. Choi, Y. Lee, T. Kim, N. D. Luong, J.–D. Nam, "Graphene oxide porous paper from amine-functionalized poly(glycidyl methacrylate)/graphene oxide core-shell microspheres", J. Mater. Chem., 20 (2010) 9200–9204.

[170] Z. Yia**,** T. Cheng-an, J. Song, J. Wang, "Metal-organic Frameworks/Graphene Oxide Composites: Preparation and Applications in Dye Absorption", In: 4th International Conference on Sustainable Energy and Environmental Engineering (ICSEEE 2015), Shenzhen, China, Feb., 2016, pp. 642–645.

[171] J. Yan, Y. Yu, C. Ma, J. Xiao, Q. Xia, Y. Li, Z. Li, "Adsorption isotherms and kinetics of water vapor on novel adsorbents MIL-101(Cr)@GO with super-high capacity", Appl. Therm. Eng., 84 (2015) 118–125.

[172] S. Sircar, "Linear-driving-force model for non-isothermal gas adsorption kinetics", J. Chem. Soc. Faraday Trans. 1, 79(4) (1983) 785–796.

[173] J. W. Wu, S. H. Madani, M. J. Biggs, P. Phillip, C. Lei, E. J. Hu, "Characterizations of Activated Carbon−Methanol Adsorption Pair Including the Heat of Adsorptions", J. Chem. Eng. Data, 60 (2015) 1727−1731.

[174] S. Ahuja, "Water Reclamation and Sustainability", 1st Ed., Elsevier, June, 2014.

[175] C. Y. Tso, S. C. Fu, C. Y.H. Chao, "Modeling a solar-powered double bed novel composite adsorbent (silica activated carbon/$CaCl_2$)–water adsorption chiller", Build. Simul., 7 (2014) 185–196.

[176] C. E. Wilmer, M. Leaf, C. Y. Lee, O. K. Farha, B. G. Hauser, J. T. Hupp, R. Q. Snurr, "Large-scale screening of hypothetical metal–organic frameworks", Nat. Chem., 4 (2012), 83–89.

[177] A. Alshammari, Z. Jiang, K. E. Kordova, " Metal Organic Frameworks as emerging photocatalysts", Chapter 11 in Book: Semiconductor Photocatalysis – Materials, Mechanisms and Applications, Edited by W. Cao, ISBN: 978-953-51-2484-9, Intech Publisher, 2016.

[178] J.-M. Zanotti, P. Judeinstein, S. Dalla-Bernardina, G. Creff, J.-B. Brubach, P. Roy, M. Bonetti, J. Ollivier, D. Sakellariou, M.-C. Bellissent-Funel, "Competing coexisting phases in 2D water", Scientific Reports (2016). DOI: 10.1038/srep25938.

[179] https://www.alibaba.com/product-detail/99-Chromium-Nitrate-Supplier-In-China_60420752802.html

[180] https://www.alibaba.com/product-detail/99-technical-Ferric-Nitrate-in-high_60178426529.html

[181] https://www.alibaba.com/product-detail/high-quality-100-21-0 Terephthalic_60502943409.html

[182] https://www.alibaba.com/product-detail/High-Quality-Trimesic-Acid-CAS 554_1324892810.html

[183] http://www.qrg.northwestern.edu/projects/vss/docs/power/2-how-efficient-are-solar-panels.html

[184] E. Zell, S. Gasim, S. Wilcox, S. Katamoura, T. Stoffel, H. Shibli, J. Engel-Cox, M. Al- Subie, "Assessment of solar radiation resources in Saudi Arabia", Solar Energy, 119 (2015), 422–438.

NAJAM UL QADIR

P. O. Box 8569,
Dhahran, KSA
+966-596516146
najamq@kfupm.edu.sa

OBJECTIVE :

I am deeply motivated to apply my academic background in a kind of work environment where I am able to practice my knowledge base in the most efficient manner. I only believe in scientific accomplishments which are commercially reproducible and can benefit the society at large. I am highly inclined to exploit both my coursework- and research-based experiences as a means to improve my problem-solving skills, and add commercial value to the outcomes of the scientific community pertaining to my research background.

SUMMARY :

- Ten consecutive years research experience in MATLAB programming.
- Ph.D dissertation on lab-scale synthesis and characterization of two multi-walled carbon nanotube (MWCNT) incorporated water-stable Metal Organic Frameworks (MOFs), MIL-100(Fe) and MIL-101(Cr), for use in adsorption chiller applications.
- Numerical modeling of a two-bed solar adsorption chiller using MWCNT/MIL-100(Fe) composite as adsorbent and water as refrigerant.
- Hands-on operation experience of a vacuum controlled Dynamic Vapor Sorption Analyzer (DVS Vacuum, Surface Measurement Systems Inc., London, U.K.).
- Recently achieved the highest reported water vapor uptake of 1.73 gg^{-1} for a MWCNT/MIL-101(Cr) composite.
- Masters and Doctoral lab-scale experience in fabrication of composite materials incorporated with nanoscale reinforcements (KAIST, South Korea, and KFUPM, Saudi Arabia).
- Graduate course work experience of a total of 33 courses during MS and Ph.D.
- Post-MS work experience in fabrication of composite superconductors followed by current-density testing of fabricated samples at liquid nitrogen temperatures (KAERI, Daejeon, South Korea).
- Post-BS work experience in analysis of engineering materials using Scanning Electron Microscope (KRL, Kahuta, Pakistan).
- 3 years doctoral experience in industrial engineering in Florida State University, Tallahassee, FL., U.S.A.
- One and a half years doctoral experience in mechanical engineering in University of Missouri, Columbia, MO, U.S.A.

WORK EXPERIENCE:

- *Faculty of Chemical and Materials Engg*: Lecturer at National University of Science and Technology, Islamabad, Pakistan (Feb 2012 – Aug 2012)

- *Faculty of Materials Science and Engg*: Research Associate at G.I.K Institute, Swabi, Pakistan (Feb 2011 – Jan 2012)

- *Superconductivity Research Lab*: Post MS employment as Researcher, Korea Atomic Energy Research Institute, Daejeon, South Korea (Mar 2006 – July 2006)
    - Lab-scale fabrication of YBCO composite superconductors using liquid phase sintering.
    - Fabrication of samples of Y211/Y123 added with $BaCeO_3$ or $BaZrO_3$ nano-particles using melt-texturing followed by microstructural and current-density analysis of as-fabricated samples at liquid nitrogen temperatures.

- *Composite Lab*: Post BS employment as Assistant Manager, Advanced Engineering Research Organization, Hasan Abdal, Pakistan (Dec 2002 – Aug 2003)
    - Fabrication of samples for strength and toughness analysis of polymer composite parts for aerospace application.

TEACHING ASSISTANTSHIPS:

- *Mechanical Engineering:* MS program, Univ. of Missouri, Columbia (Aug., 2009 – Dec., 2010)
    - Teaching Assistant for undergraduates in Numerical Methods in Computational Design in Fall 2009 and Spring 2010.
- *Industrial Engineering:* PhD program, Florida State University, FL (Aug., 2006 – May 2009)
    - Teaching Assistant for undergraduates in Tools Engineering in Spring 2007.
    - Teaching Assistant for undergraduates in Engineering Economy in Spring 2007.
    - Teaching Assistant for undergraduates in Numerical Methods in Fall 2008.

RESEARCH ASSISTANTSHIPS:

- *Mechanical Engineering:* MS program, Univ. of Missouri, Columbia (Aug., 2009 – Dec., 2010)
    - Literature survey on modeling flexible fiber suspensions using Discrete Element Modeling.
    - Developed MATLAB simulations to model flexible fiber suspensions containing single or multiple fibers using Bead-Chain, Rod-Chain or Ellipsoid-Chain Algorithms for polymer composite manufacturing
- *Industrial Engineering:* PhD program, Florida State University, FL (Aug., 2006 – May 2009)

- Literature survey on fabrication of aligned carbon nanotube arrays on polymer-based substrates for thermal management in electronic applications.
- Literature survey on modeling fiber orientation in short fiber suspensions for polymer composite manufacturing.
- Developed a new neural network based closure for modeling fiber orientation in short fiber suspensions (Composites Part A: Applied Science and Manufacturing, Vol. 40, 1524-1533, 2009).

❖ *Materials Science:* MS program, Korea Advanced Institute of Science and Technology, Daejeon, South Korea (Mar., 2004 – Feb., 2006)

- Literature survey on alignment of carbon nanotubes using Block Copolymer Self-Assembly.
- Literature survey on fabrication of carbon nanotube reinforced nanocomposites.
- Fabricated samples of carbon nanotube reinforced alumina matrix nanocomposites using Spark Plasma Sintering followed by microstructural and mechanical analysis of fabricated samples.

COURSEWORK:

❖ *Materials Science and Engineering*: K.F.U.P.M., Dhahran, Saudi Arabia (Sep., 2012 – Present)

- Enrolled in courses pertaining to both mechanical and materials science disciplines including Materials
- Characterization Techniques, Elasticity and Plasticity, Polymer Engineering, Continuum Mechanics, Tribology and Materials Structure and Defects.

❖ *Mechanical Engineering:* MS program, Univ. of Missouri, Columbia (Aug., 2009 – Dec., 2010)

- Attended coursework pertaining to all fields of structural engineering including Finite Element Methods, Advanced Computational Design, and Heat and Mass Transfer.
- Enrolled in applied mathematics classes including Numerical Methods, Numerical Linear Algebra and Applied Analysis.
- Worked as a teaching assistant in Computational Methods in Engineering Design in Fall 2009 and Spring 2010.

❖ *Industrial Engineering:* PhD program, Florida State University, FL (Aug., 2006 – May 2009)

- Studied courses related to various industrial engineering applications including Engineering Data Analysis, Design of Engineering Experiments and Modeling and Analysis.
- Enrolled in applied mathematics classes including Numerical Methods in Engineering and Applied Optimization.

- Attended coursework pertaining to mechanical engineering and computational materials science including Heat Transfer, Continuum Mechanics and Multiscale Modeling of Materials.

❖ *Materials Science:* MS program, Korea Advanced Institute of Science and Technology, Daejeon, South Korea (Mar., 2004 – Feb., 2006)

- Attended coursework pertaining to materials science basics including materials thermodynamics, structure and defects in solids, optical materials and dislocation theory.
- Enrolled in coursework related to materials engineering including and sintering process and theory, semi-conductor physics and sintering process fundamentals.

ACHIEVEMENTS:

❖ Selected five times in Dean's Honor Roll during BS.
❖ Scored 720 in Verbal and 6.0 in Analytical Writing Section in GRE General Test (Sep., 2003).
❖ Scored 287 in TOEFL Computer Based Test (June, 2004).
❖ Overall GPA of 3.8/4.0 in Ph.D study at K.F.U.P.M, Dhahran, Saudi Arabia.
❖ Overall GPA of 3.8/4.0 in graduate studies in U.S.A.
❖ Consecutive 10 years of research experience in MATLAB programming.
❖ A total of 33 graduate-level courses during MS and PhD programs.

LANGUAGE SKILLS:

❖ Fluent in Spoken and written English.
❖ Urdu as native language.

CO-CURRICULAR ACTIVITIES:

❖ Hockey.
❖ Music.
❖ Thinking about my useless past.

POSTER PRESENTATIONS:

❖ Najam ul Qadir, David A. Jack and Ben Wang, "Modeling Fiber Orientation in Rigid and Flexible Fiber Suspensions", Florida State University, March 2008.
❖ Najam ul Qadir and David A. Jack, "Modeling Fiber Orientation in Rigid and Flexible Fiber Suspensions for Polymer Macro- and Nano-composite Manufacturing", Florida State University, March 2009.

JOURNAL PUBLICATIONS:

- C. J. Kim, Najam ul Qadir, Asif Mahmood, Y. –H Han and T.-H Sung, "The Effect Of $BaCeO_3$ Nano-particles on the Current Density of a Melt-Processed YBCO Superconductor", Physica C: Superconductivity, Vol. 463-465, 344-347, 2007.
- Najam ul Qadir and David A. Jack, "Modeling Fiber Orientation in Short Fiber Suspensions Using the Neural Network Based Orthotropic Closure", Composites Part A: Applied Science and Manufacturing, Vol. 40, 1524-1533, 2009.
- Nouari Saheb, Najam Ul Qadir, Muhammad Usama Siddiqui, Abul Fazl Muhammad Arif, Syed Sohail Akhtar and Nasser Al-Aqeeli, "Characterization of Nanoreinforcement Dispersion in Inorganic Nanocomposites: A Review", Materials, Vol. 7, No. 6, 4148-4181, 2014.
- Najam ul Qadir and S.A.M. Said, "Structural stability of metal organic frameworks in aqueous media – Controlling factors and methods to improve hydrostability and hydrothermal cyclic stability", Microporous and Mesoporous Materials, Vol. 201, 61-90, 2015.
- Najam U. Qadir and Stephen M. Smith, "Use of Exact Gradient and Hessian in LM Algorithm – A Comparison of Jacobian-Based and Hessian-Based Learning", under review in international journal of artificial intelligence and soft computing.
- Najam ul Qadir, S.A.M. Said, Rached B. Mansour, "Modeling the Performance of a Two-bed Solar Adsorption Chiller using a Multi-walled Carbon Nanotube/MIL-100(Fe) Composite Adsorbent", under review in Renewable Energy.
- Najam U. Qadir, Syed A. M. Said, Rached B. Mansour, Khalid Mezghani, and Anwar U. Hamid, "Synthesis, Characterization, and Water Adsorption Properties of a Novel Multi-Walled Carbon Nanotube/ MIL-100(Fe) Composite", Dalton Transactions, Vol. 45,15621-15633, 2016.
- S. A. M. Said, N. U. Qadir, R. B. Mansour, Khaled Mezghani and H. M. Irshad, "Synthesis, Characterization and Water Sorption Kinetics of a Graphene oxide/MIL-100(Fe) Composite as a Potential Adsorbent for Chiller Applications", Manuscript under preparation.

ACADEMIC INTERNSHIPS:

- *Production and Processing of Alloy Steels*: Peoples' Steel Mills, Karachi, Pakistan (May 2001)
    - Observed production of various types of alloy steels for household and industrial use.
    - Experienced different classes of steel processing operations including rolling, forging, sheet metal forming, roll-forging and rotary forging.

EDUCATION:

- **King Fahd University of Petroleum and Minerals, Dhahran, Saudi Arabia**
  - Ph.D in Materials Science and Engineering
  - Dissertation title: Carbon nanotube and graphene incorporated water-stable MOFs as potential adsorbents in solar-powered high-performance adsorption chillers.
- **University of Missouri, Columbia, MO**
  - MS in Mechanical and Aerospace Engineering (Aug. 2009 – Dec. 2010) (credits transferred from Florida State University, FL)
- **Florida State University, Tallahassee, FL**
  - Enrolled in PhD program in Industrial Engineering (Aug. 2009 – Dec. 2010)
- **Korea Advanced Institute of Science and Technology, Daejeon, South Korea**
  - MS in Materials Science and Engineering (Mar. 2004 – Feb. 2006)
- **G.I.K Institute of Engineering Sciences and Technology, Swabi, NWFP, Pakistan**
  - BS in Metallurgy and Materials Engineering (Aug. 1998 – May 2002)